

THE UNIVERSITY OF CALGARY

FAR INFRARED AIRBORNE OBSERVATION OF THE EXTREME SOLAR LIMB
DURING THE TOTAL ECLIPSE OF FEBRUARY 26 1979

BY

RITA THERESE BOREIKO

A THESIS

SUBMITTED TO THE FACULTY OF GRADUATE STUDIES
IN PARTIAL FULFILLMENT OF THE REQUIREMENTS FOR THE DEGREE OF
MASTER OF SCIENCE

DEPARTMENT OF PHYSICS

CALGARY, ALBERTA

SEPTEMBER, 1979

© Rita T. Boreiko 1979

THE UNIVERSITY OF CALGARY

FACULTY OF GRADUATE STUDIES

The undersigned certify that they have read, and recommend to the Faculty of Graduate Studies for acceptance, a thesis entitled, "Far Infrared Airborne Observation of the Extreme Solar Limb During the Total Eclipse of February 26 1979" submitted by Rita T. Boreiko in partial fulfillment of the requirements for the degree of Master of Science.



Supervisor Physics
T.A. Clark



C.D. Anger Physics

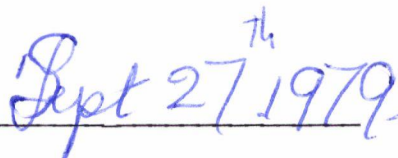


E.F. Milone Physics



F.C. Adam Chemistry

Date



ABSTRACT

Knowledge of the thermal and physical structure of the low chromosphere near the temperature minimum in the sun is important for the development of solar models, and in particular for the evaluation of the mechanisms of energy transfer operating in this region. Source heights for far infrared wavelengths lie within this height range, and are relatively easily determined theoretically, and therefore solar observations with high spatial resolution within this spectral region can be expected to be very valuable. Unfortunately, such measurements are also difficult to obtain, since this radiation is almost totally absorbed in the earth's lower atmosphere. In addition, the resolution attainable is severely limited by diffraction, even for the largest available telescopes.

These limitations were simultaneously overcome in the experiment described in this thesis, in which the far infrared intensity distribution near the solar limb was obtained to high resolution (in one dimension) from measurements taken from above the bulk of the atmosphere in a jet aircraft during a total solar eclipse. The design and performance of a four-channel far infrared photometer and its associated electronics and optics are described, along with many of the operational considerations which are specific to this type of experiment. The results from a period of eight minutes including second contact and part of eclipse totality from one channel of the photometer are presented, and are compared with eclipse curves generated for several model intensity distributions across the sun.

It is concluded that the radiation distribution is essentially uniform, with the possibility of very slight limb brightening, but of an amount significantly less than that predicted by a model based on the thermal structure of the region of origin of the radiation. In addition, there is no evidence for the intense "spike" of radiation which was measured at the extreme limb of the sun in the only previous experiment equivalent to that discussed here, and which was interpreted as resulting from the integrated emission of spicules overlapping in the line of sight at the limb. Therefore the lower extent of spicular structure, and its observability in this wavelength range, remains uncertain. The present results emphasize the non-equivalence of the two types of measurement, that of disc centre brightness temperature determination and of limb scanning, which until recently had been thought to be comparable methods of inferring thermal structure of the solar atmosphere. These results support the conclusion that limb scans are dominated by inhomogeneity in the lower chromosphere, although detailed knowledge of the structure and behaviour of this inhomogeneity is as yet unknown.

ACKNOWLEDGEMENTS

I would like to express my deep gratitude to my supervisor, Dr. T.A. Clark, for the support and guidance generously and unfailingly extended throughout this project. Without his hard work and dedication the experiment would not have been possible, and the incorporation of his ideas into all phases of the work contributed greatly to its success. It has been a privilege to work with someone with such interest, knowledge, and enthusiasm for all aspects of any project in which he is involved.

I would also like to thank David Naylor and David Kendall, the other members of the group, for many valuable discussions, and for making membership in the group a rewarding experience. I am especially grateful to David Naylor for teaching me many aspects of experimentation and data analysis during the course of a previous project.

Additionally, I would like to thank John Ewing for assistance with electronics and mechanical work; Ted Mani of the Physics Machine Shop for construction of much of the instrument; the staff of NASA - Ames Research Center, especially Mr. Robert Mason, for use of the Lear Jet and associated equipment, and for management of some of the operational aspects of the experiment; Grumman Aircraft Corporation for the loan of the heliostat slide mount; Northrop Services for assistance with incorporation of the equipment into the aircraft; SED Systems for programming the encoder and time code generator; Glen Stinnett and Garry Hill for their competent flying during the eclipse; Laura Boreiko for her careful drawing of the figures in this thesis; NSERC and the University of Calgary for financial support during the course of this project; and NRC and SRFB for funding the experiment.

To those who see
infinite beauty and mystery in the universe,
and whose lives on our fragile planet
are a gift to the future

TABLE OF CONTENTS

	<u>Page</u>
ABSTRACT	iii
ACKNOWLEDGEMENTS	v
DEDICATION	vi
TABLE OF CONTENTS.	vii
LIST OF TABLES	ix
LIST OF FIGURES.	x
CHAPTER 1 BASIC CONCEPTS.	1
1.1 Introduction.	1
1.2 Structure of the Quiet Sun.	2
1.3 The Quiet Chromosphere.	5
1.4 Radiative Transfer.	7
1.5 Complications	13
1.6 Outline of the Work	14
CHAPTER 2 DISCUSSION OF PREVIOUS WORK	16
2.1 Introduction.	16
2.2 Model Atmospheres	16
2.3 Summary of Previous Results	22
2.3.1 Ultraviolet Results	23
2.3.2 Visible and Near Infrared Results	25
2.3.3 Far Infrared and Submillimetre Results.	27
2.3.4 Millimetre Results.	30
2.3.5 Summary of Observations	33
CHAPTER 3 EXPERIMENTAL DESIGN	35
3.1 Introduction.	35
3.2 Infrared Photometer Optics and Alignment Tests.	37
3.3 Energy Considerations and Filter Requirements	41
3.4 Helio-stat System and Auxiliary Optics	46
3.5 Electronics and Data Recording.	48

	<u>Page</u>
3.6 Optimization of Flight Path	52
3.7 Configuration of Equipment in the Aircraft. . . .	55
3.8 Test Flight Performance	62
CHAPTER 4 ECLIPSE TIMING AND GENERATION OF THEORETICAL ECLIPSE CURVES.	65
4.1 Introduction.	65
4.2 Eclipse Geometry.	65
4.3 Determination of Actual Flight Path	67
4.4 Contact Timing.	68
4.5 Angular Eclipse Speed	71
4.6 Contact Position Angle Determination and Location of Active Regions.	72
4.7 Theoretical Eclipse Curves from Models.	79
CHAPTER 5 INSTRUMENT PERFORMANCE, DATA ANALYSIS, AND CONCLUSIONS	86
5.1 Introduction.	86
5.2 Eclipse Flight Performance.	86
5.3 Data Reduction and Initial Analysis	88
5.4 Visible Monitor Eclipse Curve	90
5.5 Far Infrared Data	92
5.6 Uncertainties in the Data	104
5.7 Improvements and Future Work.	106
REFERENCES	108

LIST OF TABLES

<u>Table</u>	<u>Page</u>
3.1 Filters in the radiation beams	43
3.2 Infrared system characteristics.	45

LIST OF FIGURES

<u>Figure</u>	<u>Page</u>
1.1 Schematic diagram of solar structure, greatly simplified	3
1.2. Continuous absorption coefficient, showing major sources of opacity	12
2.1 Temperature distribution of the photosphere and low chromosphere as given by several models.	21
3.1 Optical system of one dual-channel photometer.	39
3.2 Energy per unit wavenumber from a 5260 K equivalent blackbody reaching the detector in the four channels. Effective wavenumber and full-width half maximum are indicated.	44
3.3 Auxiliary visible system	47
3.4 Infrared signal electronics, one channel	50
3.5 Data recording system.	51
3.6 Aircraft flight paths for test and eclipse flights . .	56
3.7 Layout of equipment in Lear Jet cabin.	57
3.8 View through the door of the Lear Jet, showing electronics rack and heliostat	58
3.9 Photograph of the equipment in the baggage compartment of the Lear Jet, in flight configuration	60
3.10 The Lear Jet at the refuelling stop in Minot, on the eclipse day.	64
4.1 Aircraft flight path during eclipse run.	70
4.2 Apparent motion of lunar limb relative to solar active features as seen from the aircraft	75

<u>Figure</u>		<u>Page</u>
4.3	The eclipsed sun as seen from Oxbow, showing location of active features visible after second contact.	76
4.4	Solar active regions, seen on the sun on Feb. 26 1979, showing sunspots, calcium plage regions, and H α features	77
4.5	Arc length of an exposed annulus, for various cases. .	82
4.6	Radial distribution of solar intensity for several models	84
4.7	Predicted eclipse curves for three solar intensity distributions of Fig. 4.6.	85
5.1	Eclipse curve for auxiliary optical sensor	91
5.2	One second data averages and model predictions	93
5.3	Five second data averages and model predictions. . . .	94
5.4	Ten second data averages and model predictions	95

CHAPTER 1

BASIC CONCEPTS

1.1 Introduction

The unique position of the sun as the nearest star and the only one whose disc is resolvable without the use of interferometric techniques has proved to be a great advantage for its observation. The consequences of its proximity are numerous and, for the most part, obvious: large flux, the possibility for high spectral and spatial resolution without long integration times, and the opportunity for observations which do not depend upon electromagnetic radiation, to list only a few. However, the variety and quantity of available measurements have led to the identification of features on the sun which are complex and difficult to interpret, and there are still many aspects of the quiet sun such as spatial structure and temporal variations as well as manifestations of activity which are not yet satisfactorily explained. One of the consequences of the sun's accessibility to observation thus has been the dispelling of the illusion that it is a relatively easily explained entity, and the persistence of this illusion in the case of other more remote stars can probably be attributed solely to the limited observational data available. Although solar physics has progressed considerably since the time when the sun was thought to be a perfect, homogeneous, and static body, there is still a great deal to be learned, and the sun remains very much a mystery and a challenge.

1.2 Structure of the Quiet Sun

The sun has been divided into several distinct regions, which are shown schematically in Fig. 1.1. Nuclear energy generation occurs in the core at temperatures of the order of 1.5×10^7 K, and gradually photons that are produced in these fusion reactions diffuse outward, losing energy by various processes as they do so. Temperature, density, and pressure decrease rapidly and relatively smoothly outward from the core through the interior until, at a radius approximately 0.86 that of the sun (defined by the apparent location of the limb of the sun in visible light), the temperature has decreased to the point where significant recombination of electrons with nuclei can take place. The presence of these atoms and ions, particularly the H^- ion, increases the opacity, thereby reducing energy outflow by radiative transfer. A further consequence of this is a modification of the temperature gradient which then becomes greater than the adiabatic temperature gradient in the gas, resulting in convective instability. Energy transport in this region thus becomes predominantly convective rather than radiative. Above the convective zone, the temperature and density continue to decrease through the photosphere, and opacity to photons of visible wavelengths drops below unity; consequently, these photons have a good probability of escaping from the solar atmosphere. The sharp-edged appearance of the visible photosphere is the result of a rapid decrease in density of the H^- ions (which are primarily responsible for the visible emission), arising from a combination of the natural scale height behaviour of the atmosphere and the faster decrease of electron density

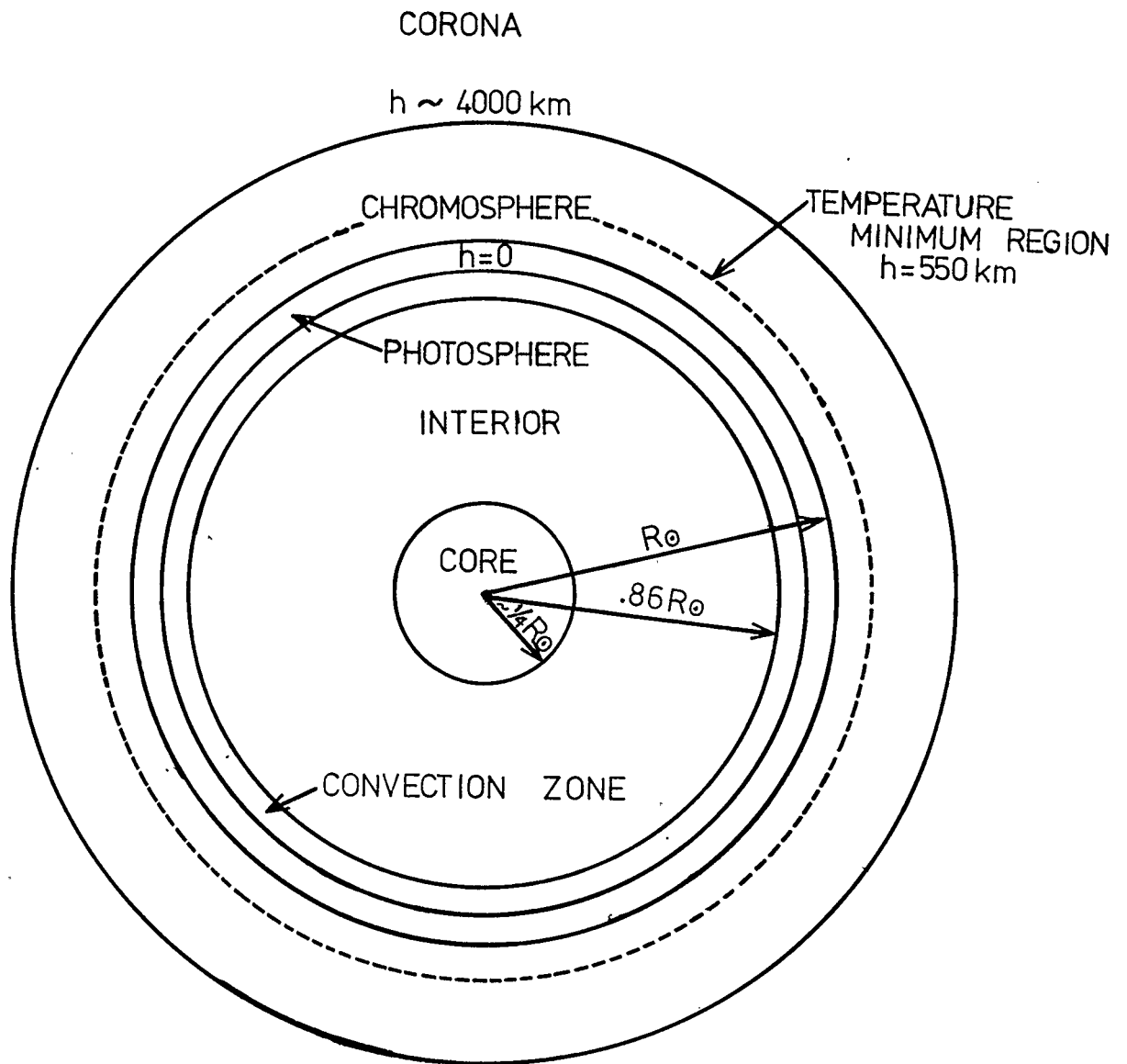


Fig. 1.1 Schematic diagram of solar structure, greatly simplified.

caused by the fall-off in temperature. The temperature reaches a minimum approximately 550 km above the photosphere, and then, surprisingly, increases rapidly in the chromosphere. The turbulent motion of the gas in the convection zone appears to generate acoustic and gravity waves which propagate through the photosphere and degenerate into shock waves as they reach the much lower density of the chromosphere. This leads to a significant deposition of energy which is thought to account, at least in part, for the abrupt temperature increase above the temperature minimum. Above the chromosphere lies the corona, which consists of very high temperature ($\sim 1 \times 10^6$ K), low density material and merges at its outer regions with the solar wind which is continuously expanding into space.

Even the "quiet" sun cannot be thought of as quiescent, since many features which are always present are also dynamic and rapidly changing in structure. The photosphere at high resolution shows the effects of the turbulence from the underlying convective zone, in the form of granulation. Cells of gas rise through the convection zone, radiate their heat at the photosphere and then sink downward with time scales of the order of ten minutes. Larger patterns of photospheric motion are detected primarily as horizontal motions in the supergranular cells, which carry with them magnetic fields, producing the chromospheric network of magnetic field enhancement. It is preferentially along this network that another manifestation of the dynamic nature of the solar atmosphere, the spicules, occurs. These spicules are columns of higher density material projecting through the chromosphere, with temperatures significantly greater than those existing at their base,

and with lifetimes of several to tens of minutes. The solar atmosphere also is subject to oscillations of various periods, particularly near 300 seconds (Stein and Leibacher, 1974), which were detected initially as periodic Doppler shifts in spectral lines probably indicating fluctuations of the solar surface, but which also have been seen in physical characteristics such as brightness and, recently, in the limb darkening function (Hill and Caudell, 1979).

The real sun is never quiet, nor can it be considered in general to be in thermodynamic or hydrostatic equilibrium. Magnetic fields play an important role in active regions as well as in determining some of the properties of the quiet sun. Active features such as sunspots, plage regions, prominences, and flares grow and die unpredictably, but are fundamentally related to physical processes occurring in the solar atmosphere. A complete theoretical description of the sun is not yet possible, but progress is being made in the understanding of limited aspects of its behaviour.

1.3 The Quiet Chromosphere

The experiment described in this thesis is an attempt to obtain information at high spatial resolution on the structure of the chromosphere by observation of radiation in the far infrared spectral region for which the source height in a homogeneous atmosphere is predicted to lie in the chromosphere. The chromosphere, although acting as a transition region between photosphere and corona, can be considered an entity in its own right. The lower limit of the chromosphere is defined approximately by the height at which the opacity for visible wavelengths

has decreased to the point where the probability for escape of visible photons is high (i.e., the optical depth of the atmosphere is ~ 0.1), while the upper limit extends beyond 15,000 km and merges into a transition zone to the corona. Both these boundaries are relatively poorly determined, and to some extent arbitrary.

The chromosphere has been subdivided into three zones (Durrant, 1978) according to different physical characteristics. In the low chromosphere, fluctuations of temperature and density are sufficiently small that a homogeneous model can be applied as a reasonable first-order description. This region comprises a very narrow layer lying just above the photosphere. The middle chromosphere is the most difficult region to describe, since the magnetic field begins to dominate gas motions, and energy transport has significant contributions from three modes: radiative, mechanical, and conductive. This region has features of both the low and high chromosphere, and the interaction of the two is extremely difficult to describe theoretically. The high chromosphere consists almost exclusively of dynamic features such as spicules and bright mottles, interspersed with high temperature, low density coronal material, and merges into the transition zone between the chromosphere and corona at heights of the order of 20,000 km.

Primarily the low and middle chromosphere is of interest for the present experiment. This region can be thought of as a synthesis of two components; spicules, and interspicular material, which have completely different physical characteristics. It is neither homogeneous nor in hydrostatic equilibrium, and therefore its description becomes complex. The spicule component of the chromosphere remains

essentially at a constant temperature of $\sim 16,000$ K above 3000 km, which is the lowest height at which spicules have been observed reliably, while electron density decreases by a factor of ten between 3000 and 11,000 km (see the review paper of Beckers, 1968 for a detailed discussion of spicules). The electron temperature of the interspicular component increases from approximately 5500 K to 18,000 K over the same height range, and electron density decreases much more quickly, by a factor of ten in 3000 km. The spicules, of width approximately 850 km, are thought to cover a fraction of the solar surface which decreases from 2.2% at 3000 km to a tenth of this at 10,000 km. The preceding are only very broad characteristics, and are still uncertain.

Of particular interest to the present experiment is the nature of the chromosphere above the temperature minimum region to heights of 3000 km. It is not known whether spicules extend down below the height at which they can be readily identified in the atmosphere, whether they merge into an average chromosphere below this height, or whether they are shielded from observation by the presence of other material. The form of the chromosphere at this level, especially the deviations from a spherically symmetric temperature and electron density structure allowed by the absence of hydrostatic equilibrium, is not known reliably. The main aim of this experiment is to obtain data which would help to clarify some of the uncertainties in the present knowledge of the structure of the lower chromosphere, outlined above.

1.4 Radiative Transfer

Knowledge of the thermal structure of the temperature minimum and low to middle chromosphere is important for the evaluation of the role of

various energy transfer mechanisms for heating these layers, and as a discriminator between various models of the solar atmosphere. This information can be obtained in several wavelength regions, discussed in 2.3, and by several techniques. Measurement of the disc centre temperature over a range of wavelengths is equivalent to measuring the distribution of intensity across the visible solar disc at a single wavelength, provided the atmosphere conforms to certain restrictions. The interpretation of both of these types of measurement in terms of a temperature profile in the solar atmosphere requires a relation between wavelength or angle from the solar limb and height. Such a relationship is provided, in the ideal case, by the theory of radiative transfer.

The nature of the radiation emerging from the solar atmosphere depends upon the interactions between it and the solar gas on its way from the centre of the sun. The source of solar energy is believed to be nuclear fusion, via the proton-proton cycle, in the core. Part of this energy is released in the form of gamma rays which diffuse slowly outward, and the spectrum of this radiation is progressively softened by interactions such as pair production, Compton scattering, and bremsstrahlung. The characteristics of the emergent radiation do not reflect conditions in the original point of formation in the core, but rather those in a relatively narrow region high in the atmosphere, where the last interaction is likely to have occurred.

If a beam of radiation of specific intensity I_λ (energy per unit area, solid angle, wavelength interval, and time) travels through an atmosphere, interactions will modify the intensity by absorption, emission, and scattering. Absorption and scattering as removal mechanisms

are described by

$$\frac{dI_{\lambda}}{ds} = -\rho\kappa_{\lambda}I_{\lambda} \quad ,$$

where ρ is gas density, κ_{λ} is mass absorption coefficient or opacity, and ds is path length; while emission and scattering as sources of photons are similarly represented:

$$\frac{dI_{\lambda}}{ds} = \rho j_{\lambda} \quad ,$$

where j_{λ} is the emission coefficient. Net change of intensity in the beam is then given by:

$$\frac{dI_{\lambda}}{ds} = (j_{\lambda} - \kappa_{\lambda}I_{\lambda})\rho = (S_{\lambda} - I_{\lambda})\rho\kappa_{\lambda} \quad ,$$

with $S = j_{\lambda}/\kappa_{\lambda}$ called the source function. For the idealized case of full thermodynamic equilibrium, I_{λ} is given by the Planck function,

$$B_{\lambda}(T) = \frac{2hc^2}{\lambda^5} [\exp(hc/\lambda kT) - 1]^{-1} \quad ,$$

as is the source function since a gradient cannot exist in thermodynamic equilibrium. However, the solar atmosphere is not in full thermodynamic equilibrium since there exists a source of radiation in the core, and loss in the outer atmosphere; hence, there must be a gradient. A more restricted concept, that of local thermodynamic equilibrium (LTE), in which the radiation field at a given point is described by the Planck function at the local temperature and which is characteristic of the gas and radiation over a small region, is approximately valid in some regions of the solar atmosphere. One further modification, which is sometimes also referred to as LTE, consists of characterizing the gas by one temperature and the radiation by another, perhaps that at a slightly

greater depth.

The degree of transparency of the solar atmosphere can be characterized by the optical depth, τ_λ , which is defined differentially by

$$d\tau_\lambda = -\rho\kappa_\lambda dr = -\rho\kappa_\lambda \cos(\theta) ds$$

where θ is the angle from the normal to the atmosphere to the line of sight. Using this relationship, the equation of transfer can be rewritten as

$$\cos(\theta) \frac{dI_\lambda}{d\tau}(\tau_\lambda, \theta) = I_\lambda(\tau_\lambda, \theta) - S_\lambda(\tau_\lambda)$$

assuming an isotropic source function, which in practice implies that the contribution of scattering must be small. This can be integrated to give

$$I_\lambda(\tau_\lambda, \theta) \exp(-\tau_\lambda/\cos(\theta)) = -\int_\infty^{\tau_\lambda/\mu} S_\lambda \exp(-\tau_\lambda/\mu) d(\tau_\lambda/\mu)$$

where $\mu = \cos(\theta)$, and the intensity emerging from the atmosphere, $I_\lambda(0, \theta)$, is given by

$$I_\lambda(0, \theta) = \int_0^\infty S_\lambda \exp(-\tau_\lambda/\mu) d(\tau_\lambda/\mu) \quad .$$

The usefulness of limb scanning can be seen from this latter relationship. If the source function is highly dependent upon optical depth, as is the case in the sun, the emergent radiation will reflect strongly the conditions at τ_λ/μ approximately equal to unity. Looking at different angles to the normal to the atmosphere (i.e., disc centre) is then equivalent to looking to differing depths within the solar atmosphere.

For full use to be made of the potential of limb scanning as a technique for investigating the thermal structure of the atmosphere, the

relationship between physical heights of origin of radiation in different spectral regions should be established. This means determining the sources of opacity in various wavelength regions, and their relative contributions. The function describing the variation of absorption coefficient with wavelength is a very complex one, particularly in the ultraviolet region where line opacities become dominant. A simplified diagram of the wavelength dependence of opacity in the solar atmosphere is shown in Fig. 1.2 (from Unsöld,1977). The relative contributions from various sources as used in a particular model of the solar atmosphere is given in Fig. 23 of the paper describing the VAL model (Vernazza et al,1976), and gives some idea of the complexity of the problem of determining sources of opacity.

There exists a pronounced minimum in the continuous opacity near $1.6 \mu\text{m}$, and consequently this wavelength at disc centre defines the deepest directly observable level of the solar atmosphere. At longer wavelengths, through the infrared and up to the radio region, the opacity, due to H^- free-free transitions (see Mankin and Strong,1969 for a discussion of other possible sources of opacity in this region), increases in a simple manner and depends upon the square of the wavelength (see John,1964,1966 for coefficients). Therefore in this spectral region it is in principle a particularly simple matter to relate source heights of various points along a limb scan with those of disc centre, and thus to compare limb scan data with central temperature values at different wavelengths, provided the source region is homogeneous.

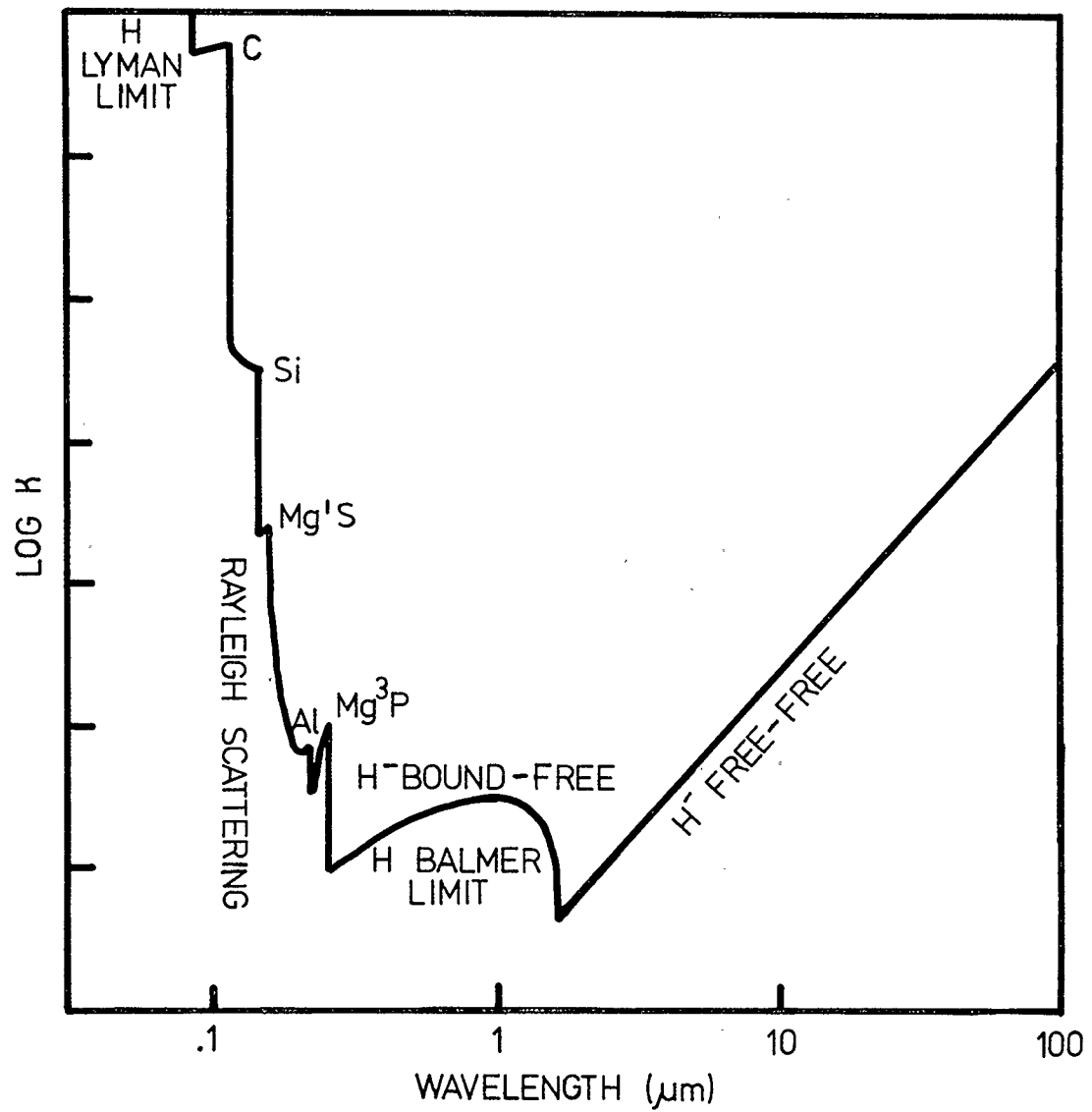


Fig.1.2 Continuous absorption coefficient, showing major sources of opacity.

1.5 Complications

The foregoing discussion has been based on simplifying assumptions, especially the existence of thermodynamic or local thermodynamic equilibrium, and spherical symmetry. The former may be a reasonable assumption for the low chromosphere but it certainly is not true for the components of the middle chromosphere, and the absence of hydrostatic equilibrium throughout the region makes the latter assumption appear unreasonable. Perhaps a more realistic picture of the chromosphere is that of a dynamic region where surfaces of equal temperature or density are not at a constant radius, but rather are randomly displaced over scale sizes of thousands of kilometres. These surfaces are interspersed with higher temperature and density spicular structures which are oriented at various inclinations to the normal to the surface and have lifetimes of several minutes. Whereas disc centre temperature measurements should be affected only marginally by the inhomogeneities implicit in the above description, this is certainly not true of limb scans. At any angle of observation between line of sight and the normal to the surface, the radiation seen will have contributions from many displaced regions of this fictitious homogeneous atmosphere, unless the angular resolution is better than $1''$ in two dimensions, which at present cannot be achieved even approximately at far infrared wavelengths. As the viewing angle is changed, the path length through any layer of constant temperature varies according to the nature of the surface structure, and cannot in general be predicted from simple considerations of spherical symmetry. Statistical ray tracing calculations

must be performed to evaluate the resultant effect on limb scans, and previous work of this kind (Beckman, Clark, and Ross, 1973) has shown that the equivalence between disc centre temperature measurements and limb scans no longer exists in such a model.

The effects of spicules must be similarly evaluated. Purely geometric considerations indicate that their contribution should increase as the limb is approached, since, as their angle to line of sight increases, a larger fraction of the surface appears to be covered by spicular material, until effects of overlapping must also be taken into account. The conclusion to be drawn from the above discussion is that data from limb scanning will be of greater value for investigating the physical structure of the dynamic chromosphere, and the nature of the inhomogeneities which form an integral part of this region of the sun, than for the straightforward determination of the thermal structure of the atmosphere.

1.6 Outline of the Work

This thesis describes the design, execution, and analysis of results from an aircraft-borne experiment whose aim was to obtain the distribution of far infrared radiation across the solar disc to high angular resolution from a measurement of intensity changes during the total solar eclipse of Feb. 26 1979. Chapter 2 gives a brief description of some of the models of the solar atmosphere which have been constructed on the basis of observational data, and presents a summary of limb scan observations in other spectral regions, with a discussion of unexpected features in the data. Chapter 3 describes the design of the experiment

and the incorporation of the equipment into the aircraft, and discusses the planning of the eclipse flight path and instrument performance during test flights. Chapter 4 provides some of the background of spherical geometry necessary for the interpretation of the eclipse data, and explains how some of the essential parameters were obtained for the actual flight. Chapter 5 presents the data obtained from the eclipse and the conclusions drawn from the data. The thesis concludes with a summary of the uncertainties remaining in the data and a discussion of improvements which could be added to similar observations in the future to extend significantly the usefulness of the present technique.

CHAPTER 2

DISCUSSION OF PREVIOUS WORK

2.1 Introduction

Solar limb scan information has been obtained at many wavelengths over the past few decades, and attempts have been made to interpret this information and to incorporate the general trends into various models. It is instructive to outline the successive models developed to represent the solar atmosphere and to examine briefly the measurements from other spectral ranges, especially those which are expected to have particular relevance to far infrared results.

2.2 Model Atmospheres

The interpretation of limb scans as well as disc centre intensity measurements in terms of the physical structure of the sun necessitates the use of models of the solar atmosphere. To facilitate the comparison of results of different workers and at differing wavelengths, it is useful to have a standard model which, if necessary, is modified periodically to bring it into better agreement with existing data. Ideally, the model should be constructed theoretically, on the basis of a given composition, by using calculated opacities and by determining temperature, pressure, and density profiles from consideration of mechanisms of energy transfer and hydrodynamic conditions. In practice, this is not yet possible to achieve because of the difficulty of representing processes such as mechanical energy deposition into the chromosphere, the mechanism for which is still a matter for debate (see for example Ando and Osaki, 1977; Athay and White, 1978; Bruner, 1978; Durrant,

1978; and Ulmschneider and Kalkofen, 1978), and radiative transfer between spectral lines and the continuum. Also, theoretical description of time-dependent processes such as solar activity, and of spatial inhomogeneity has not yet progressed to the point of being reliably incorporated into a solar model. Thus, for example, the theoretical model of Kurucz (1974) is a fairly good representation of a static, spherically symmetric photosphere in LTE, but fails to predict the increase of temperature in the chromosphere. Because of these limitations to the theoretical approach, the majority of model atmospheres have been constructed either empirically, by adjusting a temperature and pressure profile to obtain the best agreement with observations such as intensity and flux measurements and limb scans at various wavelengths, or semiempirically, in which the empirical approach is restricted by physical assumptions such as modes of energy transport or the requirement for consistency with the existence of the hydrogen convection zone below the photosphere (Frisch, 1972; Elste, 1968).

Many models of the empirical or semiempirical type, or modifications of existing models, have been proposed, some based on a single set of observational results or attempting to explain a single feature (e.g., Neidig, 1973). Only a few of the models referred to most often will be discussed further. One of the earliest attempts to produce a model of the photosphere and low chromosphere to serve as a reference for observational work was that of Heintze et al (1964), and resulted in the Utrecht Reference Photosphere (URP). This model consists of three columns; hot, upward rising gas; cool, downward moving gas; and an average, stationary column, but the relative importance of these three is not determined by the model. In origin, the URP was already

a synthesis and a modification of previous, more limited models. It was based upon the very limited observational data existing at the time, which consisted predominantly of visible and near infrared measurements, with a few in the ultraviolet. It was anticipated that the model would be modified as subsequent observations became available, and it was recognized that such a simplified model could never be an adequate representation of the solar atmosphere. The temperature in the URP reaches a minimum value of 4500 K near $\tau_{5000}=0.02$, where τ_{5000} is the optical depth at a wavelength of 500 nm (which corresponds to a height of approximately 200 km above the photosphere).

The URP was superseded in 1967 by the Bilderberg Continuum Atmosphere (BCA), which was the result of an international study week designed to synthesize as much of existing data as possible into an internationally acceptable model of the photosphere and low chromosphere (Gingerich and de Jager, 1968). The photospheric temperature distribution was determined from visible and near infrared intensities and limb darkening curves (and was subsequently modified by Elste (1968) to give better agreement with the limb darkening data), and was extended to deeper levels by using the mixing length theory of convection. The adopted value of 4600 K for the temperature minimum region, as well as the physical extent of this region, were based on ultraviolet and some infrared measurements, with the strength of carbon monoxide lines used as corroborative evidence. The temperature structure of higher layers depended on intensity measurements in the millimetre and far ultraviolet spectral regions, which agreed surprisingly well. Again, the model is simplified, assuming hydrostatic equilibrium and homogeneity, and line observations are essentially not included because of difficulties with

their interpretation. For example, neither of the two alternatives proposed at the time for the interpretation of the H and K lines of Ca II and Mg II are in agreement with the BCA model. Conversely, some models have been based largely on spectral line data (e.g., Holweger, 1967); and a synthesis of the two appears to be difficult.

The Harvard-Smithsonian Reference Atmosphere (HSRA) (Gingerich et al, 1971) utilized measurements made above the atmosphere in the ultraviolet and far infrared spectral regions to improve upon the temperature structure of the BCA model, particularly in the temperature minimum region. The minimum temperature of 4170 K is reached at an optical depth $\tau_{5000} = 10^{-4}$, and the region is very narrow, in contrast to the situation in the BCA model. In the computation of the model (Gingerich, 1963), some deviations from LTE in hydrogen and carbon were included, representing an improvement over a purely LTE model. Nevertheless, discrepancies still remained; for example, in some parts of the ultraviolet, close spacing of lines depressed the apparent continuum of observations at the resolution available by an order of magnitude below that predicted from the model. Very few results from lines were included in the HSRA, as in previous models, because of the difficulties of interpretation.

Further measurements, particularly in the ultraviolet and far infrared spectral regions, were included in the Vernazza-Avrett-Loeser (VAL) model (Vernazza et al, 1976). In this model, the temperature minimum region extends from approximately $\tau_{5000} = 1.5$ to 4×10^{-4} , with a value of 4150 K. This low minimum temperature is not in agreement with recent predictions of theoretical models such as those of Kurucz (1974) and Athay (1970); thus, surprisingly, there appears to be greater

difficulty in understanding mechanisms for cooling the minimum region rather than those for heating the chromosphere (Durrant,1978). The VAL model is more general than previous models in the consideration of non-LTE conditions (Vernazza et al,1973). The assumption of hydrostatic equilibrium is made, although that of radiative equilibrium is not, and effects of line opacity in the ultraviolet are considered. The spectra synthesized from the model are found to be in reasonable agreement with continuum observations, but the authors conclude that a contradiction exists between limb darkening and absolute intensity measurements, particularly in the region 1.0 to 2.5 μm , which originates in the deepest observable level of the solar atmosphere. They also remark upon the need to consider effects of inhomogeneities in the atmospheric structure upon observational results, which cannot be duplicated in the model predictions. The temperature structures near the minimum region of the models discussed above are shown in Fig. 2.1.

Attempts have been made to incorporate inhomogeneities into model atmospheres (e.g., Nakayama,1976), but these depend upon assumptions as to the physical nature of the inhomogeneities, and have as yet been very restricted. Nevertheless, it is clear that an adequate description of both disc centre intensity measurements and centre to limb variations requires a several component model, especially in the chromosphere and transition region, and further progress in spatial, spectral, and temporal resolution of observations as well as in the purely theoretical description of physical processes of importance to the structure of the solar atmosphere is necessary before accurate models of the outer layers of the sun can be constructed.

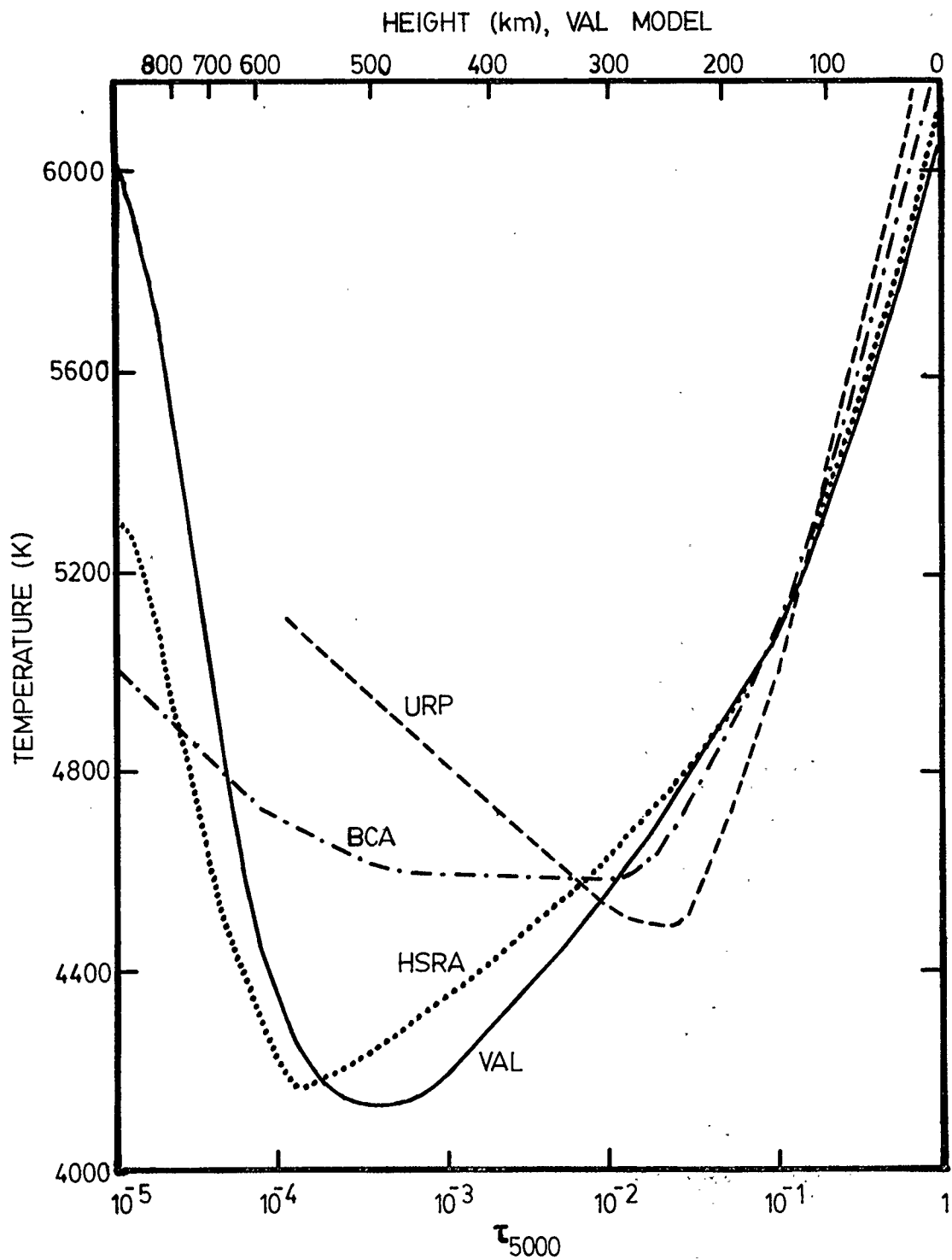


Fig. 2.1 Temperature distribution of the photosphere and low chromosphere as given by several models.

2.3 Summary of Previous Results

The relationship between wavelength and source height in the sun determines uniquely which layers of the solar atmosphere can be observed in any spectral region. Opacity calculations based on homogeneous models predict that far infrared and ultraviolet radiation should originate in equivalent layers near the temperature minimum region. While this prediction suggests that comparisons between limb scans from these two spectral ranges would be useful, the conditions under which the radiation is produced make the interpretation of such a comparison extremely difficult in practice.

In the far ultraviolet, the opacity varies rapidly with wavelength since the spectrum consists largely of line emissions, and thus the source height dependence upon wavelength will be extremely complex, varying across each line and from line to line. In contrast to this complex situation, opacity in the far infrared is dependent simply upon the square of the wavelength, since the source is predominantly the free-free transitions of the H^- ion.

There is also a marked difference between the dependence of spectral intensity upon temperature in these two regions. On the one hand, ultraviolet emission is strongly dependent upon temperature since the Planck function is proportional to $\exp(-h\nu/kT)$ in this region (Frisch, 1972), whereas it becomes a Rayleigh-Jeans relation, with spectral intensity depending only directly upon temperature, in the far infrared.

One further comment upon the interpretation of limb scan results is the influence of inhomogeneities in the chromosphere upon

these results. Information obtained from limb scans in terms of inferred temperature structure in the solar atmosphere has been contradictory and incompatible in general with that from disc centre brightness temperature measurements. Over the past few years this incompatibility has been increasingly interpreted in terms of the presence of inhomogeneities in the chromosphere, particularly with respect to far infrared and radio results. Macroscopic roughness as a mechanism for suppressing expected limb brightening can be predicted to have similar effects on limb scans in both the far infrared and the ultraviolet, while different behaviour would be difficult to interpret solely on the basis of surface roughness.

2.3.1 Ultraviolet Results

In the ultraviolet, the region of transition of the spectrum from predominantly absorption to mainly emission lines near 150 nm delineates a change of origin of the continuum from below to above the temperature minimum. Tousey (1963) has reviewed early measurements of the solar EUV spectrum including centre to limb measurements. In the wavelength range 208.5 to 170 nm, slight limb darkening is present in the continuum while limb brightening appears in the emission lines. Below 175 nm a continuum becomes hard to define, particularly in low resolution data, but this appears to show neither limb darkening nor brightening as far as 152.5 nm. At this point, conspicuous limb brightening does appear, indicating a source height near the bottom of the chromosphere, if homogeneity of the source is assumed. It appears from the published data in this spectral range that these are only very broad characteristics and that the shape of the limb scan can vary dramatically

even over short wavelength ranges. For example, Bonnet and Blamont (1968) detected a distinct discontinuity in the limb darkening function between 198 and 219 nm. Values of the coefficients of limb darkening at various wavelengths have been obtained recently by several workers, for example Samain (1979) from rocket spectra between 140 and 210 nm, and Moe and Milone (1978) from Skylab data for wavelengths 194.5 to 324.5 nm. Comparison of the observed limb darkening with that predicted by the HSRA model was done by Samain et al (1975) between 120 and 210 nm who found poor agreement overall. For example, limb brightening is predicted below 168.3 nm, while darkening is still measured to 160 nm, and an extra, unknown source of opacity was found necessary down to at least 158 nm. The range of wavelengths over which little limb darkening or brightening is seen has been interpreted as indicating a flat temperature minimum region, broader than that inferred from models such as the Utrecht Reference Photosphere or BCA (Gingerich and Rich, 1968). These authors also discuss the possibility that the temperature minimum region is not observable at all in the ultraviolet because of an abrupt change in opacity produced by an absorption edge of Si I (1D), which changes the effective emission height abruptly over a short spectral region. For this reason, comparison between ultraviolet and far infrared results may not be either relevant or useful. However, Samain et al (1975) claim that the temperature minimum region is observable near 158 nm. These ambiguities serve to emphasize the difficulty in interpretation of spectral data when atomic line transitions determine the overall opacity.

2.3.2 Visible and Near Infrared Results

In the visible and near infrared regions of the spectrum, the limb darkening function is well known and well-behaved (Allen, 1973; Zirin, Ch. 10, 1966; Pierce and Slaughter, 1977; Pierce et al, 1977), and these data have been included in models of the solar atmosphere. However, high resolution observations close to the limb during eclipses have revealed unexpected features, and Kurokawa et al (1974) discuss both their own continuum data from flash spectrograms obtained during the 1970 eclipse and earlier data by Heintze and Tanaka and Hiei in which small increases in brightness were seen near the limb, in contrast to results of Kristenson and of Weart, discussed in the same paper, which show no such increase. Measurements of limb darkening in lines of high opacity in this wavelength region have been used to determine the solar minimum temperature. For example, White et al (1972) compared the intensity of the forbidden Mg I line at 457.11 nm at $\mu = 0.125$ with that of the nearby continuum to derive a minimum temperature value of 4190 ± 50 K. This result would of course be subject to systematic error if suppression of limb darkening were to occur for the line but not for the continuum because of irregularities existing preferentially at the higher source height of the line.

Near infrared measurements are continuations of those in the visible, in the sense that ground-based telescopic limb scans can be made in which diffraction is not yet a significant limitation, although it begins to dominate atmospheric fluctuations as a limit to resolution. The early measurements of Pierce et al (1950) from $\mu = 1$ to 0.16 show a decrease in the amount of limb darkening from 3.5 to 10.2 μm , which

is qualitatively consistent with the increase of opacity with wavelength and source heights below the minimum region. Léna (1968) obtained limb scans from 10 to 25 μm , over the range of angles $\mu = 1$ to 0.14 (11 arcseconds from the limb) using the 158 cm McMath Solar Telescope at Kitt Peak, and attempted to deconvolve the effect of the scanning slit. Comparison of the data with predictions derived from the Utrecht model, modified by filtering and smearing to simulate expected effects in the data, shows the absence of the expected brightening. Below 15 μm , the predicted curve lies below the observed values, while above 17.9 μm the trend is reversed. Later measurements (Léna, 1970) extending the previous results to within $2''$ of the limb at 5, 10, and 20 μm , show reasonable agreement with the BCA model in the lower atmospheric layers but require lower temperatures in the higher layers. Also, the results at 10 and 20 μm appear to be inconsistent, and an extra source of opacity at 20 μm was postulated by the author to resolve this problem. Johnson (1971) obtained limb scans at five wavelengths between 2 and 20 μm to μ better than 0.05, from which an increase in intensity at the extreme limb can be inferred. However, there is some uncertainty in this conclusion because of the possibility of misalignment of the limb and the presence of plage regions. A normal limb darkening characteristic cannot therefore be ruled out. Noyes et al (1968) have obtained the solar intensity distribution both by limb scanning and eclipse measurements. The mean remaining intensity values derived from the November 1966 eclipse data at 22.5 μm decrease slightly toward the limb, with slope $-0.005 \pm 0.005/\mu$ for limb separations less than $10''$, thus indicating limb darkening. This conclusion is uncertain

due to the presence of variation of sensitivity with position in the detector slit, despite efforts to locate the slit at a position angle chosen to cause minimum loss of resolution from lunar limb structure and distance off the sun - moon centre line. The shape of the eclipse curve can be fitted either to a flat or limb darkened distribution, but is not consistent with limb darkening as predicted by the URP model. North-south scans obtained by the authors at 22.5 and 24.3 μm using the 1.5 m LPL telescope yield a slope of intensity of $-0.06 \pm 0.07\%/^{\circ}$ at 40° inside the limb, with indirect evidence from the asymmetry of the instrumentally smoothed profile that there is still darkening to within 10° of the limb. These results were important in the modification of the temperature minimum structure of the URP to form the BCA model. Mankin and Strong (1969) used a balloon-borne 38 cm telescope to obtain limb scans from 11 to 115 μm above the majority of the atmosphere. After correction for the scanning function, the results agree with the BCA model for wavelengths below 70 μm , but show a sharp decline in the solar temperature for longer wavelengths. Slight brightening at 31 and 52 μm could be inferred, but does not permit a smooth curve to be fitted to the entire spectrum, so probably is not real. Qualitatively, darkening appears to persist over all the wavelengths, decreasing in magnitude toward 115 μm , thus indicating that the source heights for these wavelengths are still below the temperature minimum region.

2.3.3 Far Infrared and Submillimetre Results

Very few limb scans have been obtained in the far infrared spectral region, because the earth's atmosphere is almost completely opaque to this radiation apart from a few poor windows, thus requiring

that the measurements be made from aircraft, balloons, or high mountain sites. Righini and Simon (1976) obtained drift scans at 350 and 450 μm to $1''$ resolution using the 2.2 m telescope at Mauna Kea, which show some indication of limb brightening, although the results are not inconsistent with a uniform distribution to within 1%. Lindsey and Hudson (1976) used the 1.5 m telescope on Mount Lemmon to obtain dual-beam differential scans at wavelengths between 350 μm and 1 mm. The radial limb brightening seen has a functional dependence of the form

$$\frac{I(r)}{I(0)} = 1 + (0.017 \pm 0.0034) \left(\frac{r}{r_0} \right)^2 ,$$

in contrast to the HSRA form approximating

$$\frac{I(r)}{I(0)} = 1 + 0.048 \left(\frac{r}{r_0} \right)^2 .$$

Thus the predicted limb brightening is three times that observed, with the discrepancy increasing toward the limb. The authors speculate that this discrepancy could be accounted for by the presence of irregularities which would have the effect of enhancing disc centre brightness slightly and suppressing limb brightening, apart from a spike at the limb which would not be resolvable in their data. Ade et al (1971) obtained a series of scans of the sun to $3''$ resolution at constant declination with the 1.05 m telescope of the Pic-du-Midi Observatory, for purposes of mapping active regions. The maps, at passbands of 400, 800, and 1200 μm , were not deconvolved with the telescope beam pattern, and therefore the detailed intensity distribution at the limb could not be determined. However, the positions of isophotes of half central intensity were used to infer the presence of limb brightening, of amount increasing toward the longer wavelengths. Further analysis of this data (Beckman and

Clark, 1973) led to the conclusion that no normal limb brightening is present in the data, but that the 50% isophote implies a narrow spike of intensity close to the limb. An attempt was made to deconvolve the maps with the instrument function, but the presence of residual effects at the limb makes identification of such a spike inconclusive. Some drift scans were also obtained, but were not deconvolved. These are difficult to interpret because they are distorted by changes in atmospheric emission and transmission during a scan, and by the presence of active regions in the path of the scan. Beckman et al (1975) measured second and third contacts during the June, 1973 eclipse from a Concorde aircraft, in which the duration of chromospheric visibility was extended greatly, resulting in high spatial resolution at good signal to noise ratio. Analysis of the shape of the eclipse curve showed the presence of an intense spike extending from $5''$ inside to $4''$ outside the optical limb, with brightness temperature constant for all three passbands (400, 800, and 1200 μm). The detailed shape of the spike was used to derive physical characteristics of spicules below 3000 km assuming that these are the cause of the spike and that the remainder of the chromosphere can be represented as a rough emitter (Beckman and Ross, 1976). Unfortunately, only $19''$ of the solar disc was observed, and thus the result is highly dependent upon knowledge of the location of the limb, the speed of the eclipse relative to the aircraft at all times during the measurement, and especially upon extrapolation of the data to disc centre or a calibration method, which unfortunately is not described by the authors. The amount of energy contained in the spike, roughly 3 - 4% of the total disc energy, is significant, and thus should be observable even at resolution lower than the $1.5''$ achieved in this experiment.

2.3.4 Millimetre Results

The radio region is somewhat more easily accessible to observations since the atmosphere is no longer totally absorbing. Source heights for radiation within this spectral region are above the temperature minimum and increase with wavelength until only the corona is seen, in the centimetre region. The observations are severely limited by diffraction; therefore measurements to high resolution must be made either with large telescopes, using interferometric techniques, or during an eclipse. The 1.5 m telescope at Queen Mary College was used to obtain solar scans during the May, 1966 partial eclipse (Clegg et al, 1969; Newstead, 1969) at 1.2 mm wavelength. A value for mean disc temperature of 1.11 ± 0.03 times central temperature was derived, which indicates a substantial degree of limb brightening. The detailed shape of the intensity distribution could not be derived due to inadequate resolution. Noyes et al (1968) used a 1.5 m antenna of the NRAO at an effective wavelength of 1.2 mm for drift scans of the sun, which were corrected approximately for the instrument function, whose shape was not known in detail. Limb brightening was inferred from the ratio of 1.14 ± 0.03 between the area under the measured curve to that expected from a uniform sun, although systematic errors could arise if either the sun or the antenna pattern were not circularly symmetric. The ratio would be an overestimate if the antenna pattern had been sufficiently wide to lower central intensity; however, the inferred width was small enough to make this occurrence improbable. Kundu (1971) used the 11 m NRAO radio telescope to obtain both equatorial and polar limb scans at the same wavelength, which were corrected for beamwidth. In contrast to

the previous results, these scans show definite limb darkening, more pronounced in the polar than equatorial direction. A later reanalysis of this data (Kundu and Liu, 1975) showed no evidence for either a uniform or limb brightened distribution, in response to criticism that the appearance of limb darkening was due to the use of an inadequate deconvolution function. At a wavelength of 1.4 mm, Shimabukuro (1971) sees little if any limb brightening on scans obtained with a 4.6 m antenna. Ade et al (1974) used the 11 m NRAO telescope to obtain scans over a 0.8 to 1.6 mm bandpass with centroid at 1.4 mm. The telescope beam pattern was measured accurately from single-beam scans and dual-beam differential observations of planets. The deconvolved scans show no limb brightening or darkening to within 3%, in contrast to earlier results obtained with the same telescope. Bastin et al (1964) obtained a solar intensity pattern at 1 to 4 mm by observation with a 1.65 m telescope of sunrise over a knife-edged mountain, and compared the data with that calculated assuming a circularly symmetric sun with uniform intensity distribution apart from a narrow ring at the limb. The fraction of total energy contained in such a ring was found to be 0.06 ± 0.03 , but the authors do not claim this to be an indication of significant limb brightening because of the possibility of systematic errors arising from factors such as diffraction at the mountain, difference between mountain and sky background levels, the finite angle subtended by the telescope at the mountain, and the beam pattern of the telescope. A recent eclipse measurement by Labrum et al (1978) at 3 mm showed the presence of slight brightening at the limb. Earlier eclipse measurements at 3.2 mm (Hagen et al, 1971; Swanson and Hagen, 1975) showed limb

brightening which does not correspond with that expected either in position or in shape. At the 1970 eclipse, a double peak $1 - 2''$ inside the limb of height 30% above central disc temperature was seen, while the 1973 eclipse data showed strong limb brightening with a different detailed structure, lacking the double peak. In both cases, the rough nature of the emitting surface was apparent from intensity variations of the order of 10% of the average brightness across the disc. Limb scans at 3.4 mm to a resolution of $2.8''$ obtained by Shimabukuro and Stacey (1968) indicated a flat intensity distribution to $r/r_0 = 0.7$, with a slight rise thereafter. The June, 1973 eclipse was measured at 3.3 mm by Shimabukuro et al (1975) who found a total limb brightening of less than 2% of the uniform sun flux, but of the order of 20% brightening within $0.5''$ of the limb. The eclipse measurements of Simon et al (1970; Simon, 1971) at 3.3 and 3.5 mm appear to be inconsistent with a narrow spike of intensity at the limb, placing an upper limit of 1% on the power that could be contained in an annular spike of width $0.03 r_0$ or less. The data show less limb brightening than predicted by the BCA model, with 1% darkening in an annulus of width $0.02 r_0$ giving a better representation of the data than equivalent brightening or a uniform disc. The complex character of the intensity distribution seen by Hagen et al was not observed. Fluctuations of 20% at 3.5 mm and 5% at 3.3 mm on the derived solar shape are interpreted as indications of the rough nature of the emitting region. The scans obtained by Lantos and Kundu (1972) at 3.5 mm indicate an essentially uniform distribution across the sun, with slight limb darkening. Measurements at longer wavelengths have continued the trend of showing less limb brightening than predicted by homogeneous models. The classic result is the eclipse measurement

of Coates et al (1958) at 8.6 mm, which showed an essentially flat distribution, with a possible spike at the limb. Lantos and Kundu (1972) measured limb brightening at 9 mm in both the polar and equatorial directions, of magnitude 8% above central intensity, while Hagen et al (1971) saw an indication of a double peak from an eclipse measurement at 8.3 mm. Some of the millimetre results have been used as the basis for a model incorporating a chromospheric temperature inversion (Neidig, 1973), but in view of the contradictory nature of many of the results, further data are necessary before the need for such a model can be evaluated.

2.3.5 Summary of Observations

The preceding summary gives an indication of the lack of agreement between various results arising from the difficulties inherent in the measurement and interpretation of centre to limb scans. All but two of the observations (Mankin and Strong, 1969; Beckman et al, 1975, 1976) were made either from the ground or at mountain altitudes, with the accompanying problems of wavelength restriction (most noteworthy here is the scarcity of measurements between 25 and 300 μm) and signal noise due to atmospheric transparency and emission fluctuations, which Léna (1968) reports to be as large as 30% with time scales of 10 minutes, at intermediate infrared wavelengths. All non-eclipse scans at these long wavelengths suffer from poor spatial resolution, limited usually by diffraction.

Although most authors attempt either to deconvolve the scan with an approximation to the telescope or antenna beam pattern or, equivalently, to convolve a predicted curve with this pattern, in general

an uncertainty remains which worsens toward the limb. Further complications to the deconvolution technique arise if the location of the solar limb is not known precisely. Therefore eclipse measurements serve to increase the maximum spatial resolution as well as to extend the measurements much closer to the solar limb. A further potential source of error is the presence of active regions, which when found on the limb may produce a spurious limb brightening. Isophote mapping has shown the existence of submillimetre features which are up to 10% brighter than the mean (Beckman and Clark, 1971), with some indication of a relatively flat spectrum for active regions (Righini-Cohen and Simon, 1977). Their presence must of course be taken into account in the interpretation of limb scans.

Apart from the consistent absence of limb brightening of the magnitude predicted by homogeneous models over all wavelength ranges (Simon and Zirin, 1969), one feature which has been reported several times is the spike of radiation at the limb. The most noteworthy observation of this spike was that of Beckman et al (1975), but other observations are not consistent with the presence of such a spike. Therefore further measurements, particularly during an eclipse, are important to check the existence of this limb structure and determine its origin, and to provide data on the inhomogeneity of the chromosphere and the nature of the structures comprising this inhomogeneity.

CHAPTER 3

EXPERIMENTAL DESIGN

3.1 Introduction

The design of the instrumentation for the proposed experiment was carried out after careful consideration of the basic limitations which have been referred to previously and of the very specific conditions imposed upon the experiment by the approach to be used. In particular, the small size of the Lear jet and its limited range required careful consideration during the initial operational design phases of the experiment.

As outlined earlier, the traditional methods of solar limb scanning outside eclipse require a precise knowledge of both the spatial instrument scanning function and the instrument orientation relative to the solar centre. This first parameter is simple to determine at short wavelengths, where diffraction at the telescope aperture is not severe. In such cases, a small, well-defined aperture can be used to make scans to a resolution limited only by atmospheric fluctuations. In practice, this limit is found to be of the order of $1''$ at visible wavelengths but may be somewhat better at near infrared wavelengths. At longer infrared and submillimetre wavelengths this scanning function becomes considerably broadened by diffraction and hence more difficult to define and determine experimentally. Furthermore, the influence of this function must be removed from observed scans by deconvolution in order to produce high resolution centre to limb intensity distributions. This process is difficult to carry out in practice and can lead to instrumental artifacts

in the final data unless extreme care is taken in the determination of the scanning function and in the subsequent deconvolution.

The second requirement, knowledge of the instrument orientation, can be met easily at ground-based observatories but becomes more difficult in the more hostile environments encountered in aircraft or balloon experiments. In these situations, uncertainty in the position of the scanning beam with respect to the sun caused by vibrations or steering system fluctuations induced by movement of the vehicle can limit the attainable spatial resolution of the measurement.

Each of these difficulties can be minimized by utilizing the opportunity of an eclipse observation. The moon in this case acts as an essentially diffraction-free shutter which passes in front of the solar disc. The resulting overall intensity change, if precisely timed, can be transformed into a high resolution scan of the solar disc which is unaffected by diffraction even at the longest wavelengths, provided that certain specific precautions are taken in the instrument design.

The first problem, that of providing a small and well-defined aperture, has been partially removed since the moon will now perform a sequential scan across any aperture provided. At short wavelengths this can be a well-defined slit such as that used by Noyes, Beckers, and Low (1968) in the intermediate infrared, and this slit can be placed across the limb to provide enhanced sensitivity to changes over this important but limited part of the solar disc. The observed eclipse intensity change in this case will of course be influenced by the aperture shape at all wavelengths, and at very long wavelengths the effective aperture shape will be significantly modified by diffraction.

Deconvolution of this equivalent aperture shape will again be required, and this considerably reduces the usefulness of the limited aperture. It is therefore necessary to ensure that both the full image of the sun and as much as possible of its diffraction pattern are included in the instrument field of view.

In the present submillimetre experiment, the parameters were chosen to ensure that any radiation from the moon was also included in this field of view, at least over the limited time of the measurement around eclipse totality. This aperture size must include the extent of any expected steering or vibrational excursions of the image to minimize modulation of the detected signal by such movements. In the present experiment, these criteria were relatively restrictive, particularly when the other limitations of the Lear Jet aircraft, such as limited window size and interior space for the instrumentation, are recognized. The optical arrangement eventually used is described in the following section.

3.2 Infrared Photometer Optics and Alignment Tests

The field of view of the optical telescope (of which two were utilized in the instrument, in parallel) was chosen to be 64° or two solar diameters, and was defined by an aperture at the focal plane of the 54 mm diameter f/8 primary mirror. The parameters of this primary optical element were determined by the basic requirement that the primary mirror be imaged onto the 1 mm detector cavity entrance by a 7.6 mm f/1 field lens placed at the field stop. The rather long focal length was dictated to some extent by the necessary beam length within

the vacuum enclosure of the liquid helium cryostat, inside which cold filters, the 7.6 mm field aperture and the field lens were contained. With this field of view, changes in signal level because of steering fluctuations caused by aircraft motion were expected to be small.

A schematic diagram of the optics of one telescope is shown in Fig. 3.1. Submillimetre radiation from the sun entered the aircraft through a specially designed 25 mm thick low density polyethylene window 400 mm in diameter, mounted in the emergency door of the aircraft. This radiation was automatically guided to the instrument at all times during solar observations by a gyroscopically controlled heliostat. (Gyroscopic rather than optical solar pointing control was obviously essential in order to maintain the correct viewing direction even in the absence of visible light during eclipse totality.) This radiation fell onto a 45° plane mirror M_1 , adjustable in height to allow for the change in elevation angle of the sun during the eclipse and to prevent vignetting of the radiation by the relatively limited aperture of the external window. The aircraft trajectory was carefully chosen to eliminate variation in azimuth of the sun with respect to aircraft axis and to minimize elevation change, as discussed in 3.6, but this adjustable optical element was still found to be necessary. M_1 then fed the radiation down onto a four-blade reflective aluminum chopper whose alternate blades were milled and lapped with an angle of 0.84° between them. This blade was left intentionally unpolished to provide a certain measure of rejection of visible and near infrared radiation by scattering, while reflecting the required long wavelength radiation. This blade thus moved the telescope field of view by 1.68° on the sky, and phase-sensitive detection of the resulting alternating signals provided an effective

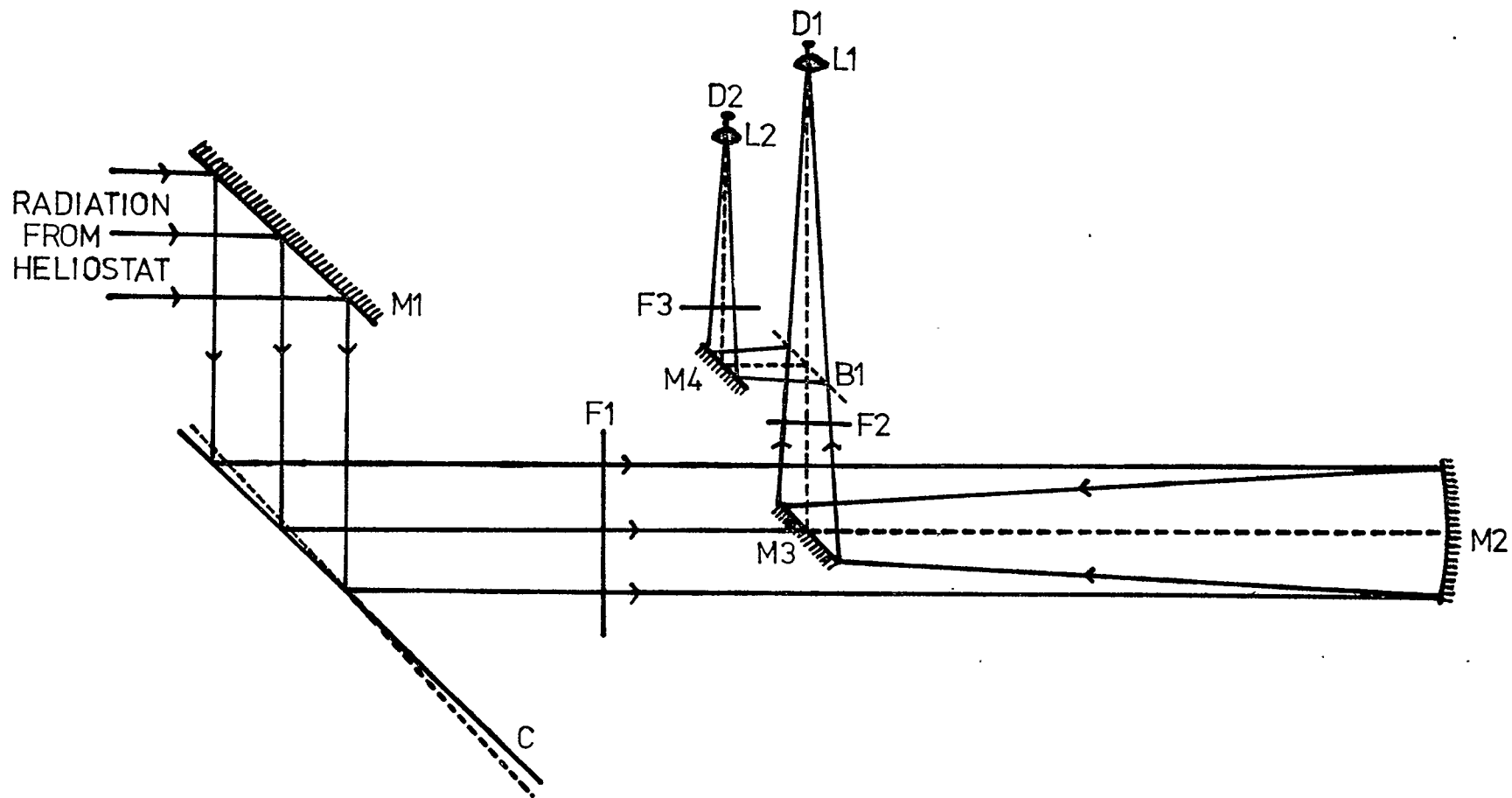


Fig. 3.1 Optical system of one dual-channel photometer.

subtraction of radiation from sources other than the sun and moon, such as the aircraft window or the atmosphere. The throw of 1.68° ensured that none of the contribution to the signal from lunar radiation was subtracted by the chopping, even at first and fourth contacts. The f/8 primary mirror focussed the radiation via the Newtonian secondary into the dewar and onto the two field lenses L_1 and L_2 after it was either reflected or transmitted by the beamsplitter B_1 . Optical alignment of the system ensured that these images fell in the centres of the two field lenses, while these lenses were positioned to image the primary optical mirrors onto the detector cavity entrances. The detectors, Ge(Ga) bolometers, either single crystal or composite, were mounted along with the lenses and apertures upon detector turrets on the liquid helium cold surface. These detectors, supplied by Infrared Laboratories Inc., were mounted inside collecting cavities behind 1 mm apertures and operated at temperatures below the lambda transitional temperature of liquid helium (at which vigorous boiling ceases) by pumping on the liquid surface with a high-flow vacuum pump installed in the aircraft.

Filtering of the radiation to specific wavelength bands was accomplished in separate channels by long wave pass mesh filters, F_2 and F_3 (Cambridge Physical Sciences), and collectively by a black polyethylene filter F_1 at the photometer entrance. Absorption in the polyethylene window, filters, and the Mylar beamsplitter, and scattering at the chopper blade modified these spectral passbands somewhat, as described in 3.3.

The second optical channel was designed to be identical to the first, but viewed the chopper blade at a different position and utilized a different section of the aircraft window. It was hoped that the choice

of cut-on filters in each of the four channels would permit the definition of several narrower channels indirectly by subtraction of signals during the data analysis.

Optical alignment and initial sensitivity tests of the fully assembled instrument were carried out in January using the 150 mm Carson heliostat of the Rothney Astrophysical Observatory. Filter combinations were initially chosen during these tests using artificial sources, and included two narrow-band filters which were selected with passbands in significant windows of the remaining atmospheric absorption above the aircraft altitude. Attempts were made to detect solar radiation through the very weak transmitting windows of the atmosphere, but light cirrus clouds and the small optics dictated by the eclipse requirements combined to make this test impossible.

3.3 Energy Considerations and Filter Requirements

Choice of filters for each of the submillimetre channels was determined to a large extent in this detector sensitivity limited spectral region by the responsivity of the detector and the required resolution at the solar limb. A further significant criterion is the rejection of near infrared and visible radiation. A representative parameter for describing the expected performance of a photometer channel is the angular distance of the moon from the second contact position at which the signal to noise ratio would be expected to reach unity. For the estimation of this parameter, it was necessary to calculate the expected eclipse curve for the geometry of sun and moon for this eclipse, and to combine the expected radiation flux with filter and detector characteristics.

For the simplified case of a moon eclipsing a uniform, non-limb darkened sun having the expected geometry of this eclipse, the observed intensity as a function of moon position is directly proportional to the area of remaining exposed solar disc and can be predicted by the method described by Hagen and Swanson (1975). However, in order to represent solar radiation distributions other than the "flat" sun, an algorithm was designed and programmed into the CDC Cyber 172 computer, in which any radially symmetric distribution of intensity on the sun could be approximated to a function, and the resulting eclipse curve in this case computed by a convolution technique. The results of these computations are used extensively in Chapter 5 but the simple "flat" sun distribution suffices for the present instrument performance estimate.

The total amount of radiant energy reaching a given detector also depends upon the overall filter combination in that channel. These filters are listed in Table 3.1 with the alternative filters where applicable for the separate channels. Transmission curves for the filter combinations for each channel were derived from available data in the literature or from the manufacturer's specifications, and Fig. 3.2 shows the energy as a function of wavenumber expected to arrive at each detector from the sun, assuming it to be a uniform blackbody of temperature 5260 K.

Table 3.2 contains a summary of the expected detector and overall system characteristics for the final flight configuration and includes the parameter introduced earlier. As can be seen, the signal to noise ratio for a time constant of 0.1 second (used in flight in the

TABLE 3.1

FILTERS IN THE RADIATION BEAMS

1. 25.4 mm low density polyethylene aircraft window
2. 25 μm black polyethylene filter (F_1)
3. 25 μm Mylar¹ beamsplitter (reflection or transmission)
4. Low pass mesh filters in 3 channels
(cutoff wavenumbers 110, 67, 33 cm^{-1})
5. 2.5 mm TPX² dewar window
6. 150 μm black polyethylene (~ 100 K)
7. 1.2 mm quartz (two thicknesses, ~ 100 K)
8. 100 μm garnet-diamond dust scatter filter

1 - Mylar is the trade name for polyethylene terephthalate used by E.I. du Pont de Nemours and Co. in North America; in Europe it is known as Melinex.

2 - TPX is the trade name for poly-4-methylpentene-1 of Mitsui Petrochemical Industries Ltd. The material used for this experiment was manufactured by ICI (U.K.) Ltd.

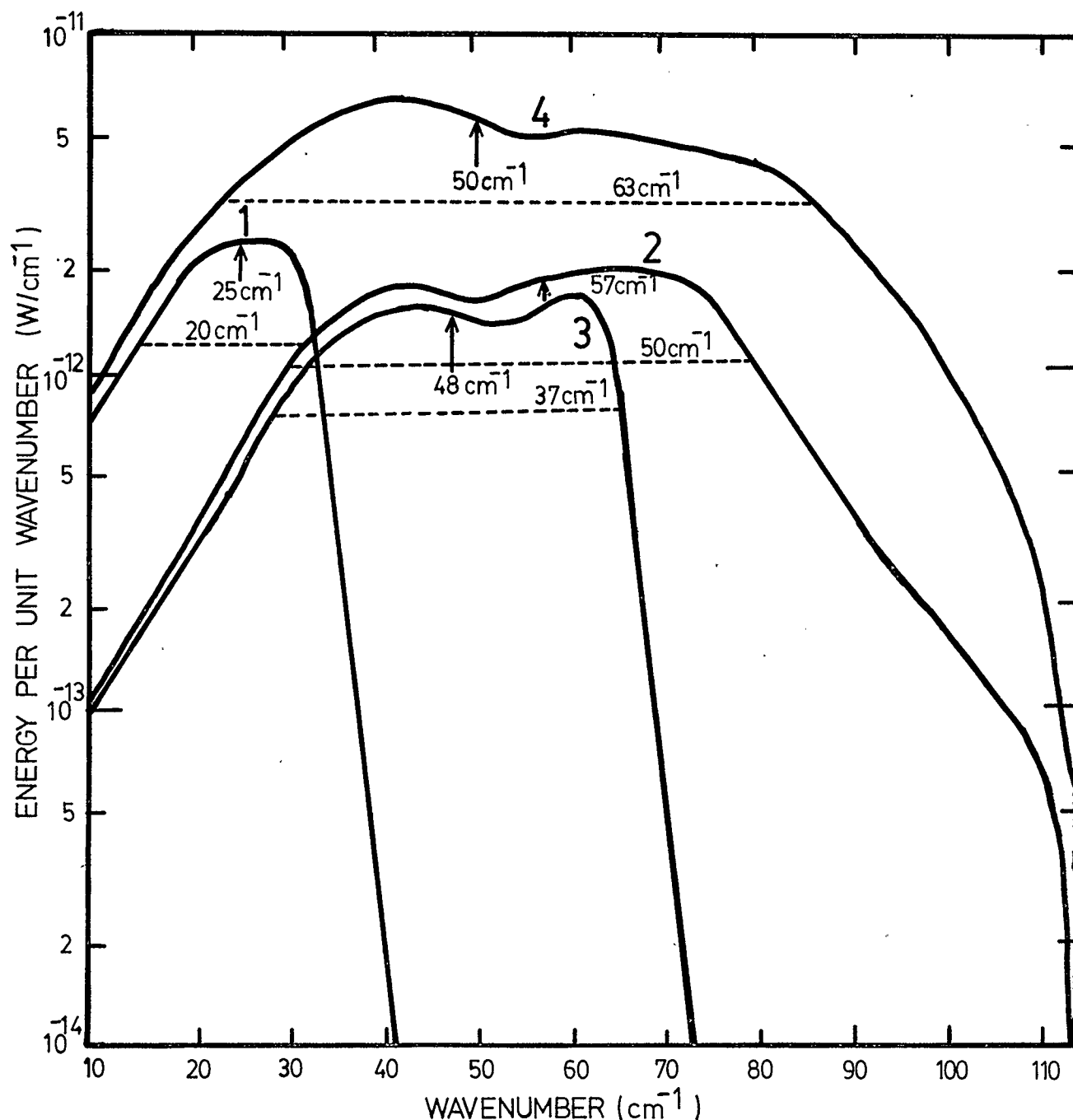


Fig. 3.2 Energy per unit wavenumber from from a 5260K equivalent blackbody reaching the detector in the four channels. Effective wavenumber and full width half maximum are indicated.

TABLE 3.2

INFRARED SYSTEM CHARACTERISTICS

Channel	1	2	3	4
Effective Central Wave-number (equal energy to either side), cm^{-1}	25	57	48	50
Filter Width (FWHM), cm^{-1}	20	50	37	63
Power onto Detector from full sun, W	5×10^{-11}	1×10^{-10}	6×10^{-11}	4×10^{-10}
Detector Responsivity, V/W	9.4×10^5	8.2×10^5	7.1×10^5	5.5×10^4
Detector Noise for 10 Hz Bandwidth, W	1.0×10^{-13}	1.0×10^{-13}	1.3×10^{-13}	1.6×10^{-12}
Signal to Noise Ratio for full sun	500	1000	500	250
Separation of Sun and Moon for Signal to Noise Ratio of 1, $^{\circ}$	3	1.5	3	6

phase-sensitive detection systems) would be expected to reach unity at about $3''$ from second contact for a uniform sun, while this would be decreased to better than $1''$ for a time constant of 1 second, assuming that detector noise is the sole contributor to the overall noise level. This degradation of time constant would represent an equivalent reduction of angular resolution for this eclipse experiment to approximately $0.5''$, the matching of these two angular parameters representing an acceptable compromise if not an ideal situation for the present experiment.

3.4 Helio-stat System and Auxiliary Optics

A gyroscopically controlled heliostat provided for the experiment by NASA Ames Research Center, consisting of an elliptical 0.5×0.3 m mirror gimballed to rotate about two orthogonal directions, guided the solar beam from the polyethylene window into the photometer in a direction parallel to the aircraft axis. Manual control of the gyroscopic steering was provided for initial acquisition and control of slow image drifts. The heliostat was mounted on a slide parallel to the aircraft axis to provide the ability to move the system to avoid vignetting of the beam at all times during the flight. An auxiliary optical system fed by visible light from a small 50 mm optical window adjacent to the infrared window was used for acquisition and monitoring of the solar image position during flight. A schematic diagram of this system, which was attached to the side of the chopper box, is shown in Fig. 3.3. Light from the heliostat is directed by mirror M_5 (which is parallel to and can be moved vertically with M_1) to a 40 mm f/6 lens L_1 and is then split by beamsplitters B_2 and B_3 into three beams. Two photocells P_1

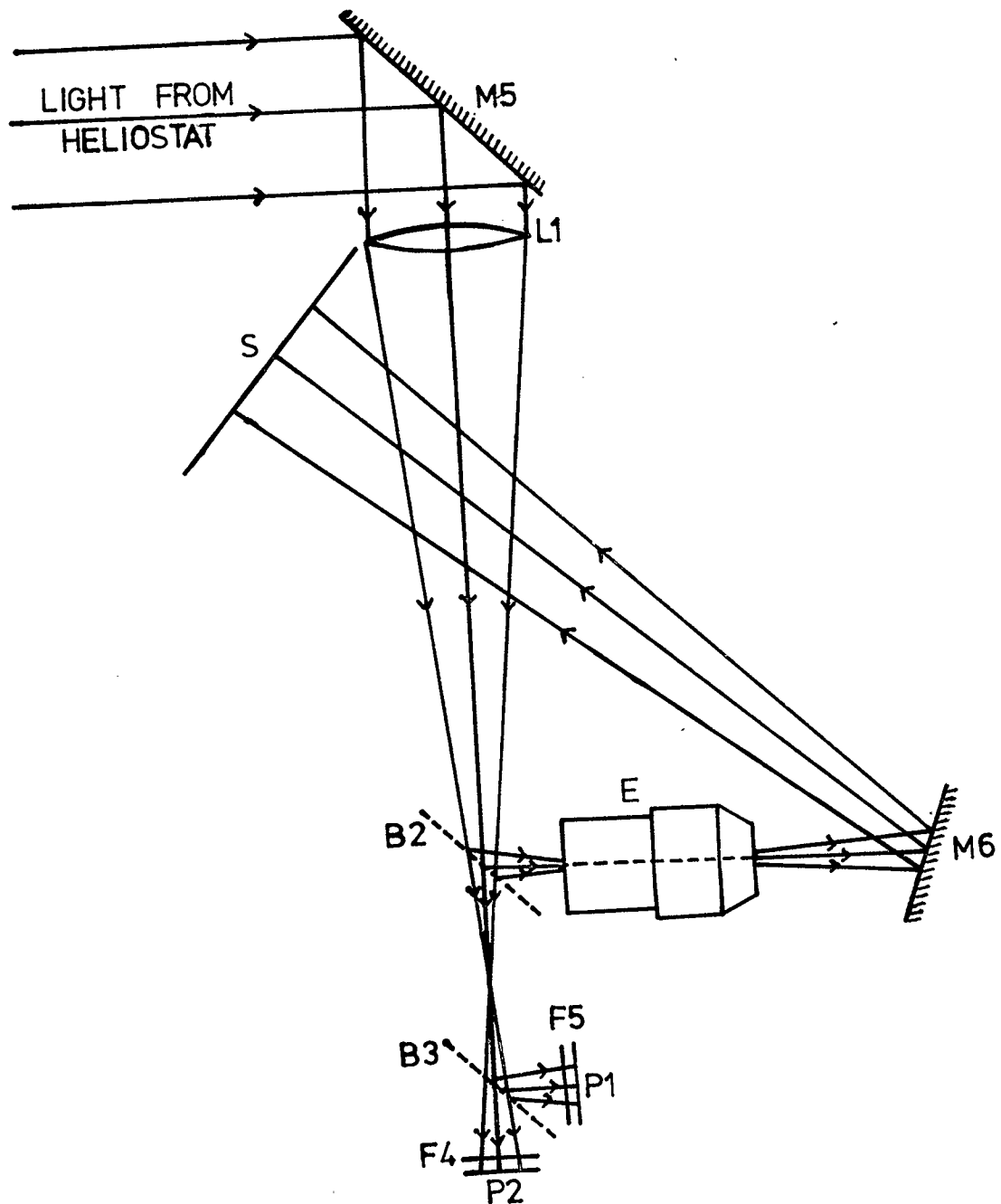


Fig. 3.3 Auxiliary visible system.

and P_2 covered by visible and near infrared filters F_4 and F_5 respectively monitor the eclipse at these wavelengths to provide an optical reference to the progress of the eclipse and timing reference information on the second and third contacts. Eyepiece E in the third beam is used to project a 25 mm solar image onto screen S in a suitable position for providing steering information for the manual correction of the heliostat mirror. The position of this image is uniquely related to the submillimetre images within the helium cryostat. The moment of final disappearance of the image of the sun on this screen at second contact provided a precise timing of this event, and its occurrence was specifically recorded on the voice channel of the auxiliary tape recorder on the aircraft.

3.5 Electronics and Data Recording

Electrical signals produced by the bolometer detectors and amplified by preamplifiers are alternating signals at a frequency of twice the chopper blade rotation rate. Selection of this chopping frequency is governed by several factors. The low frequency limit is set by the desired overall system time constant after phase-sensitive detection, and by the need to adequately cancel atmospheric fluctuations. The high frequency limit is set by detector time constant and by the physical restriction of rotation speed on the 216 mm diameter chopper blade. This blade was mounted on a servo-controlled motor (Electrocraft Corporation Inc., E-550) and the final chopping frequency was chosen during test flights to be 43 Hz, a value at which aircraft vibrations appeared to reach a significant minimum. Phase-sensitive amplifiers (Evans Associates Inc., Model 4110) were utilized to provide

the necessary noise rejection and filtering. A schematic diagram showing the overall electronic system is shown in Fig. 3.4. Phase reference information was provided by two photo-interrupter units mounted 68° apart to monitor the positions of a narrow rim on the edges of alternate chopper blades. This angular separation corresponds to the physical separation of the two regions used on the chopper blade for the infrared beams, and is adjustable to take account of detector time constants and electronic phase delays.

The resulting DC signals from the phase-sensitive amplifiers were transmitted to the two recording systems in two different forms, a direct signal, and an offset and amplified form to provide maximum flexibility and recording precision under all conditions. Fig. 3.5 shows the data recording system used in the experiment. The primary data signals were multiplexed by a pulse-code-modulated (PCM) encoder (provided by NRC Space Research Facilities Branch and programmed for this application by SED Systems Ltd.) which produced eight-bit digital words for up to 30 signals. These signals were encoded into a 32 word frame at a frame rate of 16 Hz to produce a 4000 bit per second serial binary stream for recording on an analogue tape recorder (Revox Ltd., Model A77). Data and offset signals were supermultiplexed to provide sampling at twice this mainframe rate. The offset amplifiers provided a further extension of the digital recording precision which amounted to 3 bits or a factor of 8 on each signal, but required careful attendance when signals were varying rapidly in order to maintain the signal between the upper and lower limits of the offset range. Direct and offset signals were also displayed on meters on the instrument panel

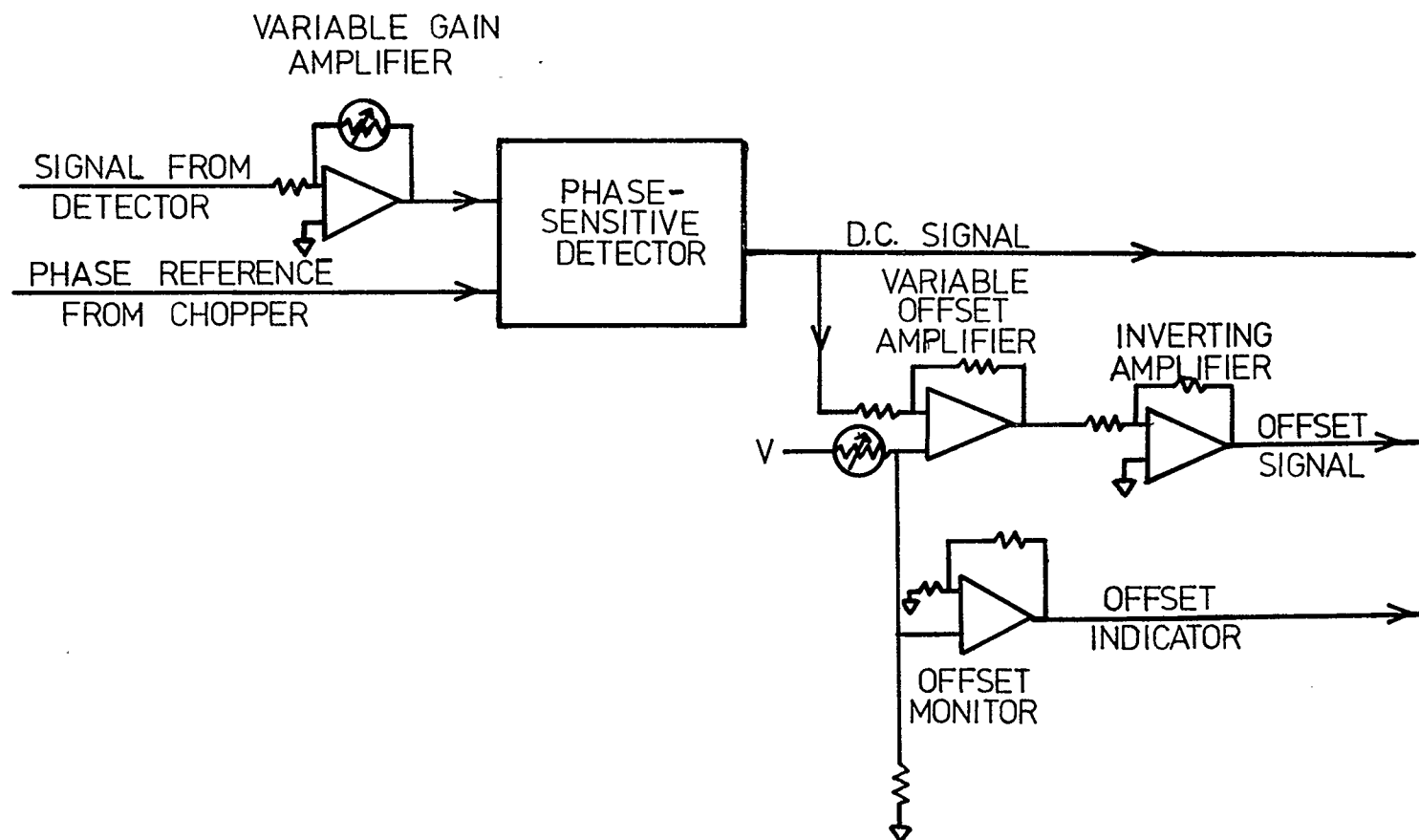


Fig.3.4 Infrared signal electronics, one channel.

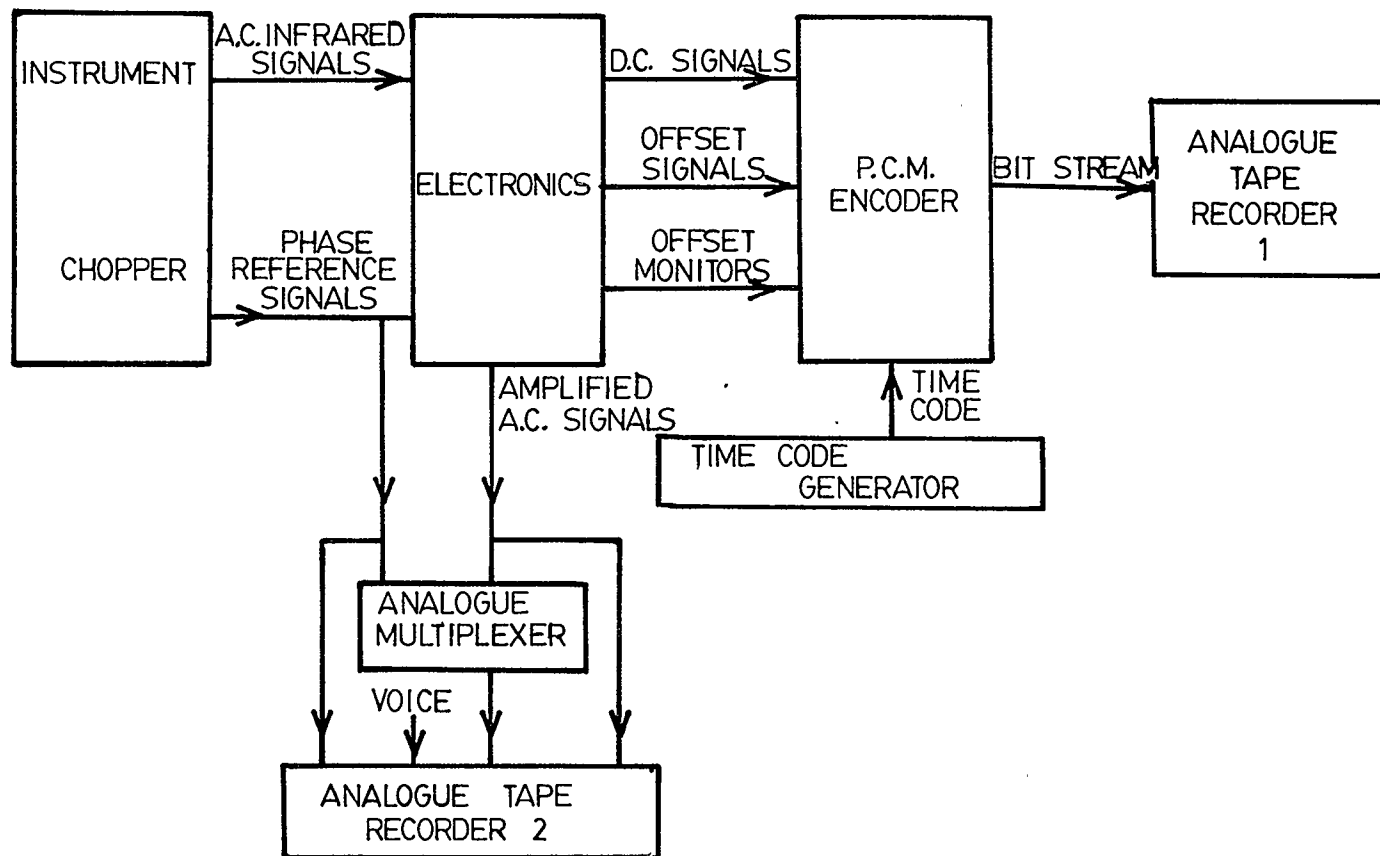


Fig. 3.5 Infrared data recording.

alongside the gain switches of the amplifier to allow the operator to monitor signal levels and optimize the recording levels of all channels during the eclipse flight. A chart recorder was used to record selected signals, and written comments on this chart served as a log book for the flight and as a further monitor of instrument and gain settings. Precise timing information was provided on two digital words of the PCM main frame from a time code generator (Datum Inc., Model 9300). A backup four-channel instrumentation tape recorder (Tandberg Ltd., Series 100) was also utilized to record AC and phase reference signals via a high-speed multiplexer, a selected data channel, its phase reference, and voice recording of comments during the eclipse. This latter facility was of paramount importance in establishing the time (and hence aircraft position) of second contact during the eclipse.

3.6 Optimization of Flight Path

Ideally, it would be desirable to measure intensity from before first contact until after fourth contact, so that the shape of the entire eclipse curve could be used to infer intensity distribution on the sun, while differences between individual contacts could perhaps be correlated with active features near the limb. Data from immediately outside the eclipse is also necessary to determine a normalization point to facilitate comparison with model predictions. Maximum signal to noise ratio for a given resolution is obtained for longest time of eclipse, which implies flight along the central eclipse track. Although the aircraft speed of 425 knots is clearly insufficient to keep up with the lunar shadow, a significant increase in the duration of totality (from 172 seconds maximum on the ground to approximately 240 seconds) can be

achieved. Unfortunately, physical restrictions imposed by aircraft size and range dictated that the flight path differ significantly from the ideal outlined above.

The maximum flight time for the Lear Jet carrying all the necessary equipment and personnel for the observation was somewhat under 2.5 hours, of which approximately 1 hour was required for ascent, descent, and flying in a direction in which the sun could not be observed, to reach an airport. This restriction meant that the entire eclipse from first to fourth contact or, in fact, even half the eclipse, from totality until last contact, could not be observed at flight altitude if the plane were to maintain constant speed along the eclipse path. Also, it was considered undesirable to have central eclipse at either the beginning or the end of the flight because the second and third contacts are potentially the most useful in determining limb structure.

The flight path, chosen as a compromise between the various and sometimes conflicting requirements, was divided into three distinct sections. The first section, spanning half an hour centred on totality, was to be flown to minimize relative speed of aircraft and eclipse; the second, during which observations could not be obtained, was designed to maximize relative speed by flying in a direction approximately perpendicular to lines of equal eclipse time, so that the apparent length of eclipse was shortened sufficiently for the third section, again along the eclipse track, to include fourth contact.

A further constraint on the flight path was necessitated by the small size of the infrared window in the aircraft. The window, inset into the plane, had a clear aperture of diameter 20 cm for normally incident radiation, but this decreased rapidly for other angles because

it was shadowed by the surrounding aircraft body. The size of aperture needed for the two primary optical channels was 11.8 cm horizontally (the direction in which the two beams were adjacent) and 5.4 cm vertically. In order to avoid vignetting, the angle of incidence of the solar infrared radiation to the window must be sufficiently close to normal to allow at least this cross-sectional size of beam, with some additional latitude for steering and navigational excursions, to enter unimpeded. This was a major consideration in flight track design because amount of vignetting would change during the eclipse, thus altering the interpretation of the limb structure by changing the shape of the eclipse curve, as well as invalidating the normalization. A secondary consideration was the possibility of vignetting, from the same causes, of the auxiliary visible beam, leading to confusion in steering and monitoring of the progress of the eclipse.

The resulting flight path during observations was curved in such a way as to maintain a constant angle of 102° in azimuth, since this was the direction of least tolerance in window aperture. Elevation angle varied during the course of the flight, and was compensated for by raising or lowering the feed mirror into the instrument, and by translating the heliostat mirror. Range of variation was approximately 6° , from 24° to 30° , or -6° to 0° to the normal to the window, in the elevation direction. The geographical location of the flight path was chosen to make the curved constant azimuth track coincide as closely as possible with the direction of motion of the lunar shadow, while maintaining the elevation angle within a small range close to normal to the window, and ensuring proximity to suitable airports at the beginning and end of the flight. It was also desired not to overfly large

population centres during totality to avoid interference with ground observations by the aircraft's vapour trail. Fig. 3.6 shows the flight path used, as well as the ferry flight and test flights which were designed to have the same azimuth and elevation characteristics as the eclipse flight.

3.7 Configuration of Equipment in the Aircraft

The overall instrument design and aircraft layout required considerable planning in order to incorporate all the necessary equipment inside the small aircraft cabin and its associated very small baggage compartment, while still keeping sufficient room for two passengers. Figure 3.7 shows the eventual arrangement, while the photographs in figures 3.8 and 3.9 show views from the door and from the pilot's seat respectively, looking toward the rear of the aircraft. The heliostat was placed in front of the polyethylene window in the emergency door, on a precision slide kindly made available for the experiment by Grumman Aircraft Corporation, but was flown in a stowed position forward of this emergency exit for takeoff and landing. Tape recorders and the time code generator were mounted in a small rack aft of the copilot's seat, while the large through-flow vacuum pump was mounted just aft of the door on a special rack. The precision vacuum gauge in the pumping line to the detector dewar was mounted on the wall within easy view of the instrument operator. The instrument and its associated electronics and power converter were assembled on an aluminum plate matching the floor of the baggage compartment. A two-channel chart recorder was included on this plate for real-time monitoring of selected signals by the operator sitting on the back of the folded-down passenger seat. This recorder

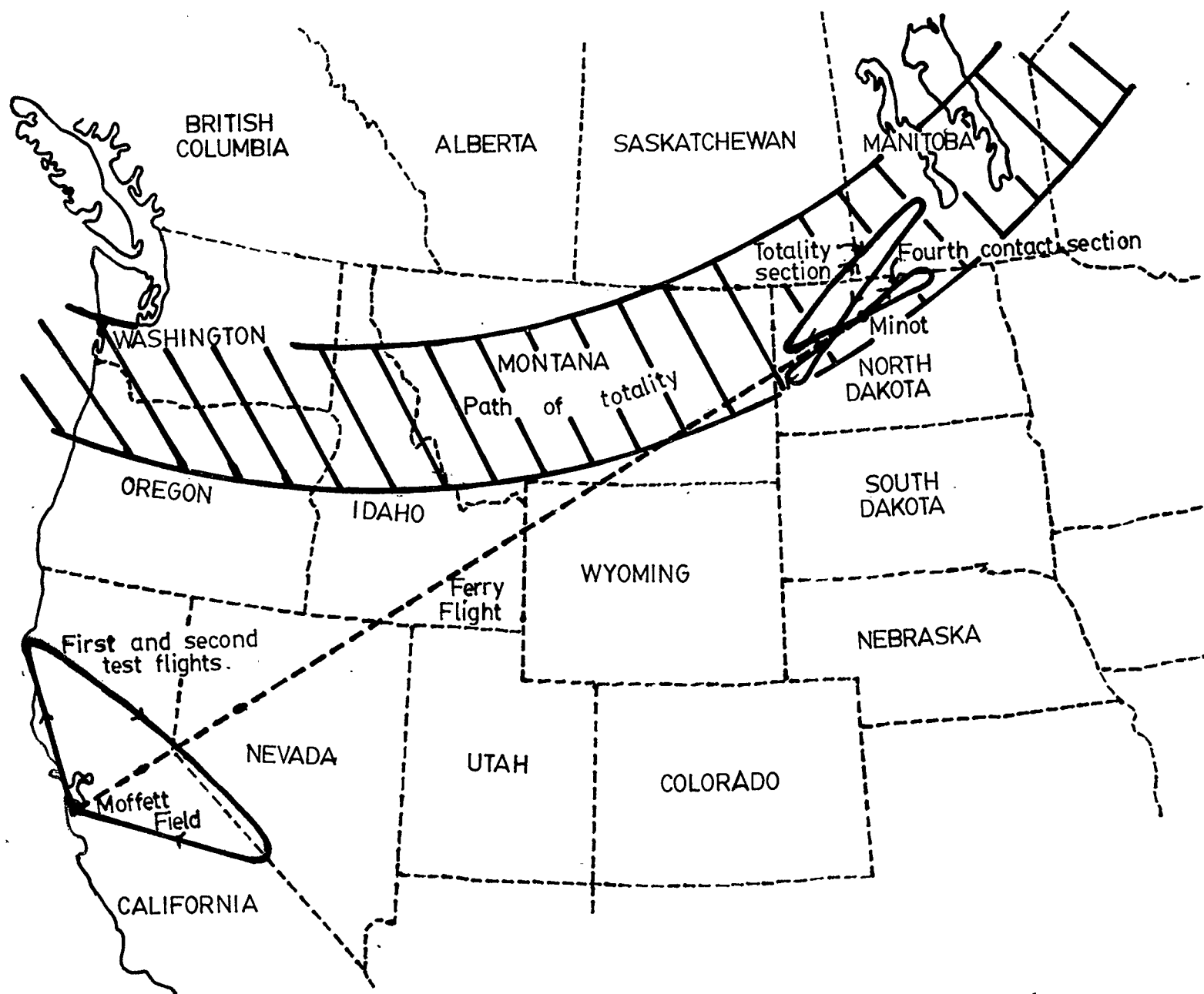


Fig. 3.6 Aircraft flight paths for test and eclipse flights.

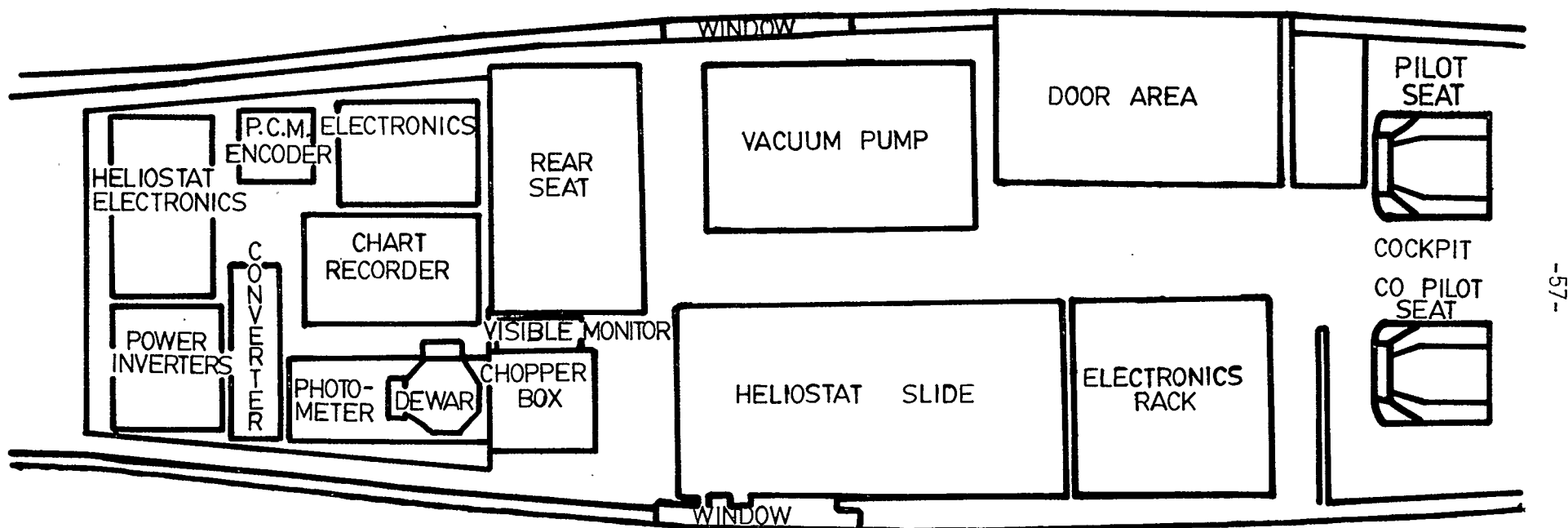


Fig. 3.7 Layout of equipment in Lear Jet cabin.

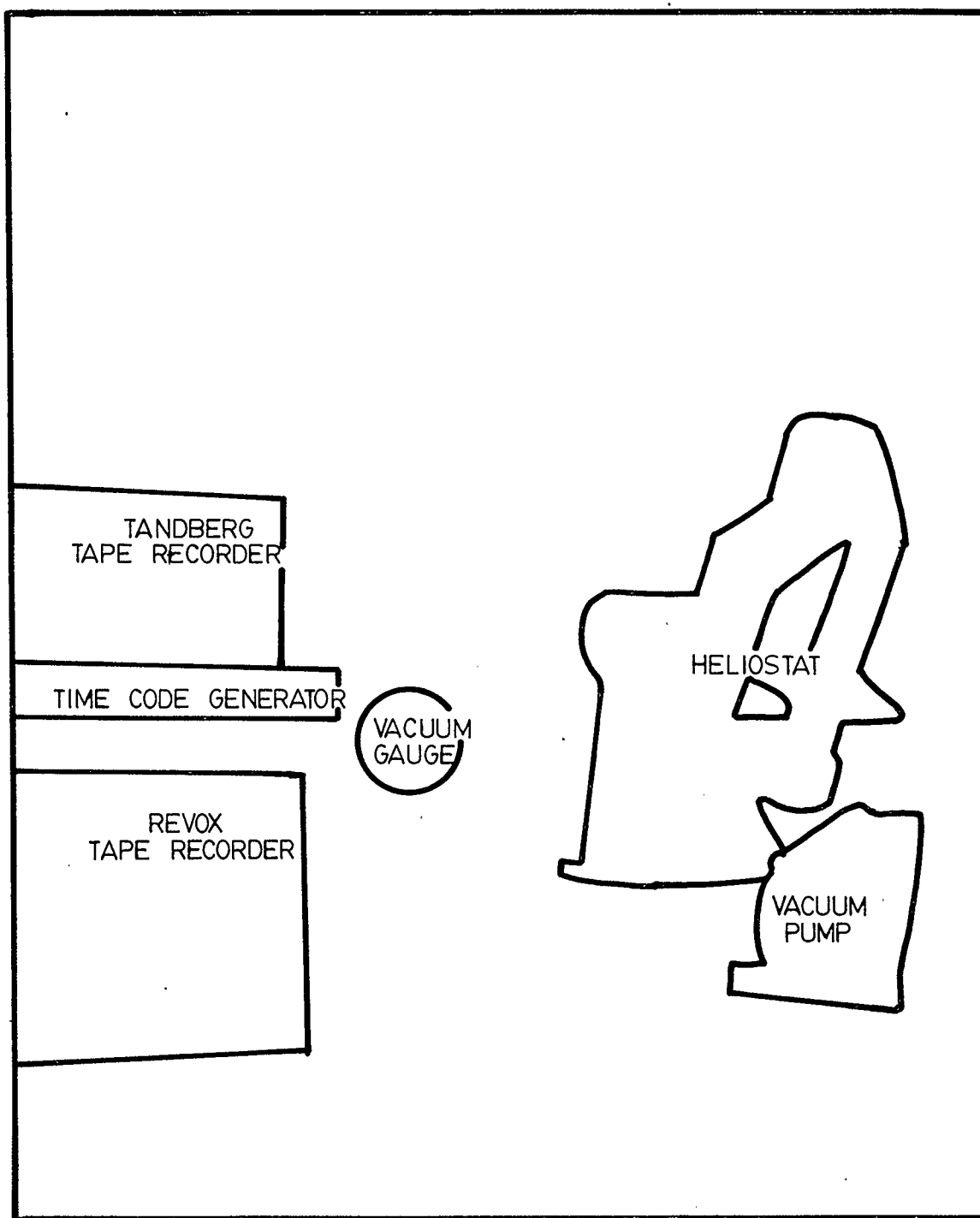
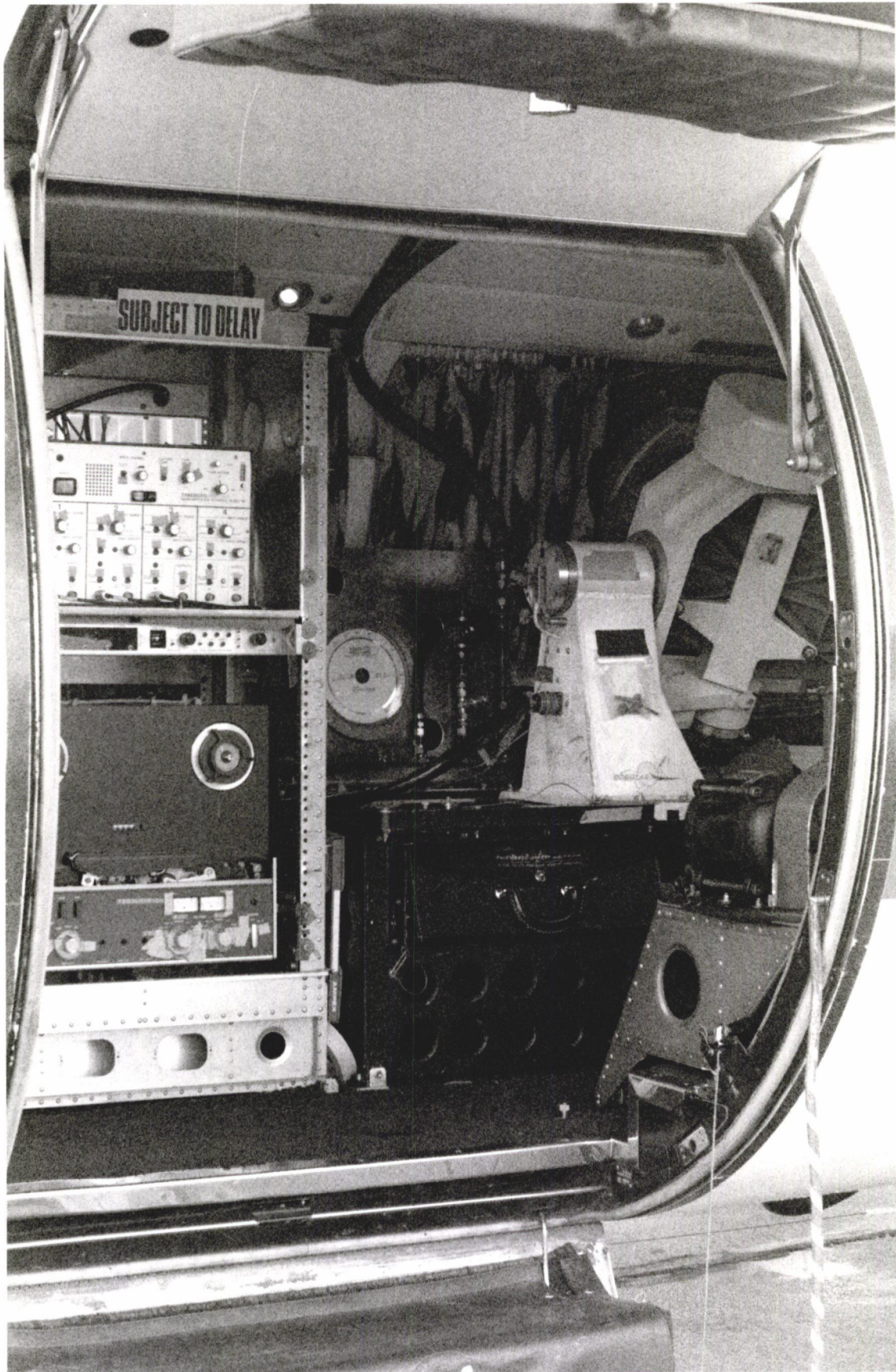


Fig. 3.8(overleaf). View through the door of the Lear Jet, showing electronics rack and heliostat (see key, above).



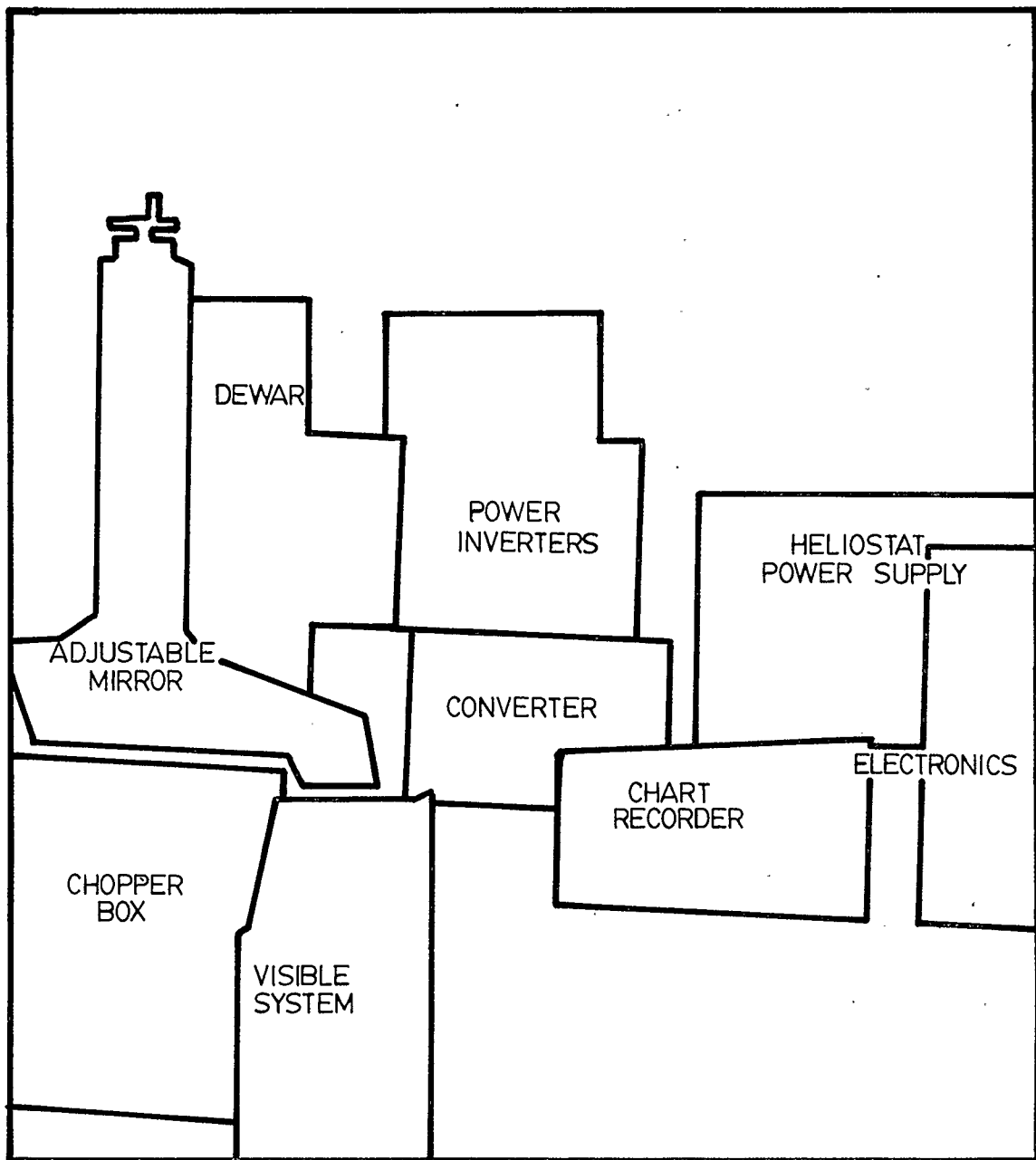
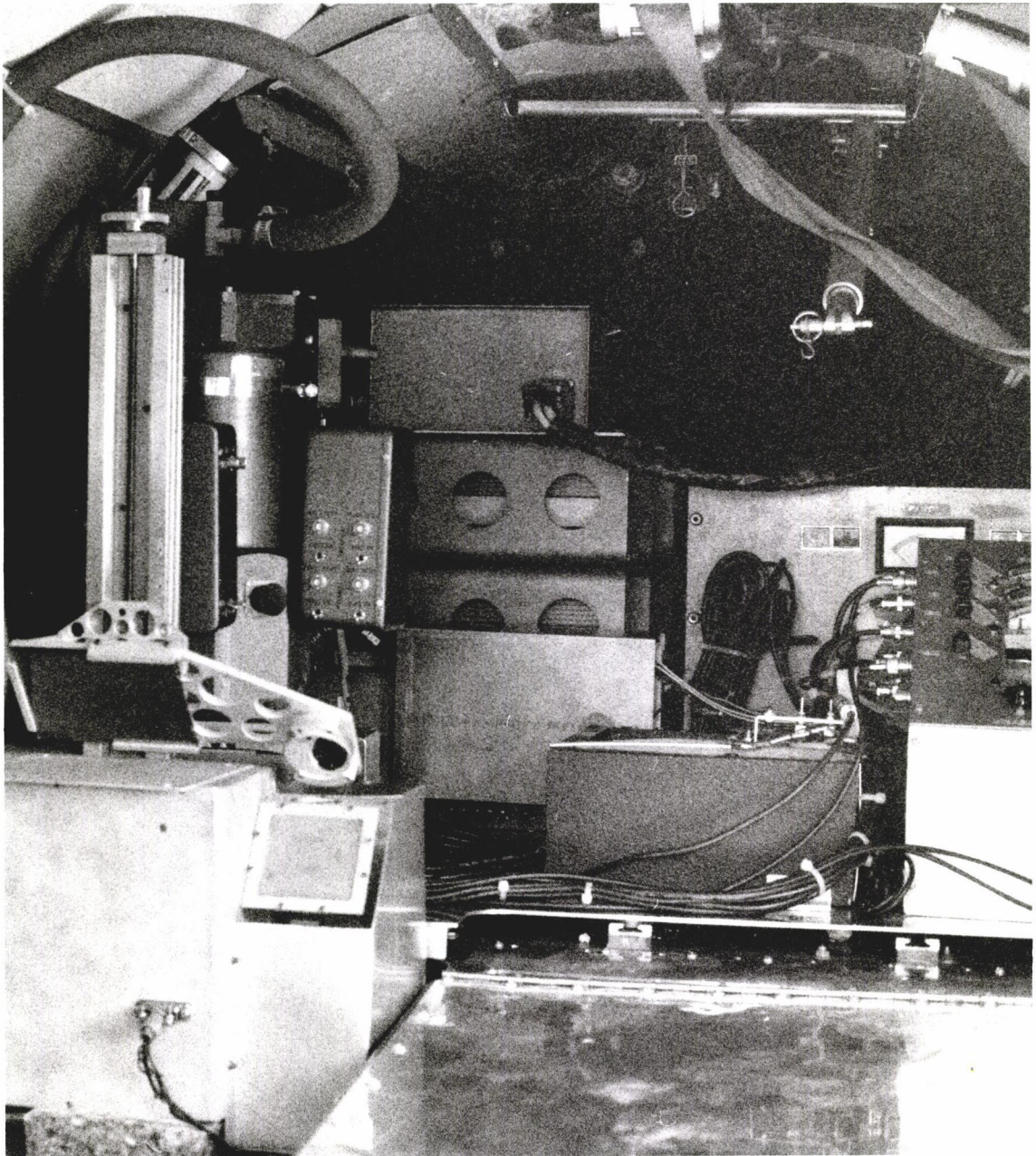


Fig. 3.9(overleaf). Photograph of the equipment in the baggage compartment of the Lear Jet, in flight configuration (see key, above).



proved invaluable as a log of the flight since times and comments were written on the chart alongside the real-time record.

The equipment was installed in the aircraft along with the special windows and power inverters during the ten-day period following Feb. 9 when the aircraft became available. The safe installation and subsequent inspections of every part of the equipment occupied considerable time. Nevertheless, two flight tests were made, on Feb. 20 and Feb. 21, over California and Nevada to test the heliostat, tracking, select electronic gain values, adjust optical alignment between infrared and visual optical systems, and fully test the data recording system in flight.

3.8 Test Flight Performance

The first test flight proved somewhat less than successful, since the heliostat gyro-guidance system did not function satisfactorily and was later found to have the gyroscope head oriented approximately 45° to its correct alignment. Nevertheless, the instrument functioned satisfactorily, and a chopping frequency scan permitted the selection of an operating frequency at which the aircraft vibrations caused the least disturbance or interference with the detector signals. Signal levels were also measured on the sun by hand-controlling the heliostat, and on the basis of these tests, the filters in each channel were changed to permit more radiation to reach each detector. Heliostat positions were chosen to avoid vignetting of the infrared beam by the inset window as the plane flew a simulated eclipse flight pattern planned beforehand in conjunction with NASA navigators.

The second test flight was completely successful and provided 45 minutes of heliostat operating experience and a further test of signal and noise levels under actual flight conditions.

A complete eclipse flight test was carried out several days before the eclipse, on Feb. 23 to ensure that all the necessary arrangements at the staging airfield at Minot Air Force Base, USAF were satisfactory. It was necessary that the aircraft be refuelled during this stop, and power was required while on the ground to allow pumping on the liquid helium surface before flight. This lead time for pumping was necessary to ensure that the detector reached its operating temperature below the lambda point before the eclipse track began. A portable heater also maintained the aircraft and the instrumentation at a reasonable temperature during this period. The organizational plan was found to be acceptable, leaving adequate time after departure from Moffett Field, California at 2:30 A.M. for a meteorological briefing by military personnel at Minot AFB. This flight also provided a test of the navigational track which had been designed to provide the necessary eclipse coverage at an altitude of 13.1 km within the limits discussed earlier. On this flight, a power inverter briefly filled the aircraft cabin with smoke before switching out of circuit automatically, but the built-in redundancy in the power system permitted the instrument to work satisfactorily during the entire flight.

Fig. 3.10 shows the aircraft at Minot AFB prior to the eclipse flight, on Feb. 26. The timing determined from the test flight described above was followed during the ferry flight and refuelling stop at Minot, and required only slight alteration for the final section into the eclipse shadow, to allow for different prevailing winds at the ceiling altitude.

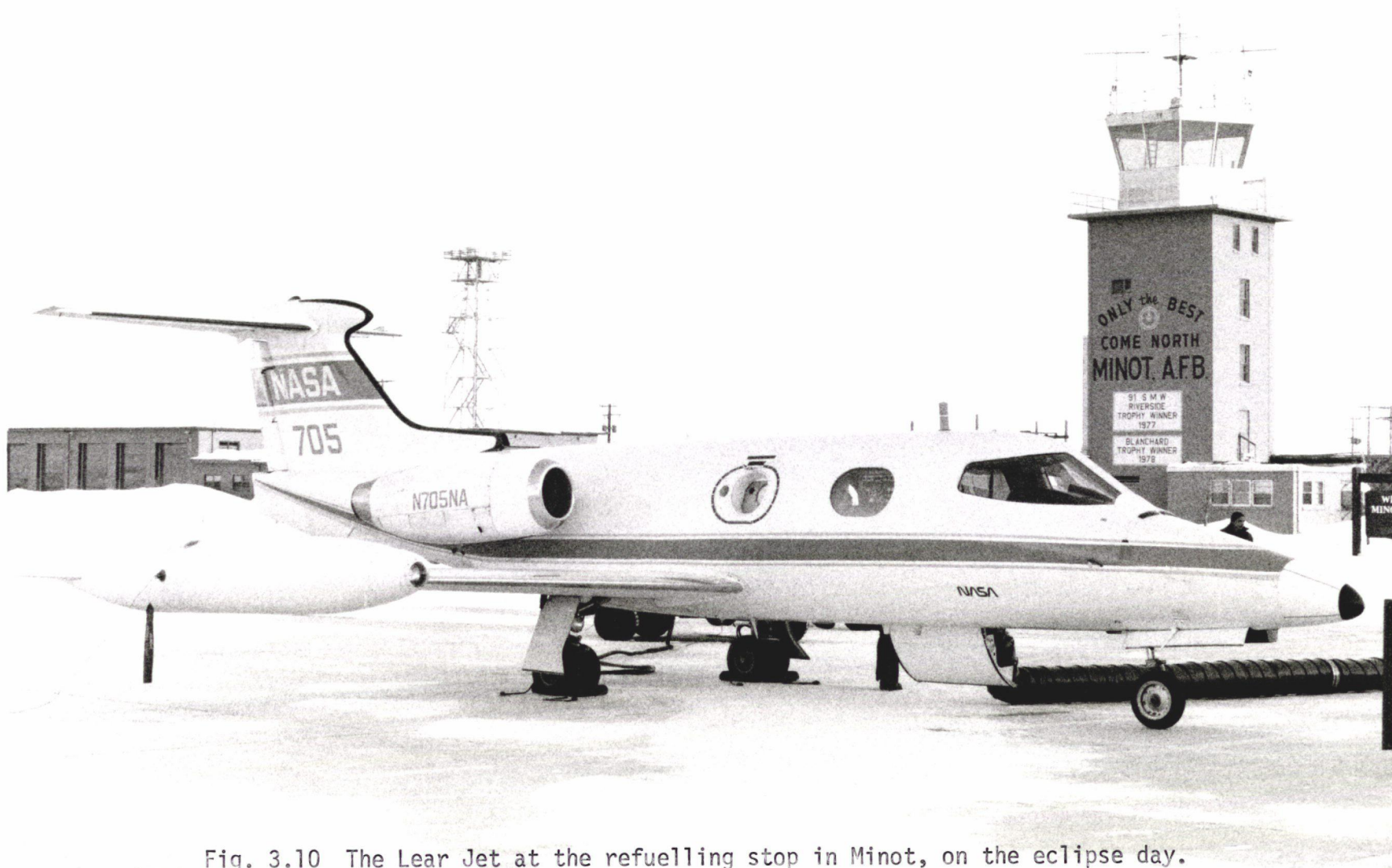


Fig. 3.10 The Lear Jet at the refuelling stop in Minot, on the eclipse day.

CHAPTER 4

ECLIPSE TIMING AND GENERATION OF THEORETICAL ECLIPSE CURVES

4.1 Introduction

Determination of the best representation of the intensity distribution across the solar disc from the measured eclipse curve can be obtained in general in two complementary ways. The first method requires a deconvolution which can be shown in practice to be very sensitive to noise in the data. The alternative method is the comparison of the eclipse data with theoretical curves generated for various intensity distributions, including those derived from model atmospheres. In both cases, the curves must be matched with the actual eclipse in terms of apparent angular sizes of sun and moon, and angular speed of moon relative to sun. Also, a knowledge of position angle of contact on the solar disc is desirable to evaluate possible contributions from active regions.

4.2 Eclipse Geometry

Conventionally, eclipse geometry is calculated by projecting motions of the sun and moon onto the fundamental plane, which is a plane passing through the centre of the earth, with its normal parallel to a line joining the centres of the sun and moon. Eight parameters, called the Besselian elements, are of importance in the description of the eclipse. These are:

- 1,2. x, y the coordinates of the centre of the lunar shadow on the fundamental plane;

3. d the declination of the z-axis of the fundamental plane (defined to be parallel to a line joining solar and lunar centres, passing through the centre of the earth);

4. μ the hour angle of the z-axis, referred to Greenwich;

5,6. f_1, f_2 the half-angles of the penumbral and umbral cones, respectively;

and 7,8. l_1, l_2 the radii of the circles in which the penumbral and umbral cones intersect the fundamental plane.

These quantities (or functions of them), as well as their time derivatives where appropriate, are tabulated for every eclipse (see for example the American Ephemeris and Nautical Almanac, 1979). The location and motion of the observer with respect to the fundamental axes are obtained from spherical geometry, and are described by the coordinates (ξ, η, ζ) and their time derivatives. The relevant transformation equations, modified to include change of geographical location such as would occur in an aircraft, are (after Smart, Ch. 15, 1971):

$$\xi = \rho \cos(\phi') \sin(\mu - \lambda)$$

$$\eta = \rho \sin(\phi') \cos(d) - \rho \cos(\phi') \sin(d) \cos(\mu - \lambda)$$

$$\zeta = \rho \sin(\phi') \sin(d) + \rho \cos(\phi') \cos(d) \cos(\mu - \lambda)$$

$$\xi' = (\rho \cos(\phi'))' \sin(\mu - \lambda) + \rho \cos(\phi') \cos(\mu - \lambda) (\mu' - \lambda')$$

$$\eta' = (\rho \sin(\phi'))' \cos(d) - d' \zeta - (\rho \cos(\phi'))' \sin(d) \cos(\mu - \lambda) + \sin(d) (\mu' - \lambda') \xi$$

$$\zeta' = (\rho \sin(\phi'))' \sin(d) + (\rho \cos(\phi'))' \cos(d) \cos(\mu - \lambda) + d' \eta - \rho \cos(\phi') \cos(d) \sin(\mu - \lambda) (\mu' - \lambda')$$

where ρ and ϕ' are geocentric distance and latitude of the observer, λ is longitude, and primes denote time derivatives. The foregoing relations are basic to all calculations of eclipse geometry and timing at any location or altitude on the earth.

4.3 Determination of Actual Flight Path

It is obviously important to know the path flown by the aircraft through the eclipse shadow before the transformations to fundamental coordinates can be made. This proved somewhat more difficult to determine than was expected from preflight planning since no automatic recording of navigational data was carried out on the small Lear Jet aircraft. The pilots were provided with a navigational track which had been generated beforehand in consultation with NASA Ames Research Center, Airborne Science Office navigators for zero wind conditions at the flight altitude. This path was modified to account for the prevailing wind at the assigned altitude on the morning of the eclipse day after the final meteorological briefing at Minot AFB. Thereafter the pilots followed the track, utilizing radio beacon (DME) equipment with which the aircraft was equipped. This equipment allowed the pilots to verify the aircraft position along the track by measurements of range and bearing from several nearby radio beacons. Post-flight interpretation of this data was confused initially by an apparent ambiguity between end-point position and time (16:58 UT) recorded on the navigational track by the pilot, and the actual time when the totality track was terminated (16:56:30 UT) according to the inflight voice recording. However, it was later determined that the 16:58 UT time and position

corresponded to an accurately predicted point on the track, and that a trajectory based on this end-point and upon the pilot's recorded track on the map provided information of the necessary precision to be confident of the finally derived aircraft motion. The flight path was generated by assuming the given endpoint and time to be an extrapolation of the actual path, and by incorporating the designed azimuth angle to the sun of 102° , a wind of 60 knots at 270° (obtained from Minot AFB meteorologist prior to the flight), and an airspeed of 425 knots to calculate ground speed and direction of the aircraft at five minute intervals. This derived track was found to begin very close to the 16:27 UT start point given by the pilot, and coincided exactly with the edge of the lunar shadow at 16:39:11 UT. This time of second contact agrees to within a second with that obtained from visual evidence recorded on inflight records, and from the optical data (see 4.4), and thus provided final justification for the adopted procedure of track determination.

4.4 Contact Timing

Once the geographical location of the observer and its variation with time have been determined, the transformed coordinates ξ, η, ζ and their derivatives can be calculated at any instant. The time of second or third contact can then be determined by equating the distance between the observer and the centre of the lunar shadow with the radius of the umbra on the observer plane (parallel to the fundamental plane, but passing through the observer). In general, this is done by assuming a time of contact, obtaining the Besselian elements and observer coordinates for this time, and then finding a correction t to the assumed time

for which the contact relationship holds. To a first approximation:

$$(x-\xi + (x'-\xi')t)^2 + (y-\eta + (y'-\eta')t)^2 = (l_2 - \zeta \tan(f_2))^2$$

where the sign convention that l_2 is negative for totality is used, and variations in l_2 and in $\zeta \tan(f_2)$, f_2 being a small angle, have been neglected. If necessary, further iterations can be performed until the desired accuracy in timing has been attained.

In practice, it was found simpler to obtain time of second contact geometrically, by finding the intersection of the edge of the lunar shadow projected onto the earth at the altitude of the aircraft with the aircraft position, as is shown in Fig. 4.1. In principle, this method is exactly equivalent to that outlined above. The resulting time of second contact was found to be 16:39:11 UT.

Independent evidence for time of second contact was obtained from the in-flight voice recording, on which the moment of disappearance of the photosphere on the auxiliary steering image was noted. The time of second contact could also be obtained quite accurately from the visible signal. These independently derived values were in very close agreement, thus supporting the method of flight path determination. Time of third contact was obtained in a similar manner, without the aid of the auxiliary visible signal because solar reacquisition was not possible until significantly later. The time of this event thus depends to a somewhat greater extent upon the assumed navigational track. Time of third contact was found to be 16:43:10 UT, giving a net duration of totality of 3^m59^s, with an estimated error ± 3 seconds.

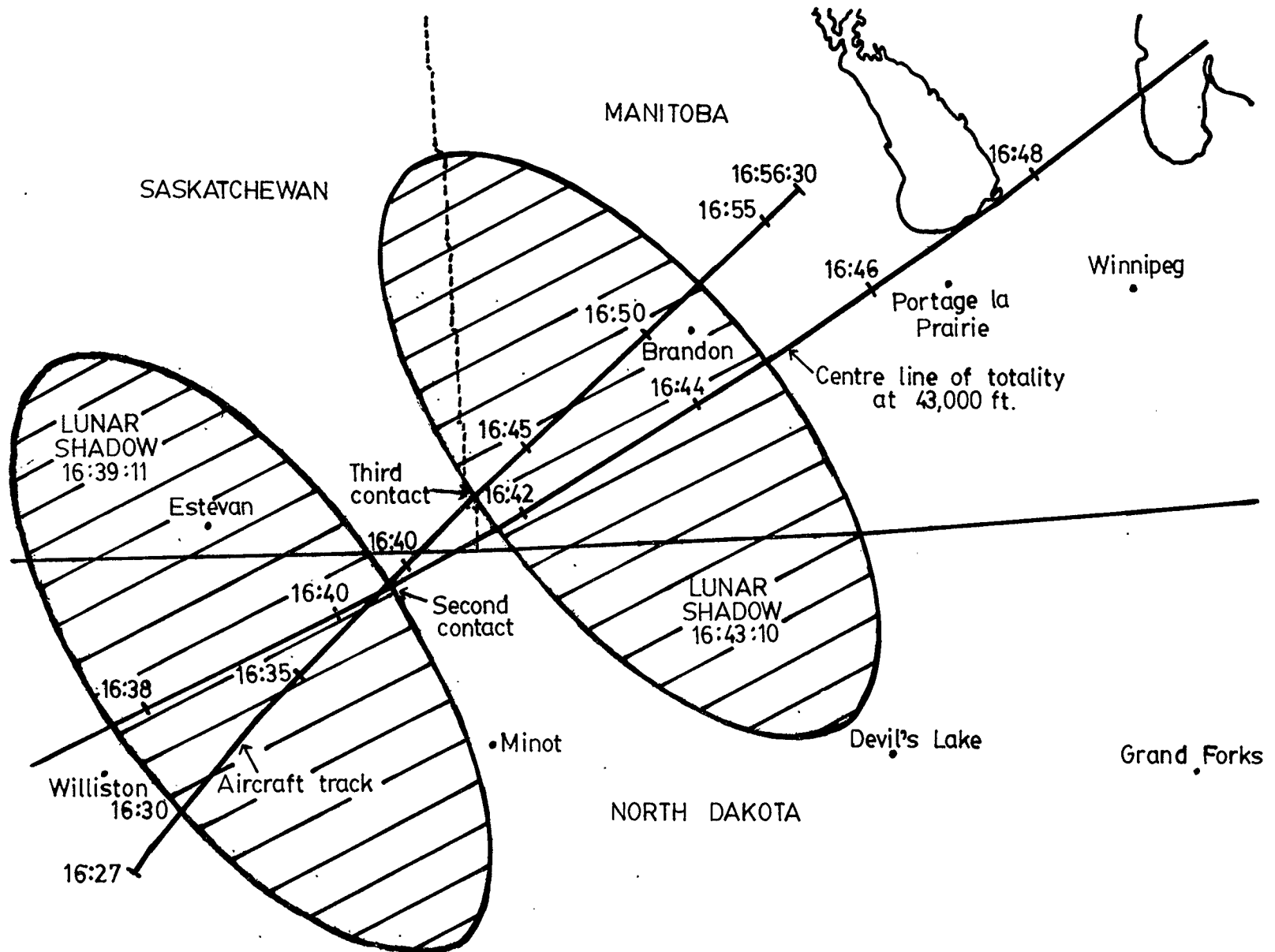


Fig. 4.1 Aircraft flight path during eclipse run.

4.5 Angular Eclipse Speed

The apparent angular speed of the moon relative to the sun, and the angular sizes of moon and sun during the eclipse, must be known in order to generate an artificial eclipse curve suitable for comparison with the observed one. This can be obtained from consideration of the relevant relationships on the observer plane. The observer coordinates and their derivatives can be calculated for a time for which angular speed is required, to give a net speed n of the centre of the lunar shadow relative to the observer:

$$n^2 = (x' - \xi')^2 + (y' - \eta')^2$$

This linear speed can then be translated into apparent angular speed at the moon's distance from the aircraft. This method is very sensitive to small changes in geographical location or timing, and several significant figures must be retained in the calculations, since the final result depends basically upon differences of small quantities.

The distance from the moon or sun to the aircraft was calculated for the location and altitude of the aircraft, including effects arising from the curvature of the earth, and the airplane's position relative to the sub-solar (or lunar) point. These values, in conjunction with ephemeris values of centre separation of earth and sun or earth and moon and angular semidiameters of both bodies from the earth's centre, were used in subsequent calculations of lunar and solar apparent angular diameters, and in the translation from linear to angular speed.

A more straightforward method of arriving at apparent angular speed is to use the times of second and third contacts to derive an average speed during totality, when the moon moves a distance equal to

the difference between lunar and solar diameters, relative to the sun. This method depends implicitly upon a central crossing, which was essentially the case for the aircraft track followed, and a linear one, which; due to the curved natures of both the eclipse and aircraft tracks, is not strictly the case. Additional assumptions include uniform angular speed and constant apparent sizes of the sun and moon over totality. Although not rigorously valid, these latter are very good approximations over the short time span (under 4 minutes) involved. The major source of error in this calculation is believed to be the error in timing of the third contact.

In view of the remaining uncertainties in both calculations, a mean value for the angular speed of the moon relative to the sun of $0.310^{\circ}/s$ was adopted, with an uncertainty of $\pm 1\%$.

4.6 Contact Position Angle Determination and Location of Active Regions

Had it been possible to measure the entire eclipse curve from first to fourth contact, it would have been necessary to obtain values of the position angle of the centre of the lunar shadow as a function of time in order to trace out the apparent path of the moon across the solar disc. However, this was unnecessary for the present experiment because of the limited observational time, and therefore the assumption was made that the centre of the moon's shadow passed through the centre of the sun (as seen from the earth) at a constant angular speed in a straight line. In this case, knowledge of position angle at a particular contact is used only to provide information about the locations of active regions relative to the lunar limb in order to evaluate possible contributions from these to the overall signal. The choice of the fundamental

axes made previously (x-axis directed eastward, y-axis northward) makes the calculation of the position angle P very simple in these coordinates:

$$P = \tan^{-1} \left(\frac{x-\xi}{y-\eta} \right)$$

with the quadrant of P chosen such that the sign of $\sin P$ is opposite to that of $x-\xi$ for second and third contacts. In practice, if the coordinates have not been determined for the precise time of the relevant contact, it becomes necessary to arrive at a value of position angle in a modified way as outlined in detail in Ch. 9 of the Explanatory Supplement to the Astronomical Ephemeris and American Ephemeris and Nautical Almanac (1961).

Locations of active regions on the solar disc were obtained from photographs taken by University of Calgary personnel at a ground site near Oxbow, Saskatchewan and by a NASA - Ames Research Center engineer with University of Calgary equipment at Minot, North Dakota. Active features visible on the solar disc permitted the alignment of successive photographs, and thus the direction of motion of the moon relative to the sun and the eventual contact point could be established with reference to solar features for both locations. Calculation of the predicted position angle of contact then fixed the north point of the solar disc and from that reference, the location of second contact as seen from the aircraft was established. These locations could be related to solar coordinates from the known position angle of the solar rotation axis of -20.8° (American Ephemeris and Nautical Almanac, 1979). Fig. 4.2 shows the motion of the moon across the solar disc as seen from the aircraft as well as some of the more prominent active features on

the sun at the time of eclipse. This figure can be compared to the photograph of totality shown in Fig. 4.3.

The sun at this phase in its 11 year cycle, close to maximum activity, was relatively active on the day of the eclipse, with several prominent features both on the visible hemisphere and at the limb. It is useful to briefly summarize the activity on the overall solar disc, although the portion of the sun actually visible but subsequently covered by the moon during the useful time of the present experiment was very small. This point is illustrated in Fig. 4.2, and a summary of the activity on the sun taken from Solar-Geophysical Data prompt reports, April 1979, is shown in Fig. 4.4.

There were three major sunspot groups surrounded by other manifestations of centres of activity (CA) designated by McMath Region numbers. Calcium plage regions existed across the whole sun, but those which contained significant sunspots were designated McMath 15840, near the northern pole, 15838 around two sunspot groups to the west of the central meridian, and 15850 near the eastern limb of the sun. Long dark filaments were associated with most of these active regions, and extensions of several of these appeared as quiescent prominences at the solar limb.

The region 15850 close to the eastern limb was the only one still visible during the second contact eclipse run, and the moon's edge passed in front of the sunspot group at the beginning of the data run at about 16:33:30 UT. Weak quiescent prominences from a neighbouring region 15859 appeared to reach out to the solar limb close to the point of second contact as seen from the aircraft (compare figures 4.2 and 4.4). Other prominences, apparently quiescent, are also seen on the limb during

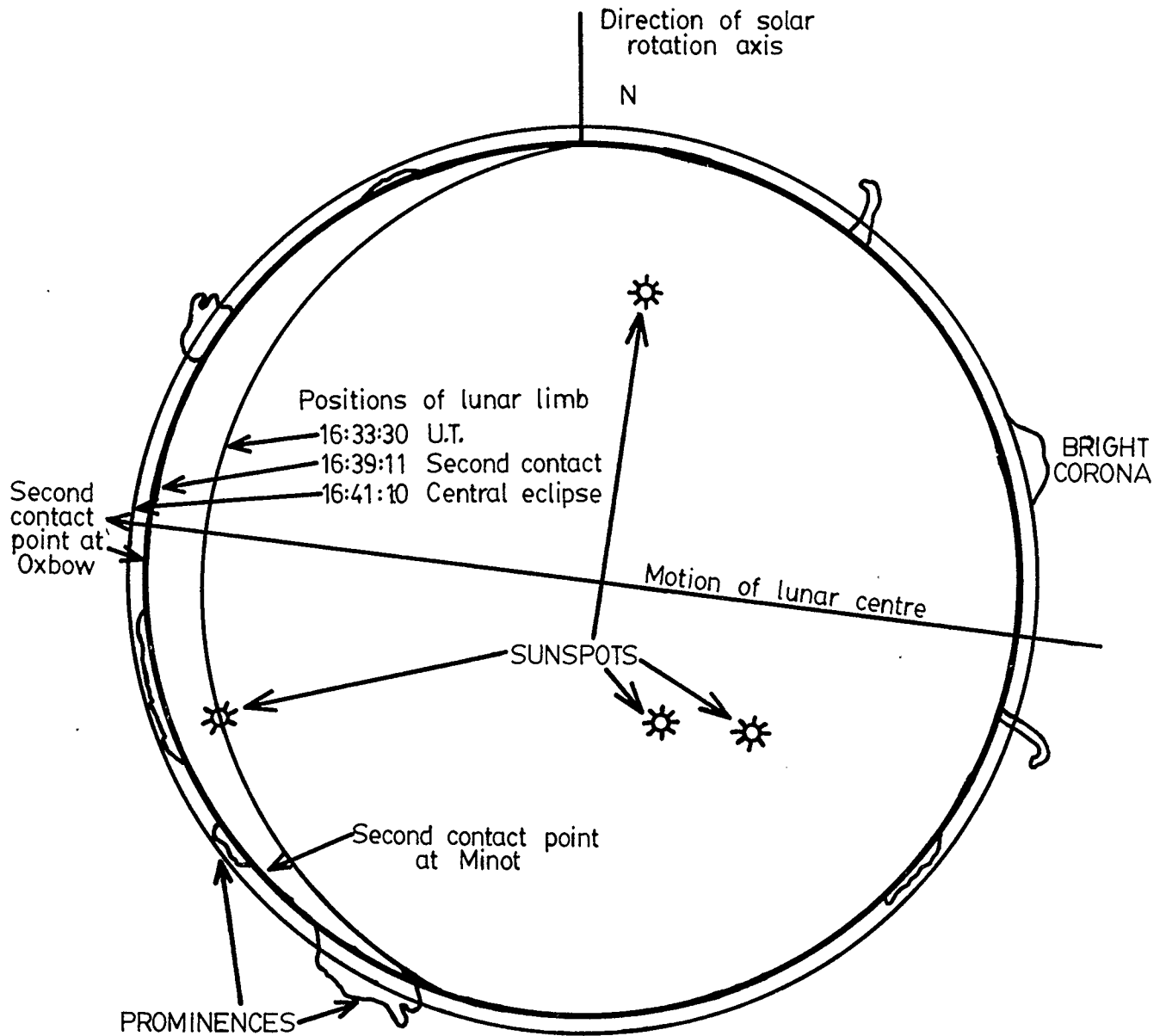
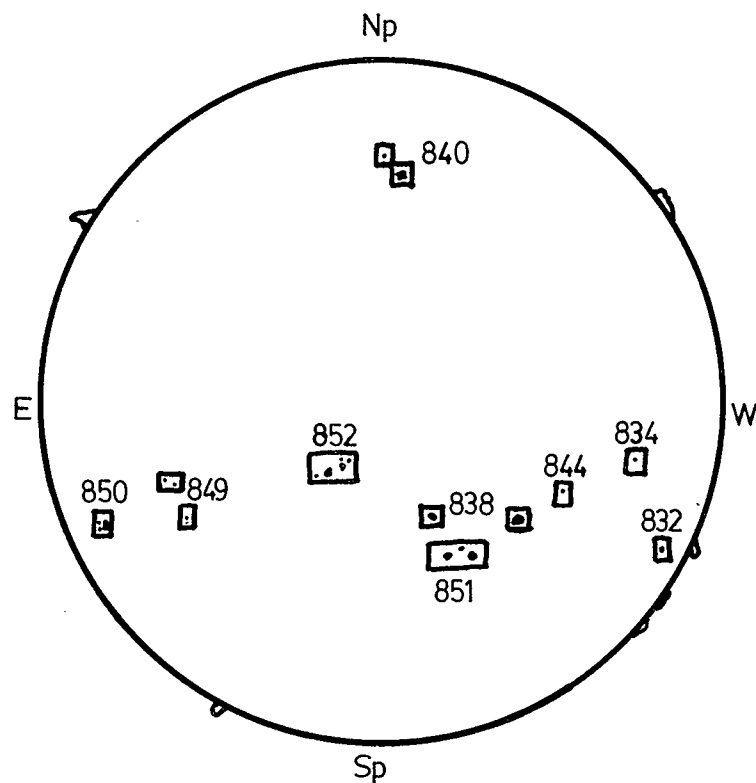


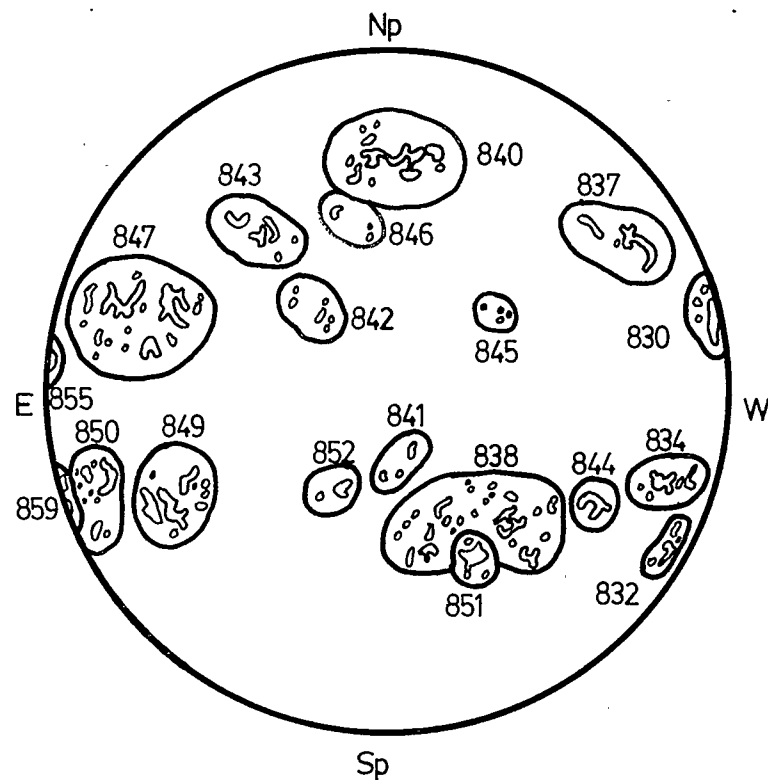
Fig. 4.2 Apparent motion of lunar limb relative to solar active features as seen from the aircraft.



Fig. 4.3 The eclipsed sun as seen from Oxbow, showing location of active features visible after second contact.



BOULDER SUNSPOTS 1437 U.T.
PROMINENCES 2016 U.T.



McMATH-HULBERT CALCIUM
REPORT
1520 U.T.

Fig. 4.4 Solar active regions, seen on the sun on Feb. 26 1979, showing sunspots, calcium plage regions, and $H\alpha$ features (overleaf). (Taken from Solar-Geophysical Data, 414 Part 1, April 1979.)

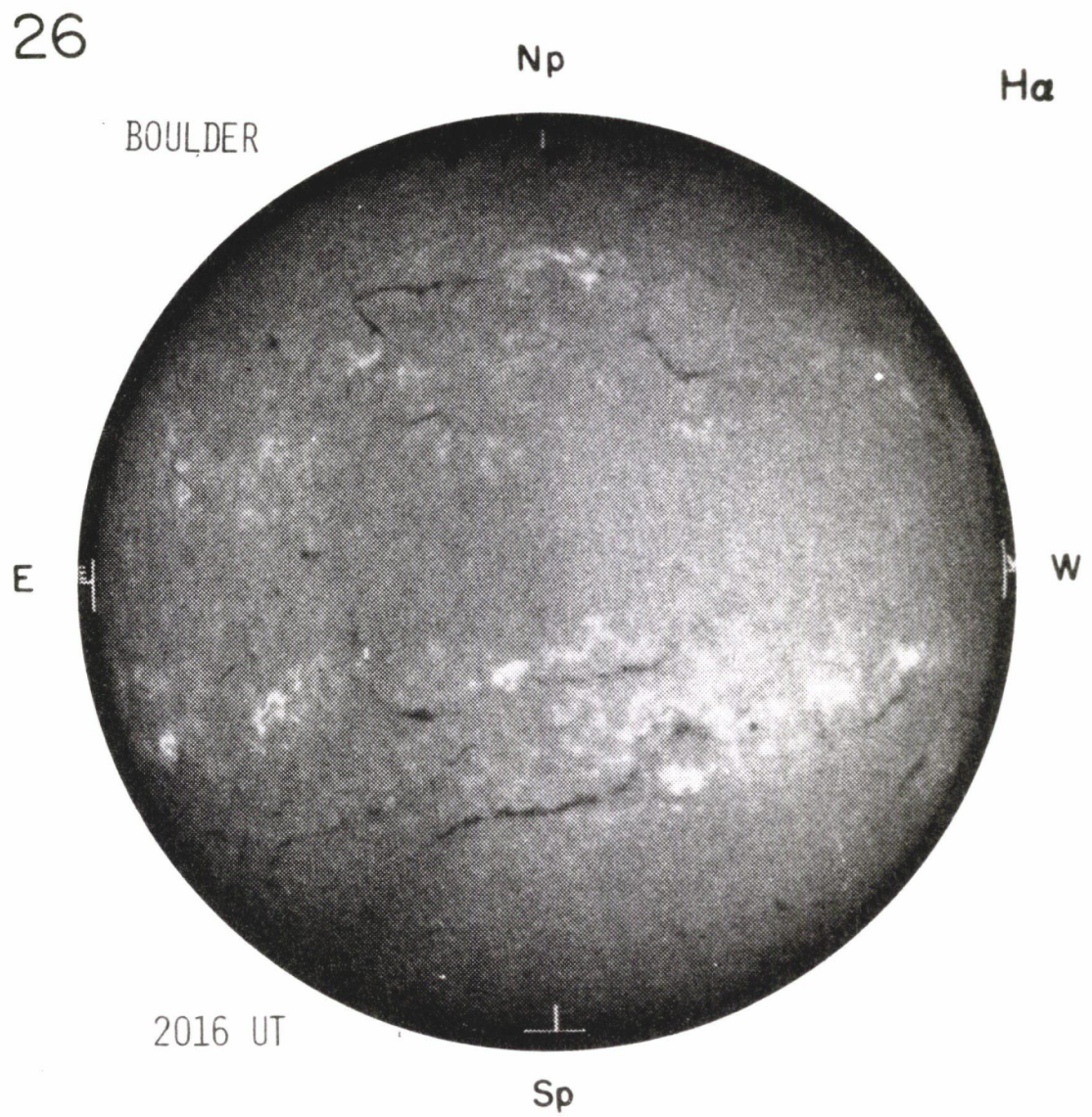


Fig. 4.4 (continued).

second contact.

Flare activity during the period of the present eclipse observations was confined to an Sn flare in region 15851 which reached maximum phase at 16:39 UT, but the sun was almost fully hidden by the moon at this time, and the flare had subsided before fourth contact occurred. Other small flares occurred in regions already covered by the moon during the time data was obtained, and thus should have no effect on the data. No radio outbursts were reported during the relevant time interval and X-ray levels, while building slowly, showed no flare at this time.

Thus the narrow strip remaining visible on the eastern limb during the data run, while containing one sunspot group and several calcium plage regions and filaments, did not contain any flare or related time changes during the eclipse run.

4.7 Theoretical Eclipse Curves from Models

Although deconvolution appears to be the most straightforward way to obtain an intensity distribution from the eclipse curve, it is inherently dependent upon differentiation, and thus the results may be highly oscillatory, especially in the presence of noise. Modifications incorporating constraints such as smoothness of the intensity distribution have been utilized successfully by others to suppress such oscillations (see Smith, 1975 for one such technique applied to a radio wavelength eclipse measurement). In the present experiment a simple deconvolution was attempted, but the solution was extremely noisy and oscillatory and consequently difficult to interpret, as perhaps could

be anticipated from the amount of noise present in the data. Therefore, it was decided not to pursue this technique, but rather to generate eclipse curves for various intensity distributions across the sun for comparison with the data obtained. The fundamental equation describing an eclipse curve can be written as follows:

$$S(r_c) = k \int_{r=0}^{r_s} \int_{\theta=0}^{2\pi} I_s(r, \theta) f(r, r_c, \theta) r dr d\theta \\ + k \int_{r=0}^{r_m} \int_{\theta=0}^{2\pi} I_m(r, \theta) f'(r, r_c, \theta) r dr d\theta$$

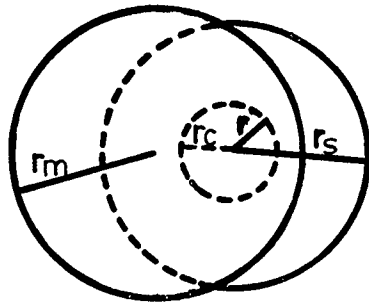
where r_c is the separation of centres of the sun and moon; r_s and r_m are radii of the sun and moon, respectively; S is the measured signal; k is a constant incorporating factors such as filter transmissions, amplifier gains and detector responsivity; I_s and I_m are intensity at any radius and angle on the solar and lunar discs; and f and f' are weighting functions which include variation of instrument function over the disc and, in the first integral, the effect of the moon in blocking part of the solar radiation. Radiation from the filters, aircraft window, atmosphere, and instrument is present in both positions of the chopping system and is cancelled from the final signal by the phase-sensitive detection system. The above relation is simplified in the present case by the assumption that only radial variations of intensity exist, and that the instrument response function is constant over a field of view appreciably larger than the solar disc, as was designed. Then the integration becomes one-dimensional, and the normalized signal is given by:

$$\frac{S(r_c)}{S_0} = \frac{\int_{r=0}^{r_s} I_s(r) r \theta_a(r, r_c) dr + \pi r_m^2 \bar{I}_m}{\int_{r=0}^{r_s} I_s(r) 2\pi r dr + \pi r_m^2 \bar{I}_m}$$

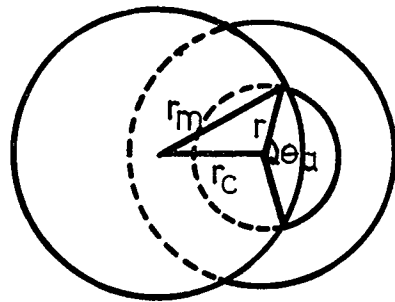
where S_0 is intensity from the sun-moon system outside eclipse, the weighting function has been replaced by θ_a , the arc length in radians of the uneclipsed sun at a radius r for separation of solar and lunar centres of r_c , and $\overline{I_m}$ is the mean lunar intensity. This curve can then be related to time by the angular speed w_e of the eclipse; i.e., $S(r_c) = S(w_e t)$, where t is measured from time of central eclipse. The arc length θ_a can be calculated from the geometry of the intersection of two circles of radii r_m and r_s , and is given for various cases by the following relationships (see Fig. 4.5):

1. $r_c \leq r_m$ and $r \leq r_m - r_c$ $\theta_a = 0$
2. $r_c \leq r_m$ and $r > r_m - r_c$ $\theta_a = 2\pi - 2\cos^{-1}\left(\frac{r_c^2 + r^2 - r_m^2}{2rr_c}\right)$
3. $r_c > r_m$ and $r \leq r_c - r_m$ $\theta_a = 2\pi$
4. $r_c > r_m$ and $r > r_c - r_m$ $\theta_a = 2\pi - 2\cos^{-1}\left(\frac{r_c^2 + r^2 - r_m^2}{2rr_c}\right)$.

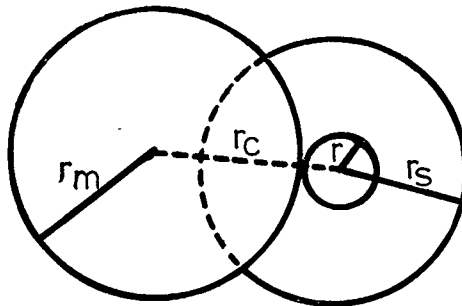
In the computational algorithm, the integral was replaced by a summation over narrow annuli, each of width 0.1° , and was performed for central separations incremented by 1° . Thus the sun was represented by slightly more than 9700 annular rings of different intensities, and the entire eclipse curve from first contact to central eclipse was defined by approximately 1980 points, although only a small portion of the eclipse curve corresponding to the range of centre separations for which data was obtained was in fact calculated. The fine grid for each centre separation was found to be necessary in order to obtain sufficient accuracy in the calculated curve. Accuracy was checked by comparison of the computed eclipse curve for a flat intensity distribution ($I(r) \equiv I$) with



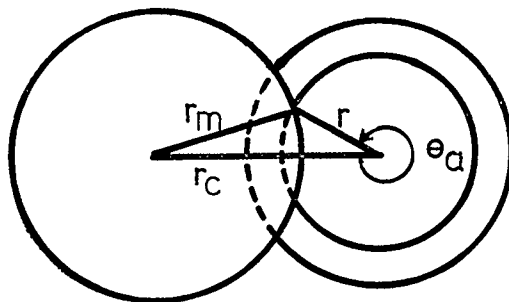
1. $r_c \leq r_m, r \leq r_m - r_c$



2. $r_c \leq r_m, r > r_m - r_c$



3. $r_c \geq r_m, r \leq r_c - r_m$



4. $r_c \geq r_m, r > r_c - r_m$

Fig. 4.5 Arc length of an exposed annulus, for various cases.

exact geometric calculations of the exposed area from the intersection of two circles with differing radii r_m and r_s (Hagen and Swanson, 1975).

Basically three intensity distributions were used to generate eclipse curves for comparison with the measured data. The first is the flat distribution, since most measurements in the wavelength region of interest show very little limb darkening or brightening. The second is the intensity distribution predicted by the HSRA model (Gingerich et al, 1971) for a homogeneous sun with a temperature profile derived from continuum intensity measurements. Finally, an eclipse curve for a flat sun with a brightness spike approximating to that reported by Beckman et al (1975, 1976) was generated in view of the significance of this previous result and its interpretation in terms of inhomogeneities in the chromosphere. The three intensity distributions used in this derivation are shown in Fig. 4.6, and the resultant integral eclipse curves are shown in Fig. 4.7 for a limited part of the sun.

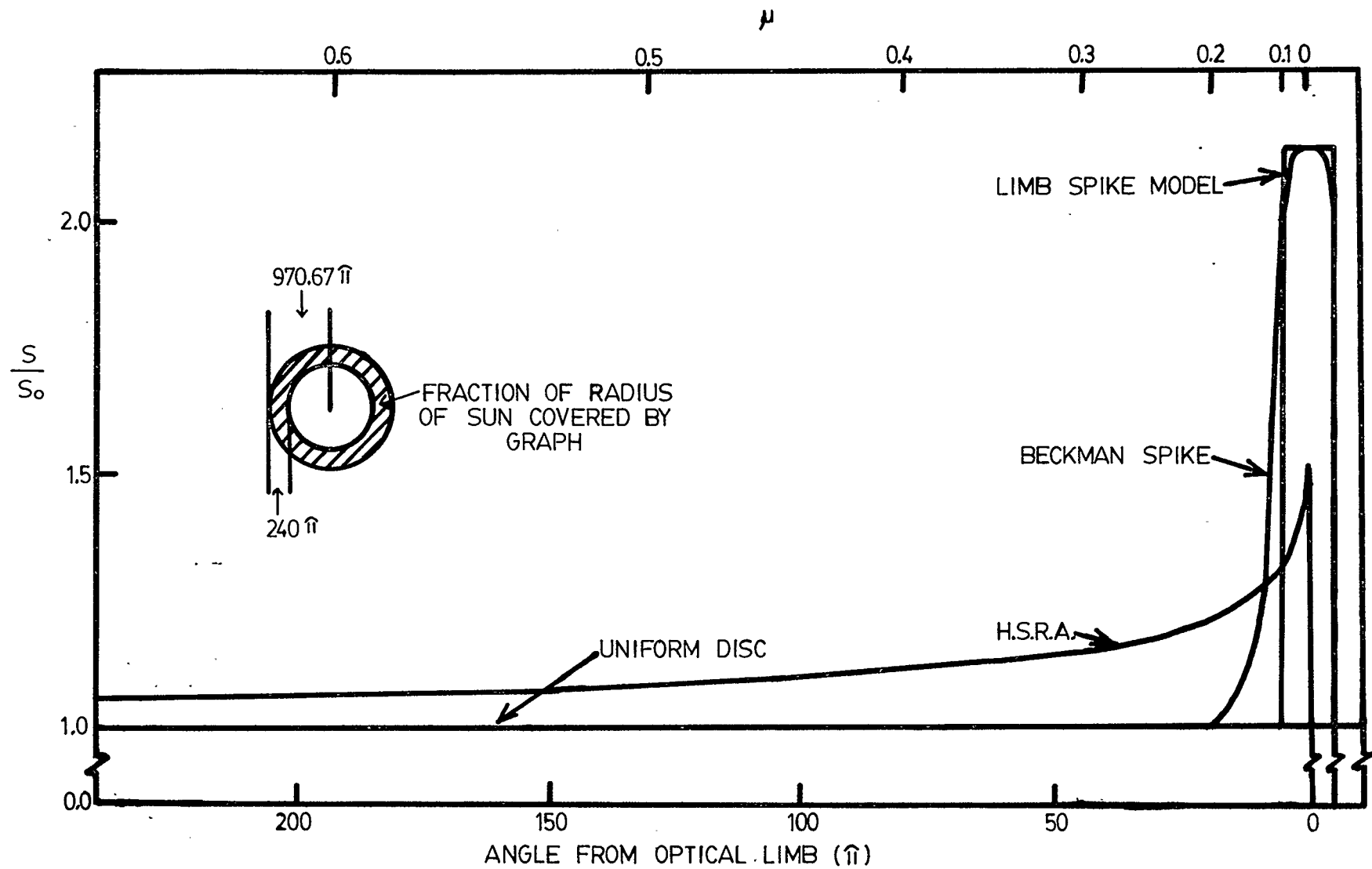


Fig. 4.6 Radial distribution of solar intensity for several models.

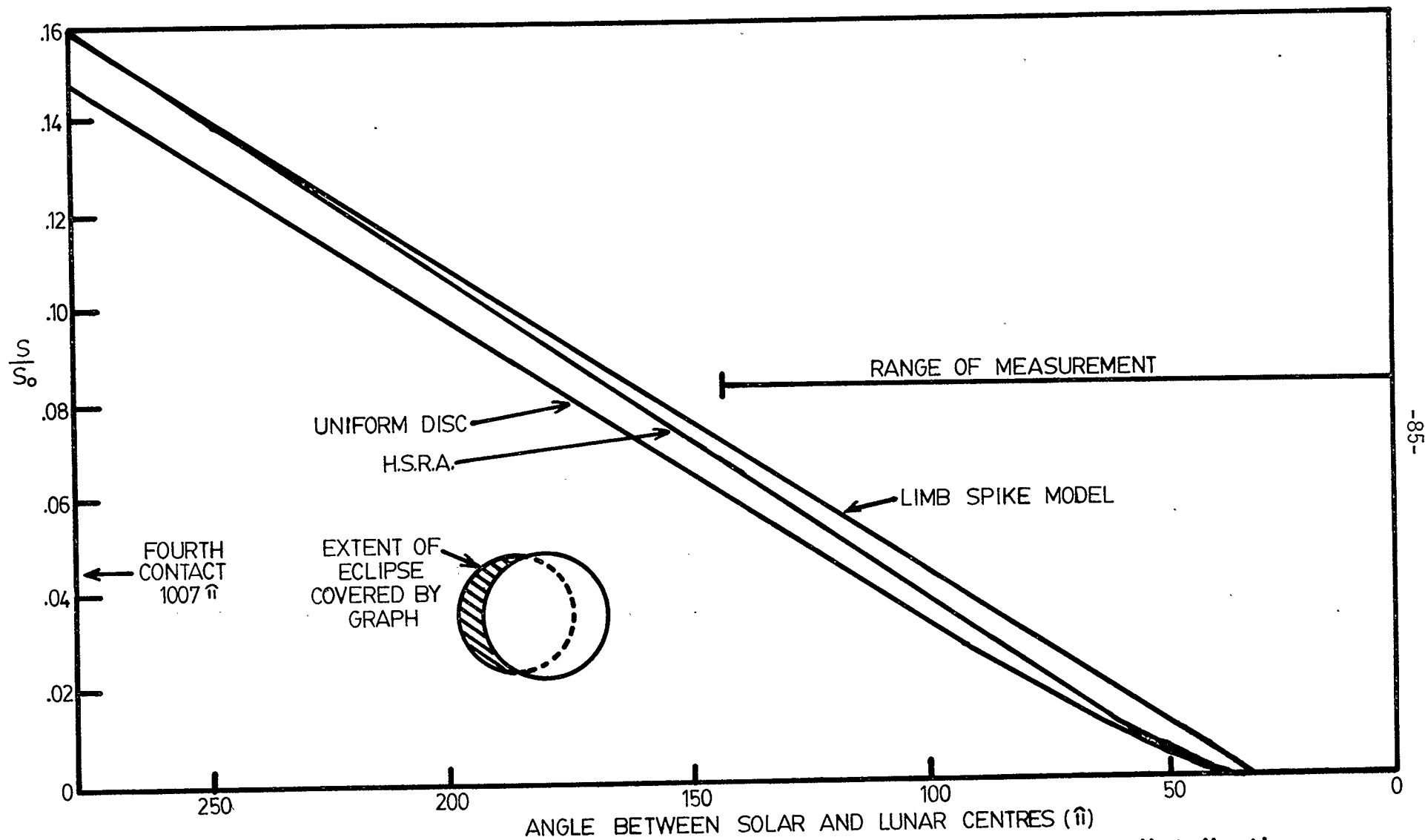


Fig. 4.7 Predicted eclipse curves for three solar intensity distributions of Fig. 4.6.

CHAPTER 5

INSTRUMENT PERFORMANCE, DATA ANALYSIS, AND CONCLUSIONS

5.1 Introduction

An eclipse experiment is, by its nature, very inflexible in that it can be performed only at a specified time over a small range of geographical locations, and it cannot be easily repeated in the event of equipment failure or other unforeseen events. By the same reasoning, a complete test duplicating all the important features expected during the data run cannot be carried out prior to the eclipse. Thus, the actual eclipse flight in a sense combines functions of final proving of the instrument design with the desired acquisition of data. The analysis of the data must be sufficiently flexible to allow the incorporation of effects arising from characteristics of the instrument which become apparent only during the final flight into the interpretation of the results. Thus the results of an eclipse experiment depend more heavily than most other experiments on knowledge of the detailed behaviour of the instrumentation, and uncertainties in the latter must inevitably be reflected by uncertainties in the interpretation of the physical significance of the data obtained.

5.2 Eclipse Flight Performance

Data were obtained from the time of solar acquisition after turning onto the designated eclipse interception track at 16:27 UT as described earlier, until the turnoff point after third contact at 16:56:30 UT. This portion of the flight pattern provided coverage of

the eclipse in terms of separation of solar and lunar centres from 4.4° before to 4.8° beyond central eclipse.

The early data, during initial solar acquisition by the heliostat, until about 16:33:30 UT, were very noisy, with major excursions of the data, related to aircraft motions and the consequent gyro-controlled mirror movements, and possibly to the change in pressure on the helium surface during the rather rapid pump-down made necessary by an inadvertent vacuum release during take-off. The data from this time until central eclipse time at the aircraft of 16:41:10 UT were found to be noisy but useable from only one of the four channels. Channels 2 and 4, sharing the same primary optics, produced no recognizable signals throughout the flight, after performing excellently during test flights, and it was discovered in post-flight calibration and alignment checks at NASA - Ames Research Center that the primary optics of these channels had become misaligned. The adjustment screws for these optics were purposely placed in the part of the photometer remote from interference, although cover plates were not used to positively prevent misalignment. It is believed that this mishap occurred during the replacement of a faulty power inverter unit by the aircraft maintenance crew after this unit had failed during the early part of the second test flight.

The only time when this particular alignment could be checked was during an actual flight with the detector liquid helium bath under correct vacuum conditions. By the time the aircraft had reached the correct starting point on the actual eclipse flight, the remaining solar signal was sufficiently small and time sufficiently short that,

even if this misalignment had been suspected, it is unlikely that it could have been corrected in time. Of the remaining two channels, the signal from channel 3 was, inexplicably, extremely sensitive to aircraft vibration, and this overloaded the electronic channel. Channel 1 was thus the only detector to produce useful data, and as specified earlier, its filter passband was centred at 20 cm^{-1} or $500 \text{ }\mu\text{m}$. Reacquisition of the sun image after third contact proved much more difficult than expected because of the slow residual drift of the heliostat, and consequently no useful data were obtained over this portion of the eclipse.

The fourth contact leg of the flight was successful in providing a normalization level for the sun's total energy under the precise conditions for which the second contact data had been taken. The noise and slow drifts which were present on the data from channel 1 prevented any attempt at detailed analysis of the data up to and including this contact.

5.3 Data Reduction and Initial Analysis

The primary data from the flight, in a 4000 bit per second bit stream encoded into 32 words of 8 bits each, were replayed from the flight tape recorder and decoded by a Conic D-Pad Data Processor to produce eight bit parallel data which were re-recorded onto digital computer-compatible tape using a Pertec tape recorder and formatter. Data from the one functional channel and from the time code generator were subsequently separated from this complete record in the CDC computer and stored independently upon magnetic tape. The data were then averaged in one, two, five, and ten second intervals from the basic data rate of

31 points per second, and examined. The near-totality data, for which the noise level became very significant, showed evidence of becoming biased by the digitization system being unable to handle negative signals. These sections of the data were read at 0.2 second intervals from the record of the in-flight chart recorder which had been adjusted before flight to accommodate negative signals. Subsequent comparison of this data with that from the computer established a good transformation and the final record contains the combined data. Gain changes were made throughout the eclipse period to maintain the correct signal level to the data encoder, and the value was written on the chart at the approximate time that the gain change was made. Unfortunately, the noise on the record, particularly near totality, meant that these times were by no means obvious on the record, and this fact was not noticed during the actual flight. These times of gain change were reliably established by a careful consideration of several factors, including a DC shift in the averaged record, and identification of a characteristic loss of signal continuity which was apparent whenever the gain was changed in the phase-sensitive detection system, during which it settled to the new signal level. Uncertainty in the times of gain change in the final record is now considered to be of the order of five seconds on all changes.

Comparison of this data with predictions of solar atmosphere models described in 2.2 required the normalization of the observed eclipse curve to the total solar signal. The data around totality established the contribution from the moon and from any remnant thermal gradient in the aircraft window or the atmosphere, and this value was

subtracted from the overall signal. The data obtained beyond fourth contact were used to establish a full sun plus moon level for carrying out this normalization under actual eclipse day flight conditions. Unfortunately, this latter value did not include an equivalent total moon contribution because of the restricted field of view of the photometers. Since the temperature of the dark side of the moon is only 104 K (Allen, 1973; Pugh, 1976) compared to the equivalent solar temperature of 5260 K, the correction to the normalization is small, and has been made assuming that about half of the moon was included in the field of view. Uncertainty in this correction, which itself amounted to only 1% of the normalization value, is very small compared with the inherent noise in the data at all points on the record, and is considered to be negligible.

5.4 Visible Monitor Eclipse Curve

The portion of the eclipse curve up to second contact obtained from one of the two visible monitors through a broadband red filter of wavelength approximately 600 nm, is shown in Fig. 5.1. The ordinate gives the measured signal, in bits from the PCM encoder. Unfortunately, this signal was not monitored during the flight because it appeared extremely sensitive to small heliostat and aircraft motions during the test flights and was therefore thought not to be useful, and thus the gain was not adjusted to obtain better digitization precision as totality approached. The situation for the other, more narrow-band, monitor was worse, with signal level starting at 11 bits and decreasing to zero rapidly, before totality was reached. Nevertheless, the noise on the monitor signal is very small, and the averaging of the signal in two

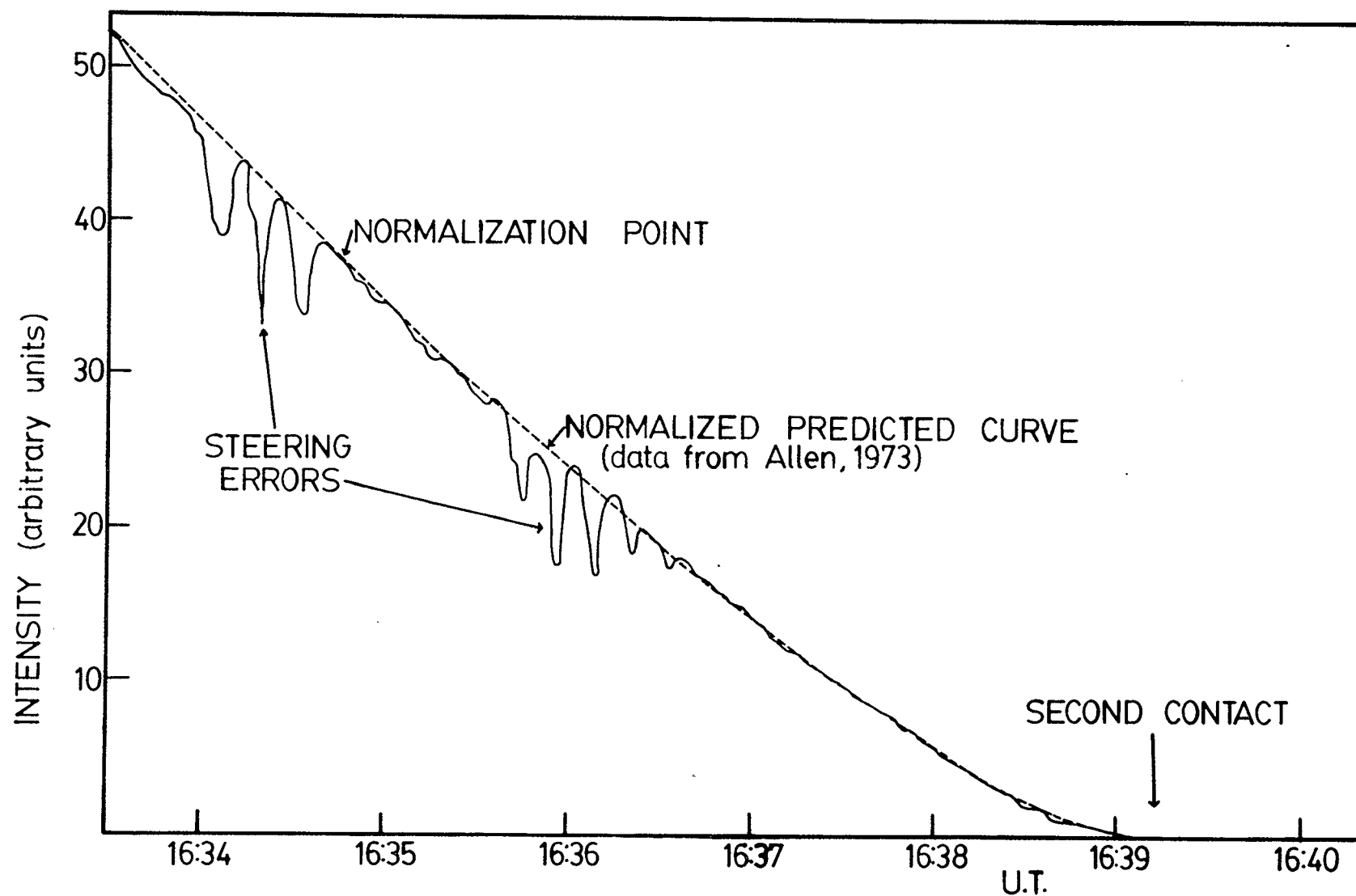


Fig.5.1 Eclipse curve for auxiliary optical sensor.

second intervals serves only to make the bit noise less apparent. Normalization to total sun intensity was not possible because, as mentioned previously, the gain was not changed and therefore the signal was overloaded.

The dashed curve gives the eclipse curve expected from a sun which has limb darkening of a form described by the parameters given by Allen(1973) for 600 nm, normalized at a point to the measured eclipse curve. The major deviations of the measured curve from that predicted are caused by errors in steering of the heliostat mirror. Smaller excursions could be explained either by steering errors or by small changes in the aircraft heading, since the small size of the visible window meant low tolerance to changes in direction before vignetting of the beam occurred. Apart from such deviations, the measured curve can be seen to follow the predicted one very closely down to second contact. The resolution is estimated to be $0.5''$, and is limited only by digitization errors. To this resolution, there is no indication of the existence of any anomalous feature in the eclipse curve, and thus the intensity distribution across the sun at approximately 600 nm at the time of eclipse can be described accurately by the normal limb darkening equation.

5.5 Far Infrared Data

Figures 5.2, 5.3, and 5.4 show the data obtained from channel 1 from 16:33:30 UT until after second contact, averaged in one, five, and ten second intervals respectively, and corrected for gain changes. The remnant contribution to intensity from the moon has been subtracted, and the normalization has been performed as described in 5.3.

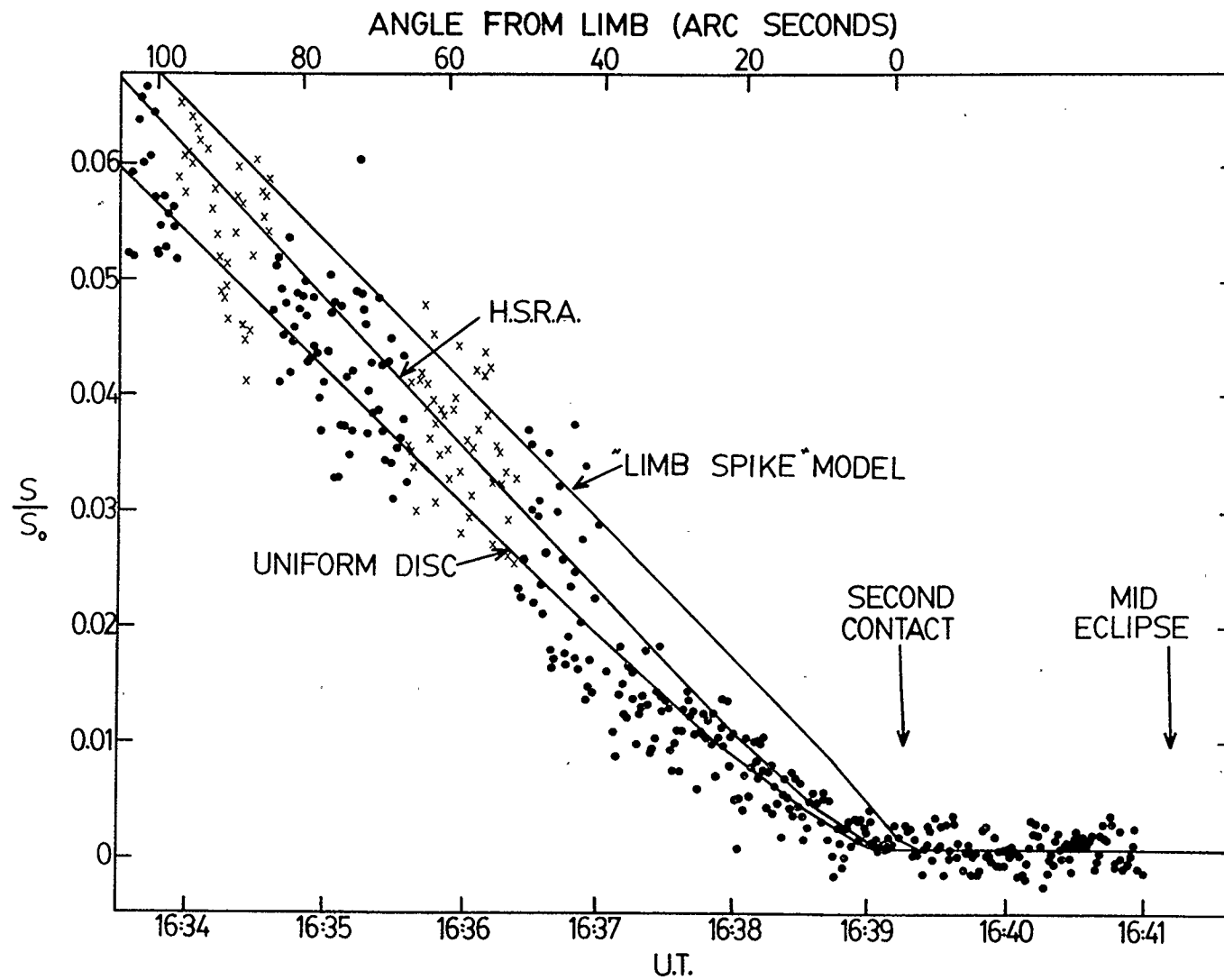


Fig. 5.2 One second data averages and model predictions.

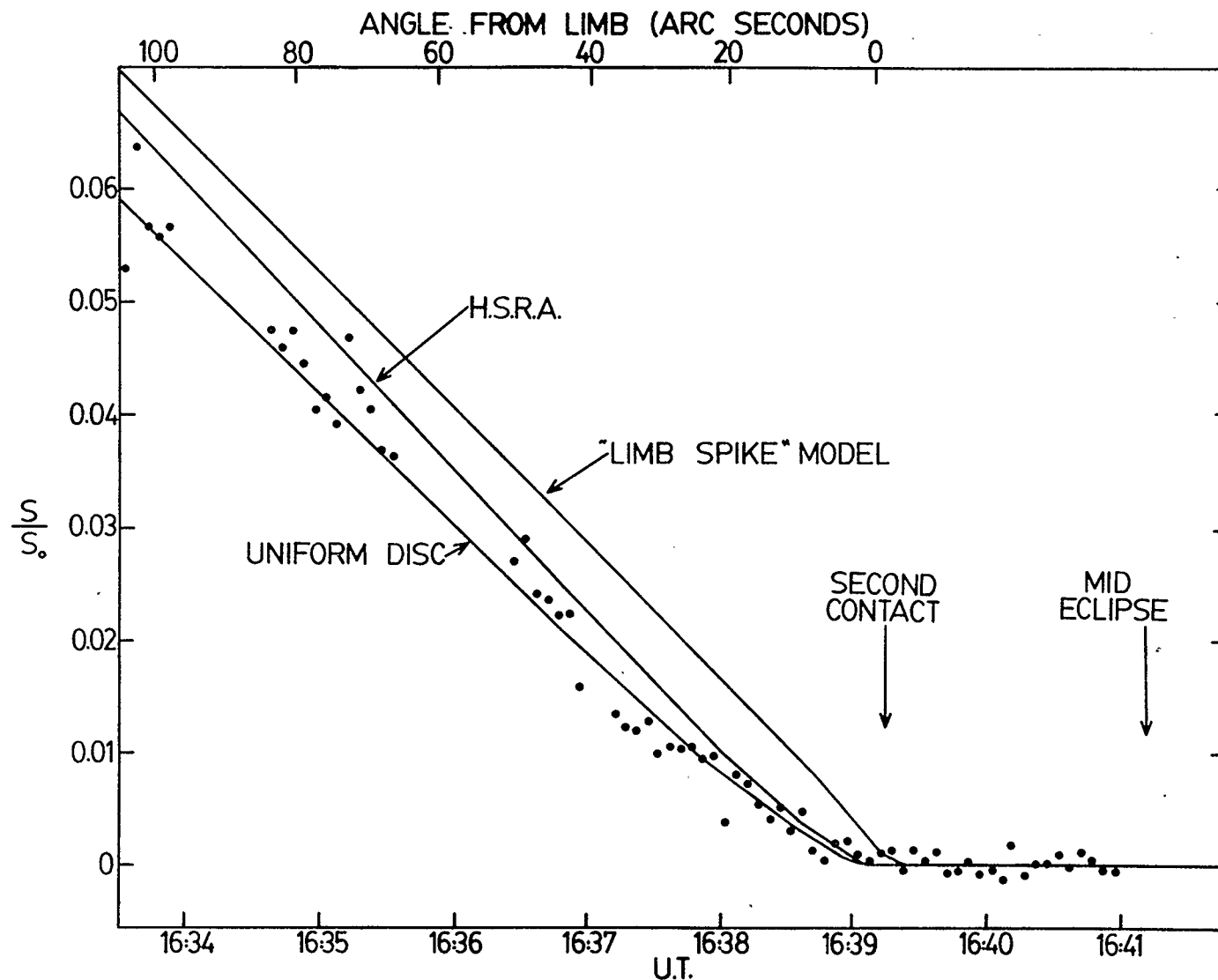


Fig. 5.3 Five second data averages and model predictions.

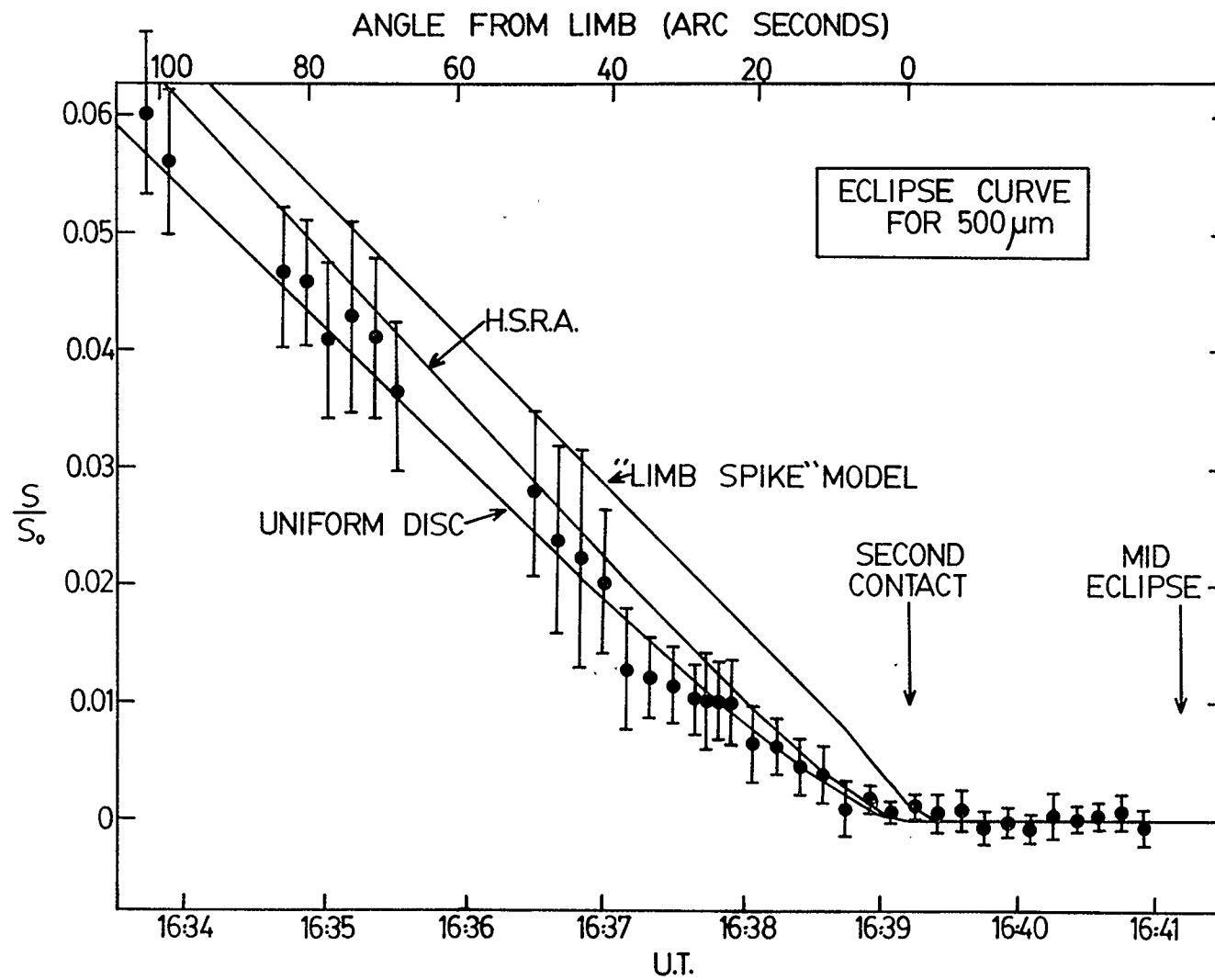


Fig. 5.4 Ten second data averages and model predictions.

Surprisingly, the net signal remaining after second contact (and subtracted from the data shown) is very small, of the order of 0.06% of that from the full sun, whereas the temperature of the dark side of the moon is 2% of the solar temperature, and hence, according to the Rayleigh-Jeans approximation to the blackbody curve which is valid in this wavelength region, the ratio of intensities should also be 2%. This apparent lack of signal from the moon can be explained by a thermal gradient in the aircraft window, which would lead to a net signal in chopping between the two beams sufficient to offset that from the moon, although the required thermal gradient admittedly would be large, of the order of 10 K. The sensitivity of the equipment was certainly sufficient to detect a signal equivalent to that from the moon, and its absence remains a puzzle.

The data plotted as crosses in Fig. 5.2 represent that obtained during times of poor steering, as indicated by the visible monitor signal (Fig. 5.1). The minor excursions also present in the monitor data are not expected to have counterparts in the infrared signal, since the latter has significantly greater tolerance to aircraft orientation relative to the sun before vignetting occurs because of the larger window size. The data during times of poor steering do not show large excursions relative to surrounding data values, as expected because the experiment had been designed to allow sufficient latitude for such errors, but they do have a slightly higher mean level than expected from extrapolation between neighbouring sections. The increase in signal is an unexpected feature, but is thought to be related to the phase-sensitive detection process rather than indicating poor optical alignment.

Alternate blades of the chopper were designed to be coplanar, but slight warping occurred several weeks after construction. This led to a four-fold chop of the form sun(centred) - sky - sun(very slightly off centre) - sky(very slightly different physical region), rather than the desired alternation of sun and sky. During the test flights, the optical alignment was adjusted to give a symmetric chop rather than having the difference of signal from one pair of blades larger than that from the other pair. Steering errors shifted the response of the system from the symmetric to the asymmetric mode, with the result that the phase-sensitive detection system interpreted this as an increase in signal. Unfortunately, the desired tolerance to steering errors is reduced by this effect, and therefore sections of data coinciding with such errors as shown by the visible monitor signal were removed from the other infrared eclipse curves shown (Figs. 5.3 and 5.4).

The amount of noise present in the data is greater than expected, and necessitated averaging over several seconds. The standard deviations calculated from these averages are shown for the ten second averaged eclipse curve, Fig. 5.4, in which each point plotted represents the average of 312 individual values. The four points near 16:37:45 UT at five second intervals show the transition from computer-read data to that read manually from the in-flight chart recording. There is very good agreement between the computer generated and hand read data in the regions where the two sets overlap. The noise present has a component which is dependent on signal level, and whose origin is unknown, although it might be due to vignetting somewhere along the beam, which would decrease as the size of the crescent of the sun decreased.

The portion of the eclipse curve close to second contact should, however, be completely free of vignetting effects, and therefore the source of the signal-dependent noise remains unexplained.

The curves generated for three intensity distributions across the sun; a uniform distribution, that expected from the HSRA model, and that arising from Beckman's observation of a limb spike, are shown for comparison with the data. It can be seen that the data follow the predicted curve for a uniform disc better than that for the HSRA model, while the curve for the limb spike model lies sufficiently far outside the error bars for the data points that it cannot be considered as a reasonable representation of the data. A statistical verification of the relative merit of the three generated curves in representing the data was performed in the form of a chi-squared test. The values of the reduced χ^2 parameter, defined by

$$\chi_v^2 = \frac{1}{v} \sum_i \frac{(M_i - P_i)^2}{\sigma_i^2} ,$$

where M is the measured data point, P is the predicted value, σ^2 is the standard deviation of the point, and v is the number of independent data values; obtained from the test are 0.49, 1.17, 6.21, and 0.89 for the uniform distribution, HSRA model, limb spike model, and an intensity distribution having limb brightening of one-third the amount predicted by the HSRA model, respectively. For a reasonable agreement between measured data and a generated curve, the value of the χ_v^2 parameter should be close to or less than one, since it would be expected that $(M_i - P_i)^2$ should, on average, be of the order of σ_i^2 . Large values of

χ_v^2 indicate a poor fit, as in the case of the limb spike model. The values of the probability of exceeding the above values of χ_v^2 for a curve that is a true representation of the data are >0.99, 0.18, <0.001, and 0.71 for the above models and the number of degrees of freedom present in the five second averaged data (Bevington, Appendix C, 1969). A value of the χ_v^2 parameter significantly less than one, as in the case of the uniform disc distribution, may be the result of accidental alignment of data and prediction or may mean that the values of σ^2 used are larger than the actual errors inherent in the data. In this case, the uniform disc and a model with slight limb brightening both are good fits to the data, while the HSRA distribution is improbable as a representation of the data.

Visual examination of the data suggests that the χ_v^2 parameter is slightly misleading, since it gives a measure of the agreement over the entire curve, while in fact the data could follow different curves over various sections of the eclipse. This appears to be true, with the early data being consistently higher than the uniform disc predicted curve, and lower during approximately 16:37 to 16:38 UT. Interpretation of such a shape of eclipse curve is not straightforward, since it is an integral relationship with intensity distribution, but in broad outline it would represent a sun whose intensity decreases approximately 25^m within the limb, then increases sharply for a few arcseconds near 40^m inside the limb, and then settles back to a mean level. Such an intensity distribution, if real, would provide evidence for complex structure in the solar atmosphere at low chromospheric heights. Unfortunately, the sharp change in signal level near 16:37 UT coincides with a gain change,

and an alternative explanation for the shift is possible. The change of gain increases the level of the signal going into the phase-sensitive detection system to near the maximum acceptable level, and noise on top of the signal may be clipped. Therefore, an averaged signal coming out from the system will be biased toward lower values near the top end of the gain range, while the reverse situation can be expected to hold near the lower limit, resulting in an apparent lack of continuity across a gain change in the presence of large amounts of noise. Evidence for such biasing was provided by an overload indicator at the phase-sensitive detector card, which was on intermittently during the eclipse flight. Therefore, the interpretation of this one particular feature of the data in terms of complex intensity structure is difficult to justify.

Minor changes in the eclipse curve could be expected to result from active regions on the sun. A calcium plage region can have a temperature approximately 200 K or 4% above that of its surroundings (Beckman and Clark, 1971), and if such a region occupied 10% of any given arc length, then the increase in radiation seen from that arc would be 0.4%. This small increase in intensity would lie on top of the integrated intensity from the portion of the sun unobscured by the moon, and would consequently be most easily detectable at the limb. With the present data, such a small increase in intensity would not be observable. If such active regions were uniformly distributed over the solar surface (as was approximately true; see Fig. 4.4), they could not be detected at all with the present technique, because it is essentially differential in nature. Therefore the presence of active regions

can be expected not to have any significant effect on the measured eclipse curve.

Bearing in mind the possible bias of the data near 16:37 UT, it can be seen that the intensity distribution which best represents the data is essentially uniform, with the possibility of very slight limb brightening of magnitude certainly less than half that predicted by the HSRA model, over $100''$ from the limb. The lack of limb brightening seen by other workers has earlier been interpreted as indicating a flat temperature minimum region, broader than that assumed in the models. However, the approximate shape of the minimum is now sufficiently well determined by other observations, such as absolute measurements at disc centre at various wavelengths, that such a conclusion cannot be made without an inconsistency remaining between centre to limb variations and disc centre measurements. The alternative explanation proposed has been the effect of inhomogeneities in the suppression of limb brightening, whose scale height increases with height above the photosphere (a necessary feature to retain the observed degree of limb darkening at visible wavelengths). If these inhomogeneities were to be related to spicules at higher chromospheric levels, evidence for this should appear in the form of a bright spike extending outside the solar limb, as seen by Beckman et al. There is no evidence in the present data for the existence of such a spike. Of special importance to the detectability of such a spike is its extension beyond the limb, since it contains a significant amount of energy due to large arc length, and to a high level of confidence, any extension of total energy greater than 0.5% of that of the full sun can be ruled out in the present case.

It is not clear why two measurements obtained in almost equivalent ways should yield contradictory results, and therefore a repetition of the experiment would be very useful for the resolution of the discrepancy.

In order to evaluate the amount of radiation expected from spicule matter, it is necessary to know the height distribution of number density, electron density and temperature within the spicule, and width and height of spicules. These data are not available from optical observations for heights below 3000 km (Bray and Loughhead, Ch. 2, 1974). The sole determination of these properties has been that of Beckman and Ross (1976) from the eclipse measurement of the last 19th of the solar limb, discussed previously. Therefore the detectability of spicules in an eclipse measurement remains uncertain, with the present results in fundamental disagreement with those obtained during a previous eclipse.

Inhomogeneities existing in the chromosphere are expected to have observable effects apart from possible contribution at the limb from spicules, and the most noticeable of these effects is the suppression of limb brightening predicted by homogeneous models. Lindsey and Hudson (1976) have calculated centre to limb curves expected from various shapes of irregularities assuming that an intrinsic angular dependence of radiation intensity exists in the inhomogeneity. Their curves derived for an angular dependence of the form $\ln[\sec(\psi)]$, where ψ is angle from normal to the surface, show a suppression of brightening over most of the disc, with a minimum followed by a bright spike at the limb. The requirement for an intrinsic angular dependence could be considered

a weakness of the method, but it is not necessary, as has been demonstrated by different approaches taken by other authors. A combination of disc centre measurements at millimetre wavelengths and eclipse measurements in the Balmer continuum were used by Beckman, Clark, and Ross(1973) to demonstrate that the chromosphere cannot be in hydrostatic equilibrium, and thus any interpretation of observations of this region must include effects of inhomogeneities. Spicular models have been shown not to be useful for the explanation of lack of significant limb brightening at millimetre wavelengths, since such models inevitably predict a high degree of limb brightening, much more than that from homogeneous models. However, Beckman et al(1973) have shown that this absence can be explained by a vertically disturbed model, in which surfaces of constant electron temperature and number density are randomly displaced, representing rising and falling gas, by tracing rays through such a model chromosphere. The authors suggest the possibility of determining the scale of chromospheric roughness from measurements of the amount of residual brightening remaining at various wavelengths. The absence in this perturbed model of effects due to spicules can be explained either by their merging into the remainder of the chromosphere at heights below 2000 km, or by the presence of optically thicker, cooler material shielding the spicules from observation. Whether spicules are observable directly at submillimetre wavelengths has not been determined conclusively, but the foregoing discussion indicates that they should not be expected to appear solely at the limb, but rather to produce apparent brightening extending over a large part of the solar disc and increasing toward the limb. The present data

suggest that spicules are not observable either at the limb or as a contribution to limb brightening, to within the accuracy of the present measurement. The effects of inhomogeneities can clearly be seen in the suppression of the expected limb brightening, and a scale size for these cannot be significantly below 1000 km. Measurements at other wavelengths would be useful to determine the scale size more accurately.

5.6 Uncertainties in the Data

Despite efforts to reconcile all the observational material obtained, some inconsistencies and uncertainties remain in the data. The possible overloading of the phase-sensitive detection system described earlier could lead to a bias in the data which is both time dependent and gain dependent, and cannot be evaluated quantitatively. However, apart from a period of 30 seconds around 16:37, this effect is estimated to be small. The exact times of gain changes are not known to within five seconds, but this would only affect a few points in the entire eclipse curve. A systematic error could arise from inaccuracy in the adopted value of the apparent angular speed of the eclipse relative to the aircraft or in variations in this speed. The several methods considered for the determination of the former gave reasonable agreement, but better knowledge of the navigational track would have markedly improved the reliability of this vital measurement. The small Lear Jet was unfortunately not equipped with continuously monitoring position information such as would be available with OMEGA navigational aids.

The lack of the expected lunar signal after second contact is puzzling, and if a thermal gradient in the window is the true explanation, then the time dependence of this gradient is important for the

interpretation of the eclipse curve. No evidence is seen for any time change of the final radiation level reached after second contact and hence this level is considered to be that of the lunar contribution. A slight out-of-phase adjustment could also easily lead to such an offset. The correction to the normalization to allow for total moon contribution is small, as was previously mentioned, and is not expected to lead to significant error. The direction of change of signal with steering errors is a source of concern in that it may indicate significantly less tolerance to such errors than desired, possibly because of poor focussing of optics, and this may have led to vignetting of the beam. The large amount of noise, especially the component which is signal dependent, is of unknown origin. Especially puzzling is the data before 16:33:30 UT, which did not show a reasonable trend downward, as would be expected during the eclipse, at all. A similar problem occurred in the data after third contact, in which there was little noise on the data until a certain signal level was reached, after which time even the upward trend of the data was not obvious. An inconsistency in signal level between the pre-second contact data and the equivalent point in the eclipse after third contact was seen, which cannot be explained except perhaps by the presence of a time-varying offset, a thermal signal from a source other than the sun, or the vignetting problem alluded to earlier.

Despite these problems, however, it is encouraging that the measured curve showed the characteristics of an eclipse, and reached a flat level after second contact, as expected. Continuity between points, even over gain changes, was good, and the normalization yielded a curve

which agrees well over the whole second contact run with independently normalized, theoretically generated curves. For these reasons it is believed that the second contact data are self-consistent, and provide valuable information on the structure of the solar atmosphere.

5.7 Improvements and Future Work

An ideal measurement of an eclipse curve unfortunately has many conflicting requirements. Good spectral resolution would be useful, while high signal to noise ratio is essential; and it would be desirable to monitor the entire eclipse, from first to fourth contact, while having as slow an apparent angular speed of eclipse as possible. Ideally, the measurement would be made from above the earth's atmosphere to eliminate any effects from variations in emission or transmission, and without the presence of a thick absorbing window in the beam. The most acceptable practical compromise appears still to be an aircraft-borne experiment, modified according to the experience gained during the course of the present experiment.

Design of an experiment to repeat the present measurement is in progress, for a possible flight into the 1980 eclipse over Africa. The design of the photometer remains basically the same, but the diameter of the primary optics will be increased to 15 cm, with a consequent increase in detector size to 5 mm, to obtain increased signal, and it is hoped to replace the Mylar beamsplitter by a dichroic one, to obtain two wavelength channels (if possible, bracketing those used in the present measurement) with minimum loss of intensity. Field of view will be increased to three solar diameters, and the field lens will be eliminated, to provide greater tolerance to steering errors and location of

focus. It is hoped that window size will be increased, and angle of incidence changes will be compensated for by a height adjustment similar to that used in the present experiment, as well as an additional azimuth motion adjustment. It is hoped that the steering will have improved sufficiently to allow monitoring throughout the period of totality to obtain a signal level from the moon. Time resolution will be maintained at the present value of one second or better, to achieve spatial resolution in one dimension of less than $0.5''$. If the entire eclipse curve, or half of it, can be monitored to give total sun intensity, improved navigational knowledge will be essential for subsequent timing of the eclipse. A position indicating system such as OMEGA would be useful to provide this information. In this way, it should be possible to obtain an improved measurement of the centre to limb intensity distribution across the sun to high spatial resolution, and in particular to search for the effects of spicules or other inhomogeneities on the eclipse curve.

REFERENCES

- Ade, P.A.R., J.E. Beckman, and C.D. Clark, (1971), *Nature*, 231, 55.
- Ade, P.A.R., J.D.G. Rather, and P.E. Clegg, (1974), *Ap. J.*, 187, 389.
- Allen, C.W., (1973), "Astrophysical Quantities", 3rd ed., Athlone Press.
- "American Ephemeris and Nautical Almanac, 1979", (1977), U.S. Government Printing Office.
- Ando, H., and Y. Osaki, (1977), *Publ. Astr. Soc. Japan*, 29, 221.
- Athay, R.G., (1970), *Ap. J.*, 161, 713.
- Athay, R.G., and O.R. White, (1978), *Ap. J.*, 226, 1135.
- Bastin, J.A., A.E. Gear, G.O. Jones, H.J.T. Smith, and P.J. Wright, (1964), *Proc. Roy. Soc. A*, 278, 543.
- Beckers, J.M., (1968), *Solar Phys.*, 3, 367.
- Beckman, J.E., and C.D. Clark, (1971), *Solar Phys.*, 16, 87.
- Beckman, J.E., and C.D. Clark, (1973), *Solar Phys.*, 29, 25.
- Beckman, J.E., C.D. Clark, and J. Ross, (1973), *Solar Phys.*, 31, 319.
- Beckman, J.E., J.C.G. Lesurf, and J. Ross, (1975), *Nature*, 254, 38.
- Beckman, J.E., and J. Ross, (1976), in "Far-Infrared Astronomy", M. Rowan-Robinson, ed., Pergamon.
- Bevington, P.R., (1969), "Data Reduction and Error Analysis for the Physical Sciences", McGraw-Hill.
- Bonnet, R.M., and J.E. Blamont, (1968), *Solar Phys.*, 3, 64.
- Bray, R.J., and R.E. Loughhead, (1974), "The Solar Chromosphere", Wiley.
- Bruner, E.C. Jr., (1978), *Ap. J.*, 226, 1140.
- Clegg, P.E., R.A. Newstead, and J.A. Bastin, (1969), *Phil. Trans. Roy. Soc. London A*, 264, 293.
- Coates, R.J., J.E. Gibson, and J.P. Hagen, (1958), *Ap. J.*, 128, 406.
- Durrant, C.J., (1978), *Q. J. R. Astr. Soc.*, 19, 411.
- Elste, G., (1968), *Solar Phys.*, 3, 106.

"Explanatory Supplement to the Astronomical Ephemeris and the American Ephemeris and Nautical Almanac", (1961), Her Majesty's Stationery Office.

Frisch, H., (1972), Space Sci. Rev., 13, 455.

Gingerich, O., (1963), Ap. J., 138, 576.

Gingerich, O., and C. de Jager, (1968), Solar Phys., 3, 4.

Gingerich, O., R.W. Noyes, W. Kalkofen, and Y. Cuny, (1971), Solar Phys., 18, 347.

Gingerich, O., and J.C. Rich, (1968), Solar Phys., 3, 82.

Hagen, J.P., and P.N. Swanson, (1975), Ap. J., 198, 219.

Hagen, J.P., P.N. Swanson, R.W. Haas, F.L. Wefer, and R.W. Vogt, (1971), Solar Phys., 21, 286.

Heintze, J.R.W., H. Hubenet, and C. de Jager, (1964), Bull. Astr. Inst. Netherlands, 17, 442.

Hill, H.A., and T.P. Caudell, (1979), Mon. Not. Roy. Astr. Soc., 186, 327.

Holweger, H., (1967), Z. Astrophys., 65, 365.

John, T.L., (1964), Mon. Not. Roy. Astr. Soc., 128, 93.

John, T.L., (1966), Mon. Not. Roy. Astr. Soc., 131, 315.

Johnson, N.J., (1971), "Solar Infrared Limb Profiles", Ph.D. thesis, University of Michigan.

Kundu, M.R., (1971), Solar Phys., 21, 130.

Kundu, M.R., and S.-Y. Liu, (1975), Solar Phys., 44, 361.

Kurokawa, H., K. Nakayama, T. Tsubaki, and M. Kanno, (1974), Solar Phys., 36, 69.

Kurucz, R.L., (1974), Solar Phys., 34, 17.

Labrum, N.R., J.W. Archer, and C.J. Smith, (1978), Solar Phys., 59, 331.

Lantos, P., and M.R. Kundu, (1972), Astron. Astrophys., 21, 119.

Léna, P.J., (1968), Solar Phys., 3, 28.

Léna, P.J., (1970), Astron. Astrophys., 4, 202.

Lindsey, C., and H.S. Hudson, (1976), Ap. J., 203, 753.

- Mankin, W.C., and J. Strong, (1969), "Solar Limb Darkening in the Far Infrared and its Relation to the Temperature of the Chromosphere", Report NGR 22-010-025.
- Moe, O.K., and E.F. Milone, (1978), Ap. J., 226, 301.
- Nakayama, K., (1976), Publ. Astr. Soc. Japan, 28, 141.
- Neidig, D.F. Jr., (1973), Solar Phys., 33, 63.
- Newstead, R.A., (1969), Solar Phys., 6, 56.
- Noyes, R.W., J.M. Beckers, and F.J. Low, (1968), Solar Phys., 3, 36.
- Pierce, A.K., R.R. McMath, L. Goldberg, and O.C. Mohler, (1950), Ap. J., 112, 289.
- Pierce, A.K., and C.D. Slaughter, (1977), Solar Phys., 51, 25.
- Pierce, A.K., C.D. Slaughter, and D. Weinberger, (1977), Solar Phys., 52, 179.
- Pugh, M.J., (1976), in "Far-Infrared Astronomy", M. Rowan-Robinson, ed., Pergamon.
- Righini, G., and M. Simon, (1976), Ap. J., 203, L95.
- Righini-Cohen, G., and Simon, M., (1977), Ap. J., 217, 999.
- Samain, D., (1979), Astron. Astrophys., 74, 225.
- Samain, D., R.M. Bonnet, R. Gayet, and C. Lizambert, (1975), Astron. Astrophys., 39, 71.
- Shimabukuro, F.I., (1971), Solar Phys., 18, 247.
- Shimabukuro, F.I., and J.M. Stacey, (1968), Ap. J., 152, 777.
- Shimabukuro, F.I., W.J. Wilson, T.T. Mori, and P.L. Smith, (1975), Solar Phys., 40, 359.
- Simon, M., (1971), Solar Phys., 21, 297.
- Simon, M., D. Buhl, J.R. Cogdell, F.I. Shimabukuro, and C. Zapata, (1970), Nature, 226, 1154.
- Simon, M., and H. Zirin, (1969), Solar Phys., 9, 317.
- Smart, W.M., (1971), "Text-Book on Spherical Astronomy", 5th ed., Cambridge University Press.
- Smith, P.L., (1975), I.E.E.E. Trans. Antennas and Propagation, AP-23, 237.

Stein, R.F., and J. Leibacher, (1974), Ann. Rev. Astron. Astrophys.,
12, 407.

Swanson, P.N., and J.P. Hagen, (1975), Solar Phys., 43, 57.

Tousey, R., (1963), Space Sci. Rev., 2, 3.

Ulmschneider, P., and W. Kalkofen, (1978), Astron. Astrophys., 69, 407.

Unsöld, A., (1977), "The New Cosmos", 2nd ed., Springer-Verlag.

Vernazza, J.E., E.H. Avrett, and R. Loeser, (1973), Ap. J., 184, 605.

Vernazza, J.E., E.H. Avrett, and R. Loeser, (1976), Ap. J. Suppl., 30, 1.

White, O.R., R.C. Altrock, J.W. Brault, and C.D. Slaughter, (1972),
Solar Phys., 23, 18.

Zirin, H., (1966), "The Solar Atmosphere", Blaisdell.